9

Biological systems: Applications and perspectives

Henk Fidder[1], Karsten Heyne[1], Selma Schenkl[5], Frank van Mourik[2], Gert van der Zwan[5], Stefan Haacke[2], Majed Chergui[2], Mikas Vengris[3], Delmar S. Larsen[4], Emmanouil Papagiannakis[5], John T.M. Kennis[5], Rienk van Grondelle[5], Ben Brüggemann[6], Volkhard May[7], Inés Corral[8], Leticia González[8], Alexandra Lauer[1], Eike Meerbach[9], Christof Schütte[9], Illia Horenko[9], Burkhard Schmidt[9], and Jean-Pierre Wolf[10,11]

[1] Institut für Experimentalphysik, Freie Universität Berlin, Germany
[2] École Polytechnique Fédérale de Lausanne, Switzerland
[3] Vilnius University Faculty of Physics Laser Research Center, Lithuania
[4] Department of Chemistry University of California, USA
[5] Faculty of Sciences Vrije Universiteit Amsterdam, The Netherlands
[6] Chemical Physics, Lund University, Sweden
[7] Institut für Physik, Humboldt-Universität zu Berlin, Germany
[8] Institut für Chemie und Biochemie, Freie Universität Berlin, Germany
[9] Institute of Mathematics II, Freie Universität Berlin, Germany
[10] GAP-Biophotonics, University of Geneva, Switzerland
[11] LASIM (UMR 5579), Université Claude Bernard Lyon 1, France

Coordinated by: Karsten Heyne

9.1 Investigation of diverse biological systems

H. Fidder and K. Heyne

Viable biological systems occur on a wide scale of dimensions ranging from sizes of 30 meters for mammals (blue whale), and 120 meters for plants (sequoia tree), down to 10^{-6} meters for single cellular organisms. These systems consist either of networks of eucaryotic cells, in which specialized cells take over unique functions, or of single procaryotic as well as eucaryotic cells. Procaryotic cells exhibit a simple build without a cell nucleus, whereas the build of eucaryotic cells is of a higher complexity, including a cell nucleus with a double membrane. Every cell consists of a cell membrane which encloses the cytoplasm, the DNA (desoxyribonucleic acid) and RNA (ribonucleic acid) which acts as the carrier of the genetic information, and proteins and enzymes

which catalyze cellular reactions and build up substructures inside the cell. Ribosomes represent the protein production machine and are found in both procaryotes and eucaryotes. Ribosomes are responsible for processing the genetic instructions and for converting the genetic code into the exact sequence of amino acids that make up a protein. Structures of higher complexity are, for example, the endoplasmic reticulum and the Golgi apparatus. The endoplasmic reticulum is the transport network for molecules targeted for certain modifications and specific destinations. The Golgi apparatus is the central delivery system for the cell, and is a site for protein processing, packaging, and transport.

The cellular membrane is a lipid bilayer impermeable to ions and polar molecules, which acts as a barrier to define a biochemical environment inside the cytoplasm that differs from outside. Permeability is conferred by two classes of membrane proteins, channels and pumps. Channels enable ions to flow rapidly through membranes in a thermodynamically downhill direction. Pumps, by contrast, use a source of free energy such as ATP (adenosine triphosphate) or light to drive the uphill transport of ions or molecules. One example for such a pump is bacteriorhodopsin (bR), which pumps protons across the cellular membrane against a proton gradient upon light absorption. The proton gradient can be harnessed to generate ATP from ADP (Adenosine diphosphate) by another membrane protein called ATP synthase. This process allows the bacterium *Halobacterium salinarium*, which is sketched in Fig. 9.1, to survive under unfavorable conditions. In addition to proteins, peptidoglycan polymers consisting of sugars and amino acids, can form a homogeneous layer outside the plasma membrane giving the wall shape and structural strength, as well as counteracting the osmotic pressure of the cytoplasm. The peptidoglycan layer is substantially thicker in Gram-positive bacteria (20 to 80 nm) than in Gram-negative bacteria (7 to 8 nm). Gram-positive bacteria are classified as bacteria that retain a crystal violet dye during the gram stain process. Gram-positive bacteria will appear blue or violet under a microscope, whereas gram-negative bacteria will appear red or pink. The difference in classification is largely based on a difference in the bacteria's cell wall structure and therefore in its composition (see Sect. 9.7). This is highly relevant in medical treatments, because antibacterial drugs, such as penicillin, interfere with the formation of the peptidoglycan layer, and therefore with cell reproduction.

The key events of biological processes originate from protein functions and their interactions with cofactors and substrates. There is a variety of important cofactors such as: i) ATP (adenosine triphosphate), the universal "currency" of free energy in biological systems; ii) NADH (nicotinamide adenine dinucleotide) and $FADH_2$ (flavin adenine dinucleotide), the major electron carriers in the oxydation of "fuel" molecules, such as glucose and fatty acids; and iii) NADPH (nicotinamide adenine dinucleotide phosphate), the major electron donor in reductive biosynthesis. Proteins play crucial roles in virtually all biological processes. In enzymatic catalysis proteins usually increase reaction rates by at least a millionfold. They transport and store small

molecules and ions, e.g., oxygen in haemoglobin. Proteins are responsible for coordinated motion, such as muscle contraction, by the sliding motion of two kinds of protein filaments, or the swimming of bacteria by rotation of flagellae (e.g., Fig.9.1). Immune protection is accomplished by antibodies, which

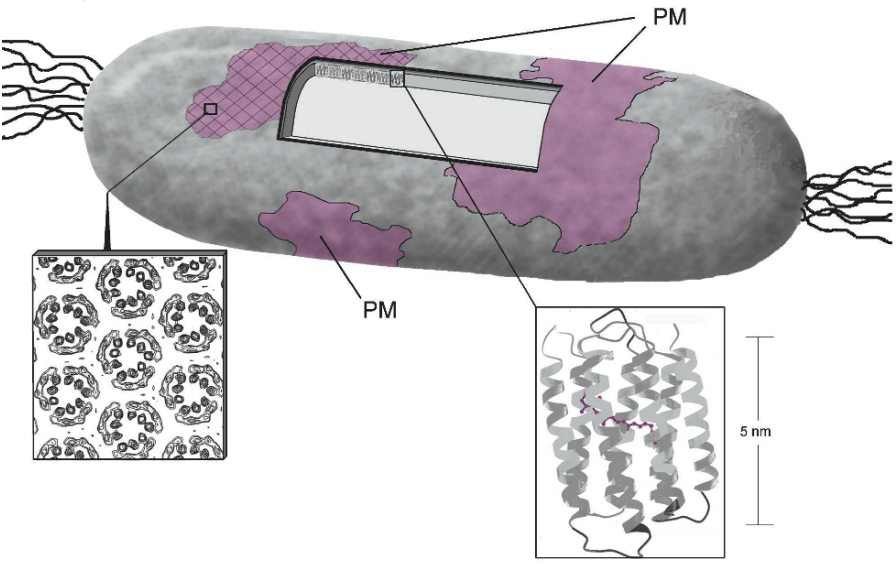

Fig. 9.1. Model of the *Halobacterium salinarium*. The bacterium spanning a length of some micrometers is sketched with its flagella on both sides; regions of the purple membrane (PM) containing the transmembrane protein bacteriorhodopsin (bR); lower panel; left side: top view of the bacteriorhodopsin proteins in the PM measured by X-ray diffraction [1,2]; right side: side view of bacteriorhodopsin with the retinal chromophore (purple) measured by electron-diffraction [3].

are highly specific proteins that recognize and combine with viruses, bacteria, and cells from other organisms. Moreover, mechanical support, such as the strength of the skin and bone, is due to the presence of the fibrous protein collagen. Generation and transmission of nerve impulses is mediated by receptor proteins. For example, rhodopsin, a protein related to bacteriorhodopsin, is the light-sensitive protein in retinal rod cells in the eye, which undergoes a cis to trans isomerization of its chromophore retinal, and triggers a reaction cascade leading to a nerve impulse from the eye. Growth and differentiation of cells is controlled by proteins, while the coordination of different activities of cells is regulated by hormones, which are often proteins themselves. Proteins serve in all cells as sensors that control the flow of energy and matter and thus they are the machinery of the cell.

All proteins are built from a repertoire of 20 amino acids. An amino acid consists of an amino group (NH_2), a carboxyl group ($COOH$), a hydrogen atom, and a R group, called residue or side chain. All groups are bonded to a carbon atom called α-carbon; and the tetrahedral array of the four different groups confers optical activity to amino acids, with two mirror-image forms called the L isomer and the D isomer. Almost only L isomers are constituents of natural proteins. The side chains R of the 20 amino acids differ in size, shape, charge, hydrogen-bonding capacity, and chemical reactivity. Two examples of amino acids are shown in Fig. 9.2. Glycine has the simplest side chain with just a hydrogen atom. Tryptophan, on the other hand, has a longer side chain belonging to the aromatic side chains, and consisting of an indole joined to a methylene group (see Fig. 9.2). In proteins, the α-carboxyl group of one amino acid is joined to the α-amino group of another amino acid

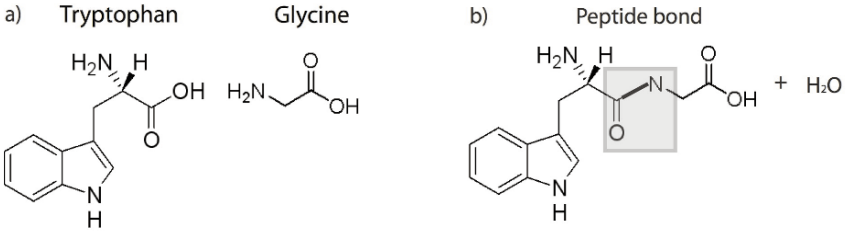

Fig. 9.2. Amino acids tryptophan and glycine; and the dipeptide with the planar peptide bond.

forming a peptide bond (see Fig. 9.2). The protein consists of a repetitive and a variable region. The main chain or protein backbone is a repetition of peptide bonds, whereas the side chains constitute the variable part. Most natural proteins contain anywhere from about ten to several thousands of amino acid residues and the sequence of each protein is unique. The sequence is called the primary structure, where small variations can lead to widely different three dimensional structures and biological functions. Three dimensional structural motifs are called secondary structures. They are determined by the interaction of peptide units $-C_\alpha - (C = O) - (N - H) - C_\alpha -$ of a peptide chain. The peptide units are rigid and planar, narrowing down the possibilities of peptide conformations. The planarity and the possibility of forming hydrogen bonds between the carboxy and amino groups of peptide units lead to regular protein structures, as α-helices and β-sheets. An example of an α-helical protein is the photoreceptor bacteriorhodopsin plotted in Fig. 9.1. It has seven α-helices reaching from inside the cell through the cellular membrane to the other side. Many photoreceptor proteins exhibit a chromophore covalently bound to a specific amino acid called the binding site. This specific location inside the protein predominantly has a well-defined

three-dimensional structure with optimized interactions between the chromophore and the protein surroundings. These surroundings can give rise to Coulomb interactions and interactions by hydrogen bonds, π-stacking, steric hindrance, etc. In bacteriorhodopsin these interactions result in an optimized trans to cis isomerization process of the retinal chromophore, with an increased quantum yield and an isomerization dynamics of 500 fs, which is at least 3 times faster than the isomerization reaction in solution [4–7]. A mechanism for reaction optimization in bacteriorhodopsin is presented in Sect. 9.2.

Since living plants and organisms are continuously undergoing many structural changes and meanwhile perform tremendously complex chemical reactions, spectroscopic techniques have to be selected to answer specific questions in such systems. The many chemical and physical events at the basis of the functioning of any living organism occur on a hierarchy of timescales ranging from femtoseconds to seconds. A real-time study of the mechanisms and dynamics of rudimentary chemical reaction steps and energy flow in plants, bacteria, and living beings requires a well-defined trigger to set off a particular chain of events. Therefore, ultrafast time-resolved investigations are mainly concerned with photoinitiated reactions and processes. Despite this limitation, this subcategory includes some of the most important and interesting biological processes, particularly in light of nature's ability to harvest the sun's energy as fuel being the basis for virtually all life on our planet. Despite the plurality in photoinitiated processes taking place around us, it is remarkable how nature's design performs these tasks with a very restricted variety of molecules.

Chlorophylls, carotenoids, xantopsins, and flavins are the work horses in harvesting solar energy for biological usage. The absorption wavelengths of these "light-harvesting" molecules are tuned through variations in side-groups, interactions with protein residues, and interactions with other photoactive molecules. For instance, in oxygenic photosynthesis (splitting water in hydrogen and oxygen), vast amounts of chlorophylls are arranged in the so-called light-harvesting antennae, whereas the core reaction center PSI (Photosystem I) contains about 100 chlorophyll and 20 carotenoid molecules. Depending on intermolecular distances and orientations the absorbed excitation energy is funneled to the reaction centers by a multitude of energy transfer steps, at times residing on a single molecule, at times existing as delocalized excitonic states.

The origin of both energy transfer and exciton formation lies in intermolecular Coulomb interaction. Even neutral molecules represent an overlay of positive and negative charge density patterns, and the full Coulomb interaction between molecules therefore involves an expansion into a series of dipolar, quadrupolar, etc. interaction terms. Typically, only the dipolar interaction terms are considered, which fall off with the third power of the intermolecular separation; see Sect. 9.2 for the explicit form of this interaction. Whether these dipolar interaction terms give rise to Förster energy transfer or Frenkel exciton formation (in both intermolecular electron exchange is

excluded), depends on the strength of these terms relative to that of other factors, such as IVR, intramolecular population decay (radiative or nonradiative), and optical (pure) dephasing (by coupling to the environment), which may disrupt the intermolecular coupling. If the dipolar coupling is large relative to these dynamic disturbances, electronic excited states of the ensemble of N molecules will be linear combinations of the N-molecule direct product states with one or more of the molecules singly excited. These linear combinations represent delocalized optical excitations known as Frenkel excitons, and form manifolds labeled the one-exciton manifold, two-exciton manifold, etc., depending on the number of singly excited molecules in the N-molecule basis states forming the exciton states. The combined oscillator strength of the N molecules is redistributed over the one-exciton states leading to enhanced radiative decay rates for some of these exciton states. Note that the delocalized exciton states are eigenstates of the N-molecule Hamiltonian, and therefore stationary solutions.

In Sect. 9.4 a theoretical study demonstrates the possibility of shaped pulses (optimal control theory) to manipulate excitonic wave packets, in order to localize an exciton on a specific molecule in the Fenna-Matthews-Olson (FMO) complex, which is part of the photosynthetic apparatus of green bacteria. A mechanism for reaction optimization by the protein environment is presented in Sect. 9.2. There, transient electric field effects on the absorption band of tryptophan units upon optical excitation of retinal inside bacteriorhodopsin is investigated and modeled with excitonic coupling. If a coherent intermolecular coupling is not established one obtains incoherent intermolecular Förster energy transfer [8], which shows a r^{-6} dependence, instead of r^{-3}, because one now considers population transfer (wave function squared), whereas in exciton formation wave function amplitudes are coupled. If the molecules are in close proximity energy transfer involving simultaneous intermolecular electron exchange is possible, which is referred to as Dexter transfer. The strength of this process drops off exponentially with the intermolecular separation (as all wave functions have this distance dependence for their amplitude in common).

Energy transfer is also widely used in medical and analytical applications. In cancer treatment (photodynamic light therapy) energy is used to generate locally high concentrations of singlet oxygen, ultimately leading to cell death. The mechanism of releasing oxygen from molecules with endoperoxide groups is studied in Sect. 9.5. Photoreceptor proteins absorb light by chromophore molecules and convert the energy into biologically useful properties, e.g. proton gradient. The wide use of the green fluorescent protein (GFP) as biological label (see Sect. 9.3), relies on using the extent of fluorescence quenching for conversion of fluorescence quantum yields into a ruler for determining distances on atomic scales. As mentioned above, various chemical and structural changes within the complete chain of a biological process can stretch over a wide range of timescales from femtoseconds to seconds. Many of these changes, which lead to biomolecular conformations or metastable structures

are not accessible with optical spectroscopy, but could lead to characteristic changes in the vibrational spectra. The protein dynamics described by all possible conformations, time scales and couplings would contain a complete set of information to understand the function of proteins. However, an obstacle to calculate metastable conformations is the curse of dimensionality, as typical biomolecular systems contain hundreds or thousands of degrees of freedom. In Sect. 9.6 the Hidden Markov Model approach is applied to reduce the dimensionality of biological systems to a few essential degrees of freedom and to identify metastable conformational structures in time series. The recent developments in time-resolved vibrational spectroscopy make the prospect of combining experimental time-resolved vibrational data with molecular dynamical calculations of metastable conformation an exciting direction for future investigations.

Section 9.7 deals with real-time identification of airborne bacteria using multiphoton excitation, multiphoton ionization and laser induced breakdown with femtosecond pulses to optimize the fluorescence emission of aerosol microparticles. The higher order interaction of the electric field with the bacteria reveals specific spectroscopic data not available in linear spectroscopy and is a key feature for identifying bacteria in urban aerosols. These techniques may prove very useful in future attempts to contain disease outbreaks by bacteria or viruses, such as SARS or anthrax, or straightforward monitoring of levels of typical highly antibiotic resistant bacteria in hospitals.

9.2 Measuring transient electric fields within proteins

S. Schenkl, F. van Mourik, G. van der Zwan, S. Haacke, and M. Chergui

"Electrostatic interactions are the common denominator and probably the most important element in structure-function correlation in biological systems". This citation by A. Warshel [9] stresses the importance of electrostatic interactions for functional dynamics in Biology, previously highlighted by M. Perutz [10]. NMR and X-ray experiments give insight in the dynamical aspects acting on the molecular level by probing the flexibility and highlighting large amplitude motion of atoms. UV-VIS spectroscopy probes electronic transitions and is thus sensitive to light-induced charge redistributions. These determine the dynamic force fields at all time scales, which in return drive the structural changes needed for biological function. The description of electric fields in proteins is still a timely issue to this day [11], in part due to the difficulty of measuring them within proteins. A further degree of complexity is added, when it comes to measuring these electric fields in the ultrashort time domain, where fundamental phenomena occur, that govern the fate of photobiological functions. Indeed, there is no direct experimental evidence for charge displacements in the femtosecond time regime, let alone within a pro-

tein, because photovoltaic techniques cannot be used to detect them if they occur faster than picoseconds, and less so on a sub-nanometer distance scale.

Cohen et al. [12] designed a modified, fluorescent, aminoacid that can be incorporated into proteins. However, the use of naturally occurring molecular groups as local probes of electrostatic effects is preferable. In heme proteins, the CO-ligand has been used as a molecular probe of the electrostatic potential in the distal pocket of myoglobin [13], though not in the time domain. In photosynthesis, the electrochromic response of carotenoid molecules is often used, to measure locally electric fields from the millisecond [14] to the femtosecond [15] time regime.

Systems for which the relation between electrostatic interactions and function is most discussed are retinal proteins and excitonic complexes involved in light-harvesting for photosynthesis. The former play an essential role in a broad range of light-driven biological processes, such as vision, energy transduction and circadian control. All these functions involve both the conversion of light energy into charge separation and retinal isomerization, but the interplay of these processes is the subject of intense debate. The retinal protein of which the initial photochemistry is most extensively studied is the photosynthetic protein bacteriorhodopsin (bR). This protein acts as a light-driven proton pump by means of a multistep process, the so-called photocycle. In the traditional model, the light driven trans-cis isomerization of retinal (Fig. 9.3), is the key primary step in this cycle. However, it is also known that Franck-Condon excitation of all-trans retinal results in an immediate change of permanent isomerization dipole moment by more than 12 D [16, 17], causing a sudden polarization of retinal. It has been suggested that the dielectric response of the protein, might be the primary light-induced event [18, 19] that could drive structural changes on longer time scales [20]. In addition, it is well established that the specific protein environment enhances the yield and the stereo-selectivity of the isomerization [21], when compared to retinal in solvents. However, the actual charges and dipoles that create these favorable electrostatic properties in bR still need to be identified.

Ultrafast transient absorption studies of bR and its mutants with non-isomerizable retinal chromophores, show identical dynamics in the first 200 fs after optical excitation [22]. Isomerization, i.e. a C13-C14 dihedral angle > 90 , thus occurs on a time scale longer than 200 fs. This conclusion is supported by transient absorption studies on wild type bR using 5 fs pulses [23], suggesting that a skeletal change occurs in the first 200 fs, which corresponds to a large twisting about the C13-C14 bond, prior to isomerization. Similar conclusions were drawn from stimulated Raman studies showing a decay of the high frequency C=C, C-C and methyl rock modes in $\sim$250 fs [24]. Femtosecond vibrational spectroscopy shows that isomerization occurs indeed later ($\leq$500 fs) and is followed by a slower vibrational relaxation of the isomerized photoproduct (the so-called J to K transition) [7, 24–26].

González-Luque et al. [27] computed the distribution of charges in the S_1 excited state, as a function of the isomerization coordinate of model chro-

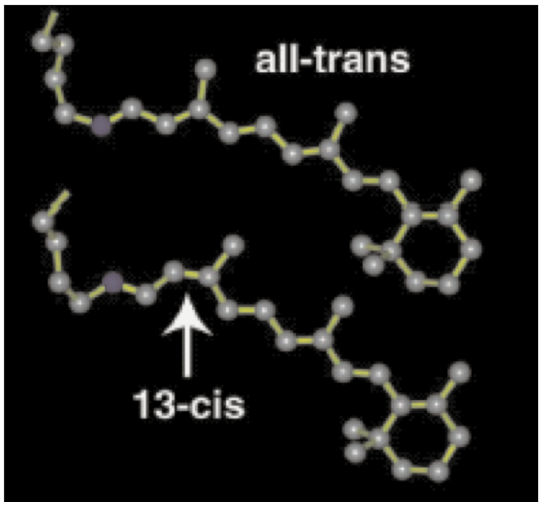

Fig. 9.3. Cis-Trans light-induced isomerization of the retinal chromophore in bacteriorhodopsin

mophores of rhodopsin and bacteriorhodopsin. The computed dipole moment of the S_1 state, increases along the isomerization coordinate of the chromophore, confirming an earlier suggestion by Salem and Bruckman [28]. It thus appears that while there is no isomerization in the first 200 fs or so, the system undergoes a large dipole moment change upon photoexcitation, followed by a translocation of charge. However, the time scale of the latter and its interplay with the initial twisting and subsequent isomerization are still unknown. Direct measurements of the charge separation process using photovoltaic techniques have been performed [29, 30]. However, the intrinsic temporal resolution of these techniques is limited to several picoseconds, i.e. slower than the ≈500-fs isomerization process. To visualize the electronic response of bR on a short time scale, Groma et al. [31] recently reported a different approach, based on a nonlinear technique: interferometric detection of optical rectification. The second order susceptibility $\chi^{(2)}$ of the retinal chromophore is unusually high, especially in its native protein environment, and this property has been shown to be a requirement for functioning of bR [32]. These strong nonlinear properties give rise to optical rectification [33], among others, in non-centrosymmetric crystals. Groma et al. [31] used it in the case of oriented bR crystal films and measured an impulsive macroscopic polarization, which they associated with the charge separation.

In order to measure more specifically the translocation of charge within a protein, we recently implemented an approach that uses the natural tryptophan (Trp) residues of the protein (bR in this case), as a sensor of the electric field changes associated with excitation of retinal and translocation of charge. Literally, all proteins contain Trp amino-acid residues, which are highly po-

larizable and can be used as sensors for intra-protein electric field changes. Therefore, the description of our results on bR should represent a test case that can be extended to other classes of proteins.

9.2.1 Origin of the transient electric fields

Four tryptophans are in the vicinity of retinal in the binding pocket of bR (Fig. 9.4A) [34, 35]: Trp86 and Trp182 sandwich retinal, while Trp138 and Trp189 are located in the vicinity of the β-ionone ring. The absorption spectrum of bR (Fig. 9.4B) exhibits a band in the visible, due to retinal, and a band near 280 nm, predominantly due to the eight Trps present in the protein. The Trp absorption is due to transition from the ground state to the lowest two close-lying excited states (labeled L_a and L_b) of the indole moiety. The transition into the L_a state implies a large difference dipole moment with respect to the ground state [36], making the Trp's particularly well-suited molecular-level sensors of electric field changes within the protein, as the latter are expected to cause large changes in their spectral features. Note that a $\sim$ 10 D dipole on retinal creates a field of $\sim$10 MV/cm on the nearby amino acids.

In retinal the positive charge from the protonated Schiff base linkage with Lys216 (Fig. 9.4) is partially moved toward the ionone ring upon excitation. To probe the electric field changes associated with the charge translocation in retinal, we have excited the latter at 560 nm, and interrogated the Trp absorption changes with 80-90 fs time resolution, using tuneable near-UV pulses, from a noncollinear optical parametric oscillator. The details of the set-up are given in [37, 38]. Our approach has two advantages: (a) in contrast to experiments in the VIS or IR, that probe retinal directly [7, 23–25], the charge displacements become detectable with high sensitivity through an electric dipole interaction in the UV, (b) the local electric field changes are followed in real-time from femtoseconds to picoseconds (ps) or more.

Results and discussion

Figure 9.5A shows the transient absorption changes, detected between 265 nm and 280 nm. The traces are normalized, highlighting their similar shape over the whole range of probe wavelengths. The presence of a rise time is directly deduced from the temporal derivative of the bleach transient (Fig. 9.4B). Its full width at half maximum (FWHM) of 150 fs is significantly larger than the 80-90 fs pump-probe cross-correlation.

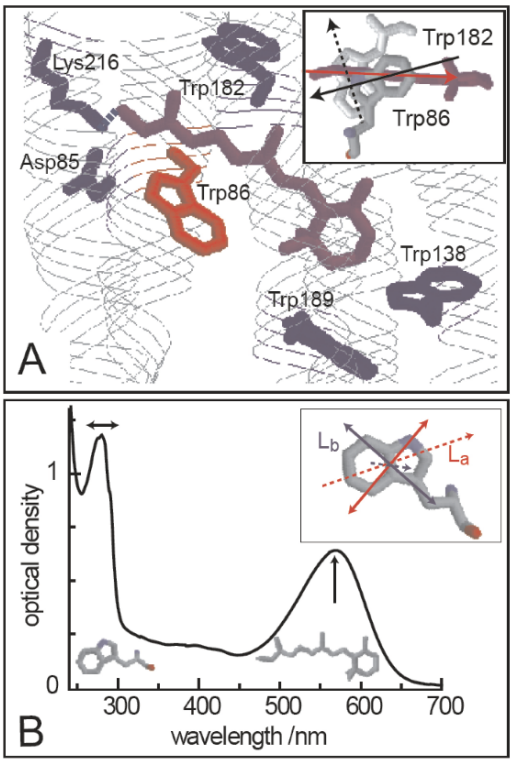

Fig. 9.4. Structure and spectral properties of bacteriorhodopsin. A) The retinal binding pocket of bacteriorhodopsin [35]. Retinal (purple) is covalently bound to Lys216 through a Schiff base linkage. The four nearest Tryptophan (Trp) residues are shown. Insert: Relative orientations of the difference dipole moments for retinal (red arrow), of Trp 86 (full black arrow) and Trp182 (dashed black arrow). B) Absorption spectrum of bR in the purple membrane. The band with maximum at 568 nm is due to the S_0-S_1 transition of the protonated Schiff base form of retinal, while the near-UV band at 280 nm is dominated by the S_0-L_a and S_0-L_b transitions of eight Trp's. The vertical arrow indicate the excitation wavelength and the horizontal one the range of probe wavelengths. Insert: Orientations of the transition (full arrows) and difference (dashed arrows) dipole moments of tryptophan for S_0 - L_a (red) and S_0 - L_b (blue) [36]. Arrows point to the positive end of the difference dipole moment.

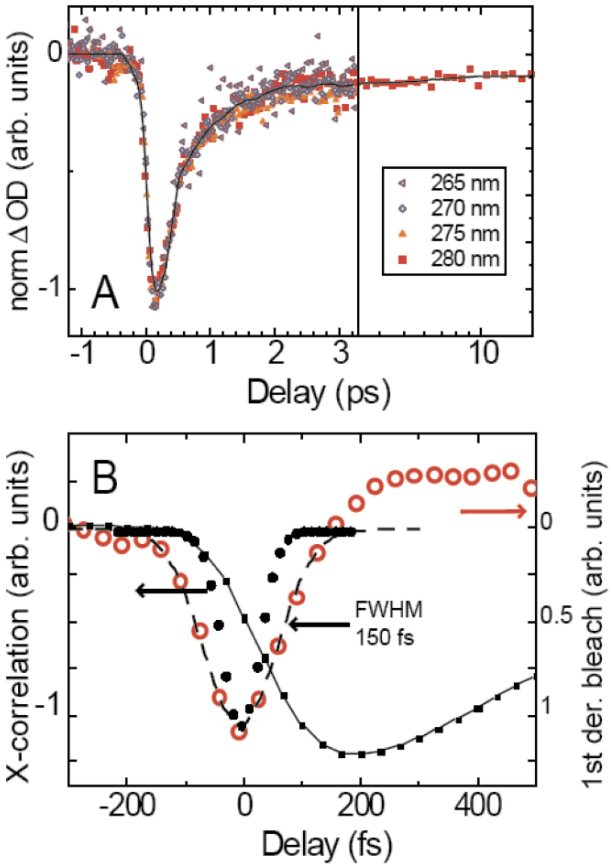

Fig. 9.5. Ultrafast response of bacteriorhodopsin in the near-UV. A) Transient bleach signals at 265-280 nm after excitation with 25 fs pulses at 560 nm at 1 kHz repetition rate. UV probe pulses (80-90 fs) were obtained by second harmonic generation of the output of a tunable noncollinear OPA [37, 38]. The transients are normalized in amplitude. The time axis of the left panel is linear, while the right panel has a logarithmic one. B) The early time portion of the bleach transient in fig. 9.4A (black squares), and its temporal derivative (red circles) showing a full width at half maximum (FWHM) of 150 fs. The latter is clearly larger than the experimental time resolution of 85 fs (black dots) determined by the pump-probe cross-correlation [38].

For longer times, we observe a biexponential recovery of the absorption with time scales: $\tau_1 = 420$ fs, $\tau_2 = 3.5$ ps, which have been reported in experi-

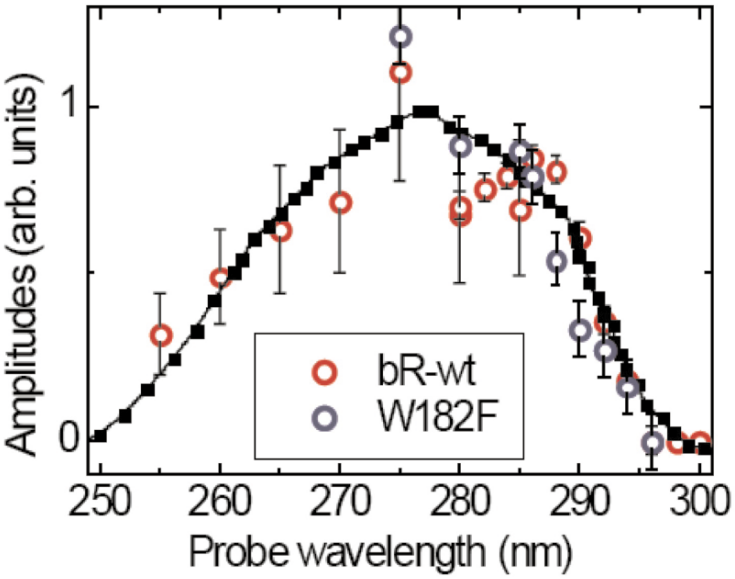

Fig. 9.6. Maximum amplitude of the bleach transients of wild type bR and of the W182F mutant, as a function of the probe wavelength. Experimental data (circles) are compared with the L_a absorption component of Trp in propylene glycol at - 50 C [39] (black squares). To account for the apolar character of the binding pocket, the L_a absorption was shifted by 5 nm to the blue. The data have been normalized to the Trp L_a spectrum at 285 nm.

ments that probe retinal directly [7, 24, 25]. A constant, weak bleach signal is also observed at the longest delay times (τ_∞).

In [37], several arguments are presented, which allowed an unambiguous assignment of the bleach signal to the response of Trp residues, not the least of them being the fact that the wavelength dependence of the bleach amplitude maps reasonably well the Trp L_a absorption spectrum (Fig.9.6). More specifically, we could show that the signal was due to Trp86, by repeating the experiment with a mutant that lacked Trp182, obtaining the same results as with the wild type (Fig. 9.6). This makes sense since the linear polarization anisotropy of the signal is high (0.30 ± 0.05), meaning that the responding Trp transition dipole is almost parallel to the transition dipole moment of retinal along the conjugate chain, as is the case for the L_a state of Trp86 (insert Fig. 9.4A).

A dielectric response of Trps through reorientation of their dipoles is unlikely to account for the rise time, as the polarization anisotropy is constant throughout the time scale of the transients. In addition, the fast inertial

relaxation of indole-like molecules is slower, even in liquids [40]. Rather, we attribute the bleach to the above-mentioned large dipole moment change of retinal. The rise time of the bleach signal (Fig. 9.5B) then reflects the instantaneous dipole moment change and an ensuing gradual charge translocation along retinal. However, the Trp response does not resemble a difference spectrum that was to be expected in the case of a pure Stark shift of the L_a transition. As a matter of fact, the bleach component does not have a positive counterpart with comparable amplitude at nearby wavelengths. As shown in [37], and briefly described below, the difference spectrum is rather dominated by the effects of excitonic coupling resulting from the resonance interaction of retinal and Trp at ∼280 nm, meaning that oscillator strength borrowing can occur between retinal and the Trp chromophores.

9.2.2 A model of three coupled chromophores

In our model, we consider a system consisting of three coupled chromophores, having three electronic levels each: S_0, S_1, S_n for retinal and, S_0, L_a and L_b for Trp86 and Trp182. They form an excitonic complex, whose proper electronic states are linear combinations of the singly-excited near UV states of $|L_{a,b},0,0>$, $|0,L_{a,b},0>$ and $|0,0,S_n>$ (product basis notation |Trp86, Trp182, retinal>), of which three are important (X_1 trough X_3, see Fig. 9.7), as a result of favorable relative orientations of the transition dipole moments. The doubly excited states (XX_1 and XX_2) with retinal in the S_1 state, arise from linear combinations of $|L_{a,b},0,S_1>$ and $|0,L_{a,b},S_1>$ (Fig. 9.7).

Since the L_a and L_b levels of Trp are nearly degenerate, we took their transition energies to be both at 280 nm (35 714 cm^{-1}). Retinal was modeled, with all dipole moments along the retinal backbone. S_1 corresponds to the first excited state and S_n to the excited state resonant with the Trp absorption (also fixed at 280 nm [41]). The interaction between the chromophores can be modeled by their dipole moment operators. The full dipole operator can be expressed as

$$\begin{aligned}\hat{\boldsymbol{\mu}}_{trp} = \boldsymbol{\mu}_0 \mid 0 < 0 \mid + \boldsymbol{\mu}_a \mid L_a >< L_a \mid + \boldsymbol{\mu}_b \mid L_b >< L_b \mid + \\ \boldsymbol{\mu}_{0a}[\mid 0 >< L_a \mid + \mid L_a >< 0 \mid] + \boldsymbol{\mu}_{0b}[\mid 0 >< L_b \mid + \mid L_b < 0 \mid]\end{aligned} \tag{9.1}$$

where the first three terms correspond to the permanent dipole moments, and the next two to transitions between the ground and the excited states. The dipolar interaction is accounted for by the usual interaction energy between two dipoles $\boldsymbol{\mu}_1$ and $\boldsymbol{\mu}_1$ at positions $\boldsymbol{r}_1$ and $\boldsymbol{r}_2$ respectively:

$$V_{12} = \frac{1}{4\pi\varepsilon_0\varepsilon_r r_{12}^3}\left(\boldsymbol{\mu}_1 \cdot \boldsymbol{\mu}_2 - 3\frac{(\boldsymbol{\mu}_1 \cdot \boldsymbol{r}_{12})(\boldsymbol{r}_{12} \cdot \boldsymbol{\mu}_2)}{r_{12}^2}\right) \tag{9.2}$$

where $\boldsymbol{r}_{12} = \boldsymbol{r}_1 - \boldsymbol{r}_2$ and $r_{12} =\mid \boldsymbol{r}_1 - \boldsymbol{r}_2 \mid$, and ε_r is the relative dielectric constant of the protein environment (in these calculations we set $\varepsilon_r = 1.5$,

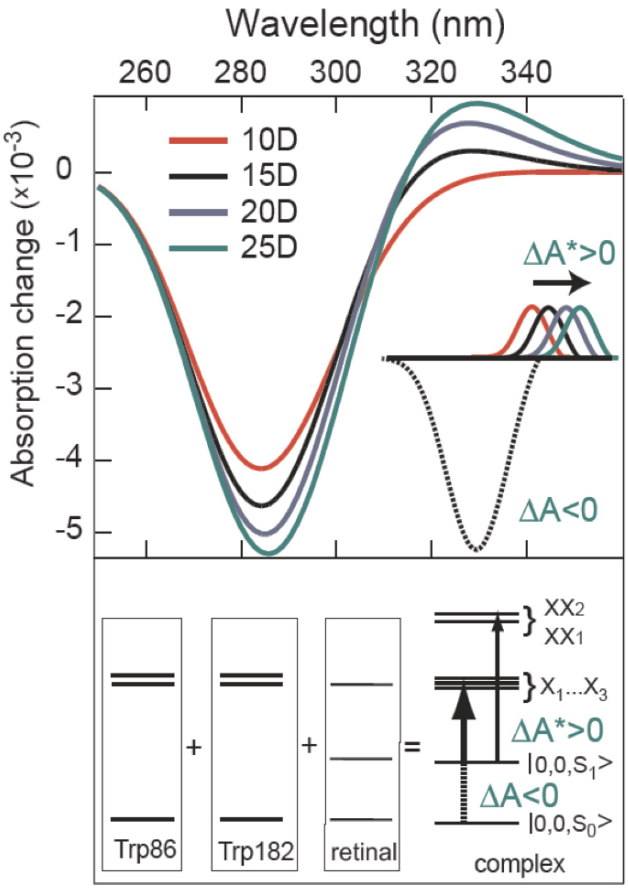

Fig. 9.7. Top panel: Calculated difference absorption spectra as a function of the retinal difference dipole moment $\Delta\mu$ and its decomposition (scheme on the right) in terms of a bleach contribution (ΔA<0) and a $\Delta\mu$-dependent absorption (ΔA*>0). Bottom panel: Dipole-dipole coupling of Trp86, Trp182 and retinal leads to the formation of an excitonic complex with proper electronic states [37]. The X_i's represent singly excited states of the excitonic complex, with one excitation per chromophore, while the XX_i's represent doubly excited states with retinal in the S_1 state. Photoexcitation of retinal attenuates the transition to the $X_1 \ldots X_3$ states (ΔA<0), due to the bleach of the $\mid 0,0,S_0$ (product basis notation $\mid$ Trp86, Trp182, retinal $>$) ground state of the excitonic complex. The photoinduced absorption from $\mid 0,0,S_1 >$ reaches the XX_1 and XX_2 states (in which both Trp and retinal are excited), giving rise to an absorption (ΔA*>0). As the difference dipole moment $\Delta\mu$ increases, ΔA* red-shifts due to a lowering of the XX_1 and XX_2 levels (attractive interaction between retinal and Trp86). This leads to an increasing bleach around 280 nm, which is a measure of the retinal difference dipole moment $\Delta\mu$.

to account for the hydrophobic binding pocket). The full interaction operator corresponds to all possible combinations of dipoles between the three pigments, i.e. we evaluate the interaction energies [36] with the dipole operators $\hat{\mu}_{\mathbf{trp86}}$, $\hat{\mu}_{\mathbf{trp182}}$, $\hat{\mu}_{\mathbf{ret}}$ expressed in analogy to [42]. In the case of the three chromophores, the total dipolar interaction is taken as the sum of pairwise interactions. The first three terms in (1) will give rise to the Stark effect, while the last four give rise to the resonance interaction. Thus we can form the full interaction Hamiltonian H = H_0 + V of the three (27x27 matrix) or of two (9x9 matrix) interacting chromophores. H_0 is the Hamiltonian of each isolated chromophore and V represents the dipole-dipole interaction between the chromophores. Diagonalization of this Hamiltonian by standard methods gives a set of eigenvalues, from which new transition energies can be found, and eigenvectors, from which new transition dipole moments can be determined. As illustrated in Fig. 9.7 (bottom panel), this gives rise to a single ground state ($\mid 0,0,S_0$) and a single excited state ($\mid 0,0,S_1>$) close to 570 nm (17 540 cm^{-1}). The exciton manifold consists of the five states $\mid L_{a,b},0,0>$, $\mid 0,L_{a,b},0>$ and $\mid 0,0,S_n>$ (in the product basis notation |Trp86,Trp182, retinal>), derived from the single excitations to the original levels absorbing at 280 nm (35 714 cm^{-1}). It is represented by the three dominant transitions X_1, X_2, and X_3, which are separated by a Davydov splitting of ∼270 cm^{-1}. The double excitation of retinal and Trp's ($\mid L_{a,b},0,S_1>$ and $\mid 0,L_{a,b},S_1>$) leads to an exciton manifold of four states around 52 000 cm^{-1} with two dominant ones, labeled XX_1 and XX_2.

Stick spectra are generated from the transition energies and intensities. The latter are determined by the respective oscillator strengths, which are proportional to the square of the transition dipole moments. Gaussian broadening of 3500 cm^{-1} (FWHM) is assumed, a spectral broadening commonly observed for Trp and retinal transitions in proteins. Thus, the UV ground state absorption spectrum is dominated by the transition from $\mid 0,0,S_0>$ to X_1, X_2 and X_3, while the excited state spectrum, i.e. with retinal in the S_1 state, is due to the transitions from $\mid 0,0,S_1>$ to XX_1 and XX_2 (Fig. 9.7, bottom). The difference absorption spectrum is obtained by subtracting the ground state spectrum from the excited state spectrum. For low $\Delta\mu$ ($\leq 10D$), the ground and excited state spectra almost compensate, leading to a small negative difference signal around 280 nm (Fig. 9.7, top).

The simulated absorption changes are plotted in Fig. 9.7 (top panel) for various values of the retinal difference dipole moment $\Delta\mu$. The photoinduced signal in the region of Trp absorption indeed appears as a bleach of the excitonic transitions into the X_i levels (the bleach character arises from the depletion of ground state retinal due to excitation with the pump pulse), while transitions from $\mid 0,0,S_1>$ to XX_i levels show up as a positive signal on the red side. As the retinal difference dipole moment $\Delta\mu$ acts only when the system is in the $\mid 0,0,S_1>$ state, the position of the induced absorption ΔA* red-shifts with increasing difference dipole moment, while the ground state bleach A is $\Delta\mu$-independent. The red shifting of ΔA* is due to an

attractive interaction between the excited state dipole moments of Trp86 and retinal (insert Fig. 9.3), with the latter's varying in time. The signal is the sum of ΔA and ΔA*, and it results in an increasing bleach signal with increasing $\Delta\mu$ (Fig. 9.7), as observed. The bleach amplitude at 280 nm is therefore a measure for the retinal difference dipole moment $\Delta\mu$.

Based on the calculations that link the amplitude of the bleach signal to the retinal difference dipole moment, the additional rise time of the experimental bleach transients appears to reflect a progressive increase of $\Delta\mu$, on a time scale of 200 fs after excitation. The dipole moment change is due to the translocation of charge, for which we measure the time scale for the first time. Given that the events at $t < 200$ fs are also characterized by large amplitude torsional motion of the retinal skeleton, prior to isomerization [23,24], we conclude that the dipole moment increase is related to these structural changes, as also predicted by quantum chemistry calculations [27]. In an intuitive picture, the torsional motion breaks the conjugation at the C13-C14 bond and thus localizes the charges on the left and right of that bond, which leads to a dipole moment increase. A similar situation is encountered in donor-acceptor molecules like DMABN, where the build-up of a charge transfer state involves rotation of the dimethyl amine with respect to the phenol moiety [43, 44]. In the protein environment, the gradual dipole moment change of retinal in the excited state then acts as driving force for the torsional motion, because the electrostatic interactions are attractive [45, 46].

At later times (400-500 fs), the difference dipole moment decreases. This is the time scale of formation of the 13-cis isomer [7], pointing to a weaker dipolar interaction in the ground state 13-cis retinal than in excited all-trans retinal. Since the isomerization leads to an electronic ground state, with a mainly covalent character as in the all-trans adduct state [27], the dipole moment change is small, and so is the remaining bleach signal. The additional 3.5 ps decay component, which is similar to the vibrational relaxation in the 13-cis photoproduct found in experiments probing retinal [24–26], suggests a further decrease of the dipolar interaction. Vibrational relaxation leads to a weak displacement of the center of gravity of the charge, which may cause the decrease in dipole strength. Alternatively, energy dissipation may cause structural changes in the retinal binding pocket, which modify the field detected at the location of Trp86. Finally, the weak bleach component at longer times (τ_∞) points to long-lived changes in the structure of the pocket and/or the dielectric constant, which may relate to changes detected in the picosecond range in mid-IR experiments [7].

In summary, we have measured the light-induced electric field changes within a protein (bacteriorhodopsin), following them over the whole course of the dynamics from the Franck-Condon region to the vibrationally relaxed photoproduct. Our observations allow us to establish the connection between the translocation of charge [27] and the skeletal changes of the conjugate chain [23]. The present work also stresses the role of the dynamic electric force fields, which drive structural dynamics and govern enzymatic reactions.

9.3 Multipulse transient absorption spectroscopy: A tool to explore biological systems

M. Vengris, D. S. Larsen, E. Papagiannakis, J. T.M. Kennis, and R. van Grondelle

Light-driven events in biological systems are triggered by the absorption of a photon in pigment-protein complexes, which eventually produces a physiological response. Even though the light is absorbed by the pigments (chlorophylls, carotenoids, xantopsins, flavins, etc.), protein environment plays a key role in the absolute majority of these processes: the protein determines the course of the photoinduced reactions by 'guiding' the excited pigments along the reaction pathway, and, at some stage, taking over all the reaction functions, which then no longer rely on the physicochemical properties of the pigment. For the photoinduced reactions to be efficient, their rates must compete effectively with the lifetime of electronic excitation in the molecules (usually of the order of several ns for singlet excited states), which makes these reactions the subject of ultrafast laser spectroscopy. In photoreceptors the protein environment plays a key role in the absolute majority of light-related biological processes: the protein determines the course of the photoinduced reactions by 'guiding' the excited pigments along the reaction pathway, and, at some stage, takes over all the reaction functions, which then no longer rely on the physicochemical properties of the pigment.

Pump-probe (PP) spectroscopy (see Chaps. 2 and 8), is probably the most widely used ultrafast technique to investigate photoinduced reactions [47]. Pump-probe data are usually presented in the form of time-resolved difference spectra, i.e. $\Delta OD = \Delta OD(t, \lambda)$, where ΔOD is the difference between the sample absorbance with and without the pump pulse (Fig. 9.8). The absorption-difference (ΔOD) spectra measured in pump-probe experiments are shaped by a number of qualitatively different contributions that may originate from transitions between the different states of the system (Fig. 9.8), e.g. ground state bleach (GSB), stimulated emission (SE) and induced absorption (excited state absorption, ESA, or absorption by nonequilibrated ground state). Without additional experimental information, when no additional control is exerted on the sample, these contributions often become impossible to distinguish one from another and the data interpretation becomes ambiguous.

9.3.1 Multipulse transient absorption spectroscopy: The principles

The difficulties of traditional PP experiments can be addressed using multipulse transient absorption spectroscopies (MPTAS), such as the dispersed pump-dump-probe (PDP) and the pump-repump-probe (PrPP) techniques, which involve the introduction of a third pulse to the PP experiment (Fig. 9.9)

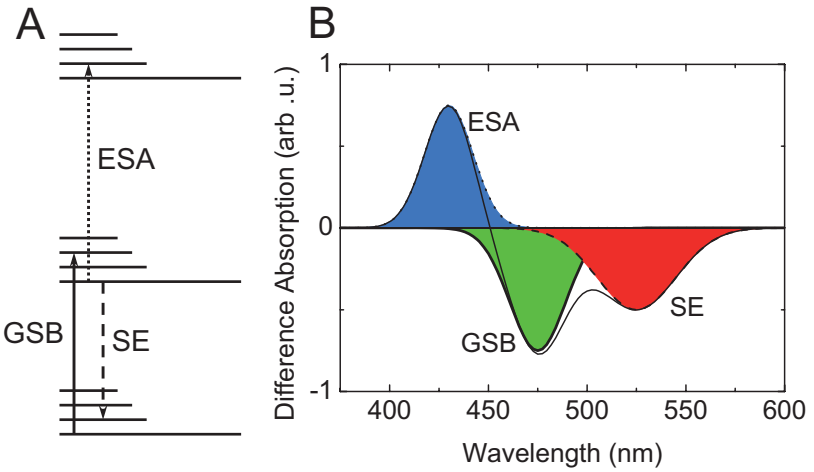

Fig. 9.8. The energy level scheme (A) of a hypothetical molecule and different transitions influencing the pump-probe spectrum (B): ground state bleach (GSB), stimulated emission (SE) and excited state absorption (ESA). By tuning the third pulse of a laser into the resonance with ESA and SE bands, a means of controlling the photoreaction can be established. In the case of the third pulse acting on ESA, pump-repump-probe technique (PrPP) is obtained, whereas if the third pulse is in resonance with SE, the technique is called pump-dump-probe (PDP).

[48, 49]. This additional pulse can be appropriately wavelength-tuned and delayed to selectively interact with a 'targeted' electronic transition. In PDP experiments, this added pulse interacts with the SE of an excited state and results in the de-excitation of molecules and the transfer of population from the excited state to the ground state. In PrPP experiments, the additional pulse interacts with an ESA band and causes the redistribution of population within the excited state manifold whilst the total amount of excitations is preserved, i.e. the ground state population remains unaffected.

Ultrafast single-wavelength PDP experiments were previously used to study the properties of the excited states in bacteriorhodopsin [50, 51], and to explore ground state dynamics in calmodulin [52]; asymptotic-limited dispersed PDP has been used to study ground state liquid dynamics [53]. The higher excited-state dynamics of bacteriorhodopsin has been studied by single-wavelength PrPP [54] and the combined use of PDP and PrPP allowed the distinction of overlapping bands in the PP signals [50]. In the recent years, the MPTAS techniques have been further developed to include dispersed detection [48, 49], which allows the simultaneous probing of complete spectra with an unprecedented signal-to-noise ratio, that subsequently can be analyzed globally [55–57]. This development, which allowed to test explicit physical models for light-driven biological processes, moved ultrafast research on biological systems to a qualitatively new level.

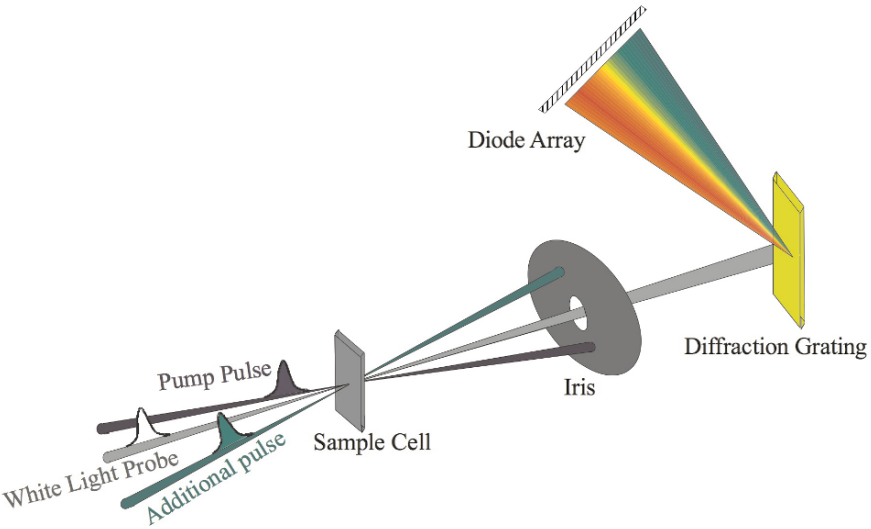

Fig. 9.9. Laser beam arrangement in the multipulse transient absorption experiment. The additional pulse can be tuned to be in resonance with excited state absorption or stimulated emission (see Fig. 9.8).

The utility of MPTAS spectroscopies lies in their ability to control reactions as they evolve, by manipulating the population of transient species with applied laser pulses. This is, to a certain extent, related to coherent control mechanisms where reactions are manipulated via complex processes such as vibrational wave packet motion, quantum interferences and electronic coherences [58]. A more appropriate term for describing MPTAS spectroscopies is incoherent control, because the control effects are achieved and the data is interpreted solely in terms of manipulated electronic state populations. This simplification, as will be shown in the following applications, allows for clear, concise and biologically relevant interpretations of the measured data.

The important aspects of biological pigment-protein systems, where MPTAS can resolve issues that remain obscure in conventional ultrafast spectroscopic experiments, can be summarized in the following list:

• MPTAS can help to attribute specific bands in the transient absorption spectrum to either ground or excited-state reaction intermediates. In a PDP experiment, excited state population is diminished via the dumping of SE by the second pulse. If a specific spectral band measured by the third pulse is diminished as well, one can safely conclude that this band originates from the excited state; if, however, it increases in magnitude, it must come from the ground state.

• MPTAS can be used to determine the pathway of the excited-state evolution of a light-driven biosystem by providing the ability to perturb it (both

dumping and re-pumping the excited state). For example, if the excitation pulse initiates two parallel processes, only one of which leads to a specific photoproduct, the additional pulse can be used to selectively perturb one 'branch' of such a reaction and observe which spectroscopic intermediates originate from that particular pathway.

• If some intermediates of a photoreaction are very short-lived and do not accumulate significant population during the reaction course, the excited and ground state populations can be 'artificially tweaked' using pump and dump pulses and thereby used to selectively populate specific intermediates. This allows monitoring the desired photoreaction steps (and measuring the spectra of transient products) with great precision and selectivity.

• Finally, since MPTAS involves multiple interactions between the sample and the excitation pulses, it can be used as a tool to explore the interaction between excited states in multichromophore systems [59, 60].

In the following subsections we will discuss a variety of biological applications of MTAPS, where all of the mentioned advantages of these spectroscopies will be exploited, but first we will discuss several issues of experimental arrangement, data collection and analysis.

Experimental layout

The principal scheme of MPTAS experiment is shown in Fig. 9.9. Because two excitation pulses are used along with dispersed detection, MPTAS measurements generate multidimensional data (two time delays and one wavelength dimension), which can be collected and presented in two different ways (Fig. 9.10) [48,49]. In a kinetic trace measurement (Fig. 9.10B), the additional pulse is placed at the selected delay (called 'dump-delay' in the case of PDP measurement) after the pump pulse and remains fixed during the measurement. The dump-delay corresponds to a specific distribution of excited-state population and thus determines the effect that will be induced. The delay of the probe pulse is scanned as in PP measurements and records the effect of the dump pulse on the spectrum and dynamics of the PP signal. Alternatively, the dump-induced dynamics can be explored by measuring an action trace (Fig. 9.10C) [48,49], in which the delay of the additional pulse is scanned whilst the probe pulse is maintained at a selected delay. An action trace monitors how the PP spectrum at the chosen probe delay changes as a consequence of the interaction of the additional pulse with the system at variable instances. An additional advantage of an action trace is that it is not affected by time-zero artifacts (e.g. cross-phase modulation, stimulated Raman scattering, 2-photon absorption etc.) because the probed signal is at a much longer delay, allowing clear observation of the dump-induced dynamic changes at early times.

Data presentation and analysis

Here we will briefly discuss the data of PDP experiments only; the same discussion is valid for PrPP experiments, because the two experiments do not

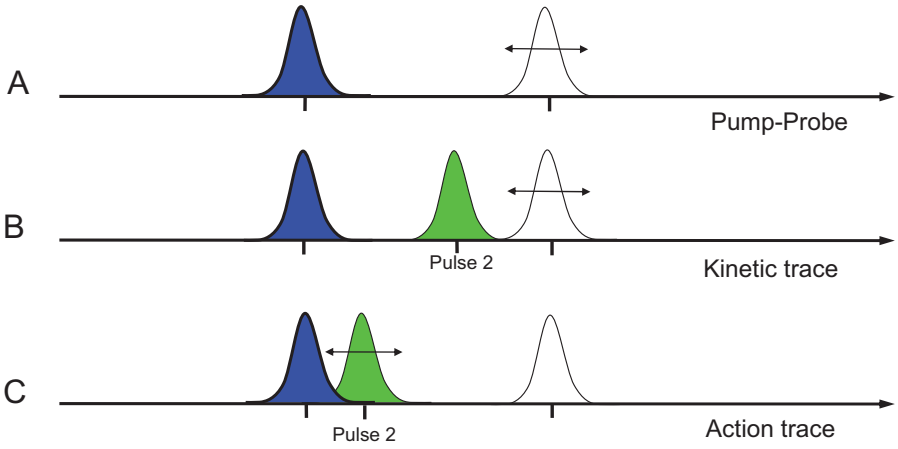

Fig. 9.10. The timing schemes in MPTAS experiments. The pump pulse is represented in blue, the probe pulse is shown in white, and the additional pulse in green. In the pump probe experiment (A) and MPTAS kinetic trace (B), the delay of the probe is varied whereas the actinic pulses are kept at fixed delays. In the action trace (C), pump and probe pulses are fixed at certain time delays and the delay of the additional pulse is varied.

differ in the way the data is collected, but in the nature of interaction between the additional pulse and the sample. Along with the ΔOD signals measured without (PP) and with (PDP) the dump pulse, the double-difference signals are constructed

$$\Delta\Delta OD(\lambda, t, \tau) = PDP(\lambda, t, \tau) - PP(\lambda, t)$$

where λ and t represent the probe wavelength, and delay and τ is the delay of the dump pulse. The $\Delta\Delta OD$ signal is often easier to interpret as it has non-zero amplitude only when there is a dump-induced effect on the PP measurement. However, the time dependence of $\Delta\Delta OD$ signals inherently contains the dynamics of the underlying PP signal; to examine the occurrence of additional, dump-induced dynamics, we can construct the relative double-difference signal, representing a fractional change of PP signal due to additional pulse:

$$\Delta\Delta OD_{rel}(\lambda, t, \tau) = \Delta\Delta OD(\lambda, t, \tau)/PP(\lambda, t)$$

In order to take full advantage of the time- and wavelength resolved experimental data and quantify the observed dynamics, global and target analysis methodologies are instrumental [55–57]. They allow the concise parameterization of results, as well as testing a specific physical model to describe the observed dynamics. For the preliminary parameterization description of the PP signals alone, a sequential scheme is used, where the components interconvert

unidirectionally with increasing exponential lifetimes; it provides estimates of the characteristic timescales for spectral evolution and the corresponding evolution-associated difference spectra (EADS) [56,57]. The EADS estimated from such a scheme do not necessarily reflect pure transient states occurring in the experiment but rather provide a phenomenological description of the observed spectral evolution. To estimate the species-associated difference spectra (SADS) that portray the real states of the system, the PDP data is subsequently analyzed simultaneously with the PP data by applying a specific physical model in a so-called 'target analysis' [56,57]. In this description of the data, a connectivity scheme (physical model) is chosen with each of its compartments depicting a true physical state of the system. The model applied in a target analysis is designed to make physical sense, to produce plausible spectra and (of course) to represent the experimental data well.

In the following we will discuss three applications of MTAPS to biological systems, including proton transfer in the green fluorescent protein, the excited state decay in photosynthetic carotenoids and the initial events in photoactive yellow protein, leading to formation of the signaling state. These cases are selected to illustrate different aspects of how MPTAS can be used to get new insights in the photoinduced dynamics of the molecules.

9.3.2 Uncovering the hidden ground state of green fluorescent protein

In the last decade, green fluorescent protein (GFP) has become the fluorescent label of choice in cell biology and biophysics [61]. GFP absorbs primarily in the near-UV (the main absorption band attributed to a so-called state A of GFP peaks at around 400 nm), but fluoresces in the green (the fluorescence maximum lies near 510 nm). It is generally accepted that the large shift of the emission to longer wavelengths after near-UV absorption is caused by a deprotonation reaction of the neutral chromophore in the excited state [62]. Upon excitation of the state A band with near-UV light, the chromophore deprotonates on a picosecond timescale and subsequent proton transport occurs, most likely via a hydrogen-bonded network that involves an internal water molecule (W25) a serine residue (S205) and a terminal proton acceptor, an ionized glutamate (E222) [63]. The thus formed intermediate state, with a deprotonated, anionic chromophore and a protonated, neutral glutamate is generally referred to as I^* and is the emitting state of GFP, responsible for the green fluorescence around 510 nm. An anionic ground state species, which has been labeled I, can be stabilized and photoconverted back to A at cryogenic temperatures [64]. It has been postulated that the molecular ground state of the chromophore in this anionic form acts as an intermediate in the GFP photocycle [62, 64–67]. However, with time-resolved spectroscopy only the excited states A^* and I^* of GFP could be detected [68], and the molecular nature and dynamics of any ground state intermediate remained elusive.

MPTAS in combination with global analysis was successfully used as a tool to directly measure the ground-state proton transfer dynamics in GFP [69]. By manipulating the excited and ground state populations using an additional femtosecond laser pulse that dumped the excited state I^*, the so far hidden anionic ground state of GFP was shown to be an integral part of the photocycle.

Pump-probe spectra recorded on GFP with excitation at 400 nm are shown in Fig. 9.11. The first spectrum (black line), taken at a delay of 400 fs, exhibits a ground-state bleaching near 400 nm, an ESA band at 440 nm and a broad SE band ranging from 450 to 550 nm. This stimulated emission can primarily be assigned to the excited state of the neutral chromophore, A^*. At progressively increasing time delays, a pronounced SE band with maximum intensity around 509 nm and a shoulder at 545 nm develops. The intensity of the SE signal near 509 nm is a direct measure of the population of I^*, and these results demonstrate the formation of I^* on a picosecond timescale, which corresponds to the deprotonation reaction of the phenolic oxygen of the chromophore [62]. Concomitant with the rise of SE, the excited-state absorption around 440 nm increases, indicating that like A^*, I^* has a pronounced ESA in this spectral region. The transient absorption signal then slowly decays to zero amplitude on a nanosecond timescale (spectra not shown). These dynamics are also reflected in Fig. 9.12A, where the kinetic trace probed at 509 nm is shown (blue squares). The trace shows little signal at early times after excitation. On a timescale of several picoseconds the SE signal rises to a maximum (negative) amplitude. The SE signal subsequently decays to zero in

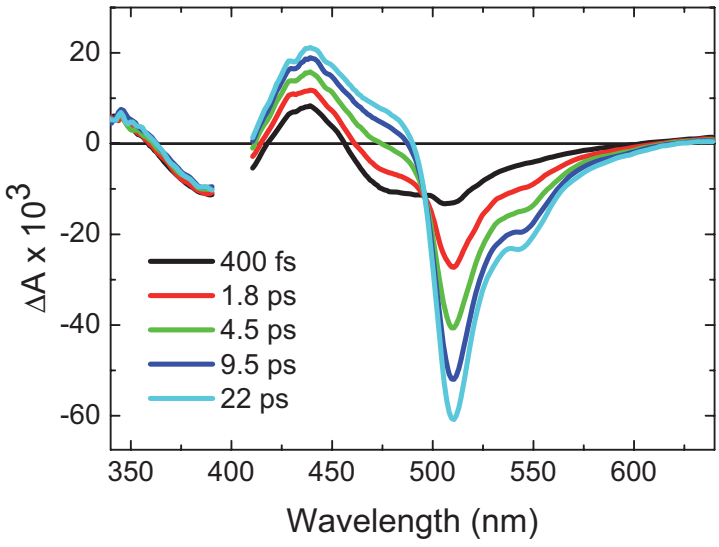

Fig. 9.11. Time-resolved absorbance difference spectra recorded in GFP upon excitation at 400 nm at the time delays indicated.

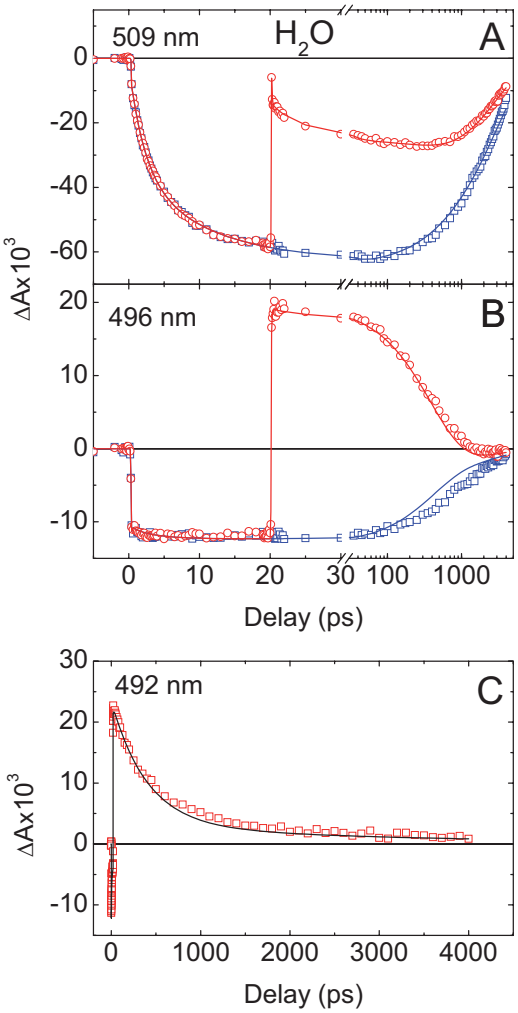

Fig. 9.12. Transient absorption trace at 509 nm (A), 496 nm (B) and 492 nm (C) with excitation of GFP at 400 nm in the absence (blue symbols) and presence (red symbols) of a dump pulse at 540 nm at 20 ps delay. The black thin lines show the result of the global fitting. The time axis is linear up to 30 ps, and logarithmic thereafter in (A) and (B), and linear throughout (C).

about 3 ns, which corresponds mainly to radiative decay of I^* to the ground state [67, 70].

Application of MPTAS to GFP

Pump-dump-probe experiments were performed with the aim to transfer population on a femtosecond timescale from the excited state to the ground state,

thereby overruling the 'slow' 3 ns radiative decay [69]. The red circles in Fig. 9.12A show the kinetic trace at 509 nm in the presence of a short 540 nm dump pulse, which overlaps with a shoulder of GFP's fluorescence spectrum and is fired 20 ps after the 400 nm excitation flash. Up to 20 ps, the trace overlaps with an unmodified (i.e. without dump-pulse) transient absorption trace. At 20 ps, a sudden decrease of the SE signal indicates that the excited-state population has decreased as a result of the action of the dump pulse. Figure 9.12B contains the corresponding kinetic traces measured at 496 nm, showing the appearance of a large induced absorption at 20 ps. This indicates that as a result of the action of the dump pulse, a product species that absorbs at 496 nm is formed concomitantly with the depletion of the excited state. This species corresponds to the ground state of the deprotonated chromophore, *I*, and therefore this experiment clearly demonstrates, for the first time, a ground state intermediate in the photocycle of GFP. Figure 9.12C shows the kinetic trace at 492 nm, where I^* shows an isosbestic point. At this wavelength, the signals exclusively represent the dynamic behavior of the ground state species I (red squares). We observe that after its formation by the dump pulse, the I state disappears rapidly; the smooth curve represents a fit of the data with a single exponential decay of 400 ps. Without the dump pulse the I state remains invisible because it decays about ten times faster than it is formed. To illustrate the spectral evolution induced by the dump pulse, time-resolved spectra at selected delays are shown in Fig. 9.13, measured in the presence (dashed lines) and absence (solid lines) of the dump pulse at 20 ps. As can be seen from the difference spectrum taken at a delay of 22 ps (i.e., 2 ps after the dump pulse, Figure 9.12A), the stimulated emission band of I^* from 509 to 600 nm has been significantly depleted. Moreover, a pronounced new absorption band is observed near 500 nm in the PDP spectrum, along with a 15 nm red-shift of the isosbestic point (at 492 nm in the PP spectrum), indicating the formation of the ground state species upon dumping. Thus, the dumped spectrum is a superposition of the excited state species I^* and the newly formed ground state species *I*. To assess the spectral properties of the ground state species *I*, the difference spectrum of I^* was scaled by a factor of 0.57 (to reflect that an estimated fraction of population 0.43 was dumped to the ground state) and subtracted from the dumped spectrum. The resulting double-difference spectrum (dotted line) corresponds to the 'pure' signal of *I*. At subsequent delays of the probe pulse (450 ps and 900 ps, Fig. 9.13 B and C), the absorption feature near 500 nm decreases significantly and the 'dumped' spectrum starts to resemble the undumped spectrum, indicating that the newly formed ground state species indeed has a significantly shorter lifetime than I^*.

MPTAS data measured in both water and D_2O buffer solutions were globally analyzed. The analysis revealed a pronounced effect of deuteration on the observed dynamics, but virtually no influence on the spectra, as was expected for a proton (or deuterium) transfer reaction [69]. The model used to interpret and quantify the data is shown in Fig. 9.14 (upper panel) along with the tran-

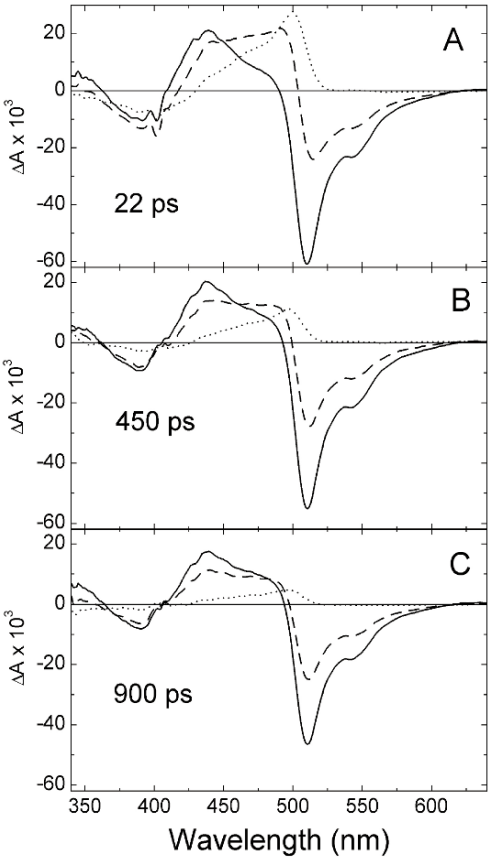

Fig. 9.13. Time-resolved absorbance difference spectra recorded for GFP at the delays indicated after the excitation at 400 nm in the absence (solid line) and presence (dashed line) of a 'dump' pulse at 540 nm, applied 20 ps after the excitation. The dotted lines denote a double-difference spectrum, in which a fraction of 0.57 of the undumped spectrum is subtracted from the dumped spectrum, and denote the 'pure' difference spectra corresponding to the anionic ground state *I*.

sient spectra of the GFP photocycle intermediates (Fig. 9.14, lower panel). Both proton transfer events in the excited and the ground state proceed in a double-exponential fashion, with the resulting species-associated difference spectra virtually identical for H_2O and D_2O solutions. The substantial difference is in the kinetics: the excited- and ground-state proton transfer is 2 and 12 times slower, respectively, when the proton is substituted to deuterium. The estimated proton transfer time in the ground state is 440 ps. The importance of this observation is in the fact that the proton back transfer in GFP occurs in the molecular ground state, as do the vast majority of proton transfers in biology. Thus using MPTAS the 'true', intrinsic rate constant of

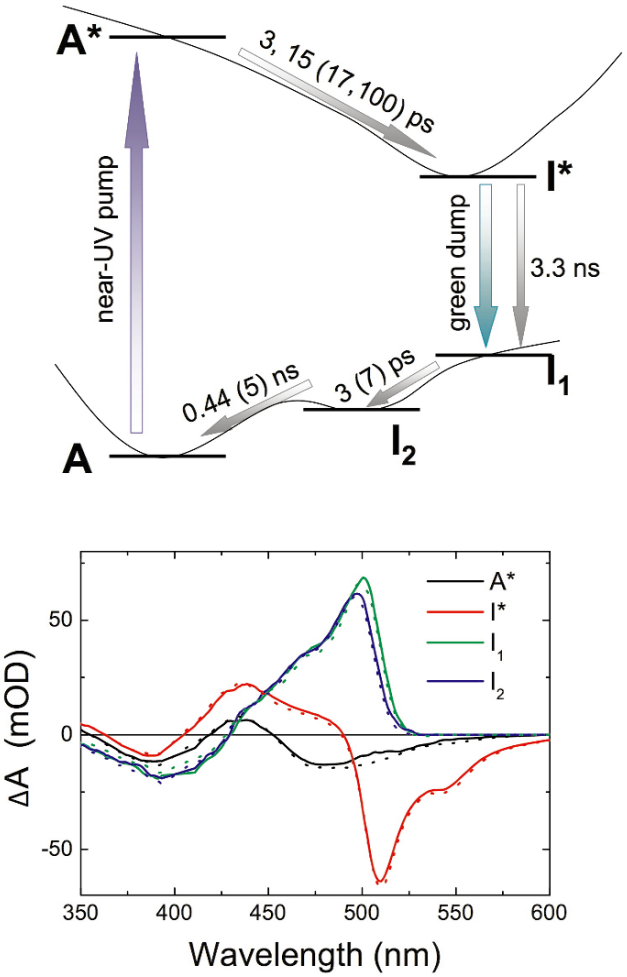

Fig. 9.14. Upper panel: kinetic scheme and potential energy level surfaces representing the photocycle of GFP, to fit the multipulse and traditional transient absorption data of GFP in H_2O and D_2O. The time constants by which the states evolve into one another as estimated from the target analysis are indicated at the arrows, with the values in parentheses representing those obtained for D_2O. Lower panel: Species-associated difference spectra (SADS, [19, 20]) of A^*, I^*, I_1, and I_2 species relative to the A state that result from a target analysis of the time-resolved spectra recorded for GFP in H_2O (solid lines) and D_2O (dotted lines).

the ground state proton transfer in a protein was determined by moving the proton with the first femtosecond pulse to a terminal acceptor, and then 'instantaneously' switching the pK of the donor back to its original value (by applying the dump pulse and returning the donor to the ground state) and watching the proton migrate back. It turns out that the characteristic time of such migration is less than a nanosecond. When using other (chemical) methods than MPTAS, this measured rate is prone to be estimated slower because some steps in the experimental sequence will probably be diffusion-limited and much slower than the intrinsic rate.

9.3.3 Untangling the excited state dynamics of carotenoids

Carotenoids are vital for photosynthetic organisms for light-harvesting and photoprotection, functions that are dictated by their conjugated π-electron backbone. Nevertheless, the molecular mechanisms behind these functions are not fully understood and in fact a concise description of their properties is lacking. Carotenoids typically have a π-conjugation length between 7 and 13 (Fig. 9.15) and their spectroscopic properties are interpreted on the basis of what is known for linear polyenes. Traditionally, their electronic structure has been described as a manifold with two low-lying electronic states: S_2 and S_1 (the $1B_u^+$ and $2A_g^-$ polyene states) [71]. The S_1 state has the same electronic symmetry as the ground electronic state S_0 ($1A_g^-$) and therefore is dark, i.e. it is not observed in the linear ground-state absorption spectrum. The strong absorption of blue-green light corresponds to the transition from S_0 to S_2. The S_2 state is easily observed in fluorescence-upconversion and pump-probe (PP) measurements as it emits in the visible region and absorbs in the near-infrared. S_2 decays by ultrafast ($\sim$200 fs) internal conversion (IC) to the S_1 state, which internally converts to the ground state, with a lifetime that depends on the conjugation length ($\sim$1 to $\sim$100 ps). The S_1 state is easily observed and characterized in PP experiments because of its distinctly strong ESA in the visible [71].

The improvement of ultrafast spectroscopy led to the identification of several features that can not be described in the frame of this simple model and the assignment of newly observed spectral and temporal features in a variety carotenoid-containing systems has been hotly debated. These features include the vibrational cooling of the S_1 and S_0 states, the interference of additional states, such as the $1B_u^-$ and the $3A_g^+$, with the S_2-S_1 relaxation, the branching of S_2 to populate a state S*, which most likely is the precursor to the triplet generation by singlet fission, etc. [71–75]. The electronic character and the spectroscopic properties of these new carotenoid excited states have still to be characterized and integrated into a comprehensive model linking carotenoid structure with function. Clearly, identifying the underlying connectivity of temporally overlapping states is crucial for interpreting their origin and understanding how and why Nature selected and shaped these molecules into

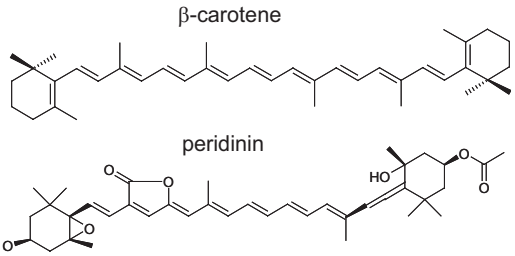

Fig. 9.15. The structural formulae of carotenoids discussed here: β-carotene (top) and peridinin (bottom).

the multifunctional biological pigment as we know them; MPTAS techniques provide the experimental tools to further this understanding.

9.3.3.1 An additional excited state in β-carotene

A comparison of the transient absorption spectra of β-carotene measured 3 ps after excitation at 400 and 500 nm, shows that the excitation at the higher energy side of the S_2 state (400 nm) generates a spectrum with a pronounced shoulder on the blue side (500-525 nm) of the strong ESA of S_1 which peaks at ∼550 nm (green line in Fig. 9.16). This shoulder is absent when 500 nm light is used for the excitation (black line in Fig. 9.16) To address this feature, a series of multipulse experiments were performed [49].

The first was a PrPP experiment; an 800-nm pulse was used to repump population from the S_1 state to a higher excited state, 1 ps after 500 and 400-nm excitation. The effect of the additional 800 nm pulse on the transient absorption spectra is shown in Fig. 9.16 (red and blue lines). When comparing $\Delta\Delta OD$ spectra (red and blue lines) to their respective PP spectra (green and black lines), the effect is markedly different for the two pump wavelengths that were applied. The $\Delta\Delta OD$ spectrum measured with 500-nm excitation (red line) is similar to the respective PP signal in the S_1 region (black line), whereas after 400-nm excitation the $\Delta\Delta OD$ (blue line) lacks the blue shoulder observed in the PP spectrum (green line). If the entire ESA band from 500 nm to 600 nm were due to S_1 state, the shapes of $\Delta\Delta OD$ and PP spectra should be identical. This different response to the 800-nm pulse indicates that the ESA shoulder originates from a species other than the S_1 state. This species is denoted $S^{\ddagger}$ [49]. The second MPTAS experiment performed was the addition of a 530-nm pulse to the PP measuring scheme [49]. This pulse is resonant with both the stimulated emission of S_2 and the absorption of S_1; its effect on the observed PP kinetics depends on the exact timing (i.e. on the state of the molecule that it finds it in). Figure 9.17 illustrates the effect of the

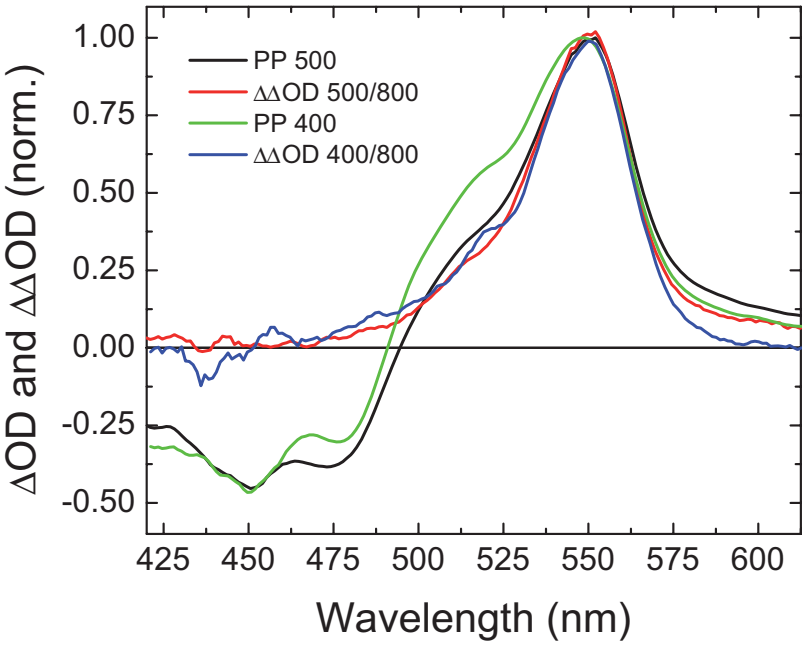

Fig. 9.16. Pump-probe spectra of β-carotene measured 3 ps after excitation at 400 nm (green line) and 500 nm (black thick line). The spectra have been normalized on the S_1 ESA maximum (550 nm). Blue and red lines show the double difference spectra (the difference between pump probe spectra in the presence and absence of the 800 nm repump pulse). The red line to a pump wavelength of 500 nm, the blue line - to a pump wavelength of 400 nm. The double difference spectra are also normalized at 550 nm.

530-nm pulse on the population of S_1: the S_1 signal is largely depleted upon interaction with the 530 nm pulse at 3 ps; the ensuing dynamics illustrates that population returns back to S_1 only partly. The complex dynamics is observed at 580 nm, where the ESA is due to vibrationally hot S_1 [72]. From the observed kinetics, it can be inferred that the back relaxation from the higher states involves the transient population of higher vibrational levels within S_1, before relaxing to the cool S_1 within 500 fs.

An action trace measurement was performed to investigate the changes induced on the 3-ps PP spectrum as the delay of the 530-nm pulse is varied (see Fig. 9.10C). Figure 9.18 shows the action traces measured at two wavelengths: 450 nm (GSB) and at 550 nm, (S_1 ESA peak). The effects differ significantly and two timescales can be separated. At 450 nm and early times (when the additional pulse is in resonance with the SE of S_2), the $\Delta\Delta OD$ signal exhibits a loss of GSB which results from the dumping of excited state population from the S_2 to the ground state. At 550 nm and early delays of the additional pulse, a similar effect is observed, because the S_1 population is also reduced

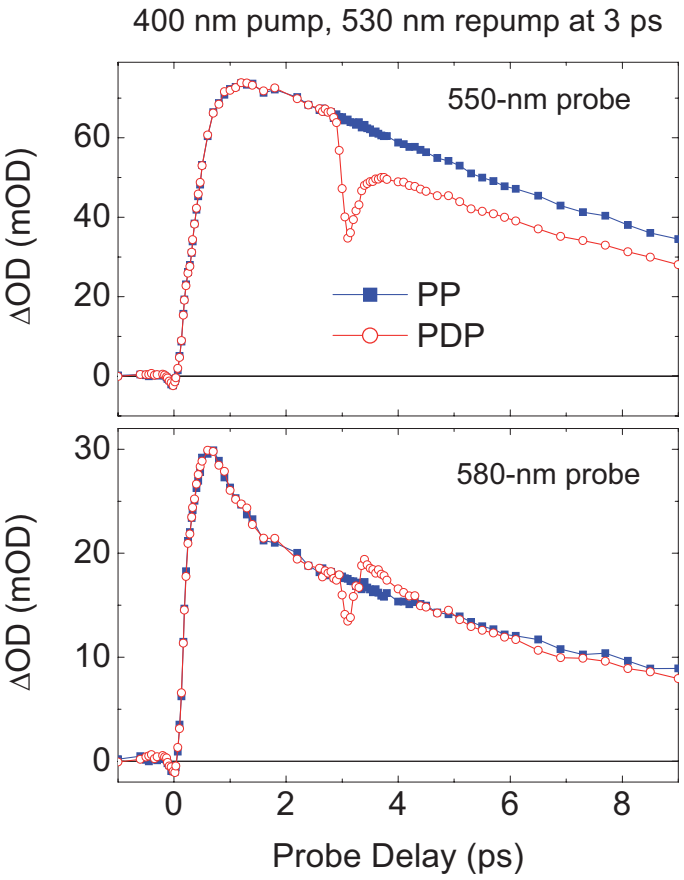

Fig. 9.17. The effect of a 530 nm pulse on the pump-probe kinetics of β-carotene. Excitation wavelength was 400 nm, the traces shown were probed at 550 nm (top) and 530 nm (bottom). Blue squares show unperturbed pump signals, red open circles depict the difference absorption signal in the presence of additional 530 nm pulse.

as a result of the S_2 dump. An additional, longer, timescale is also present in the 550-nm trace, describing the removal of population from the S_1 state by repumping its ESA at 530 nm.

Using global analysis, timescales and spectra that correspond to these two processes were estimated [49] (see Fig. 9.18 bottom panel). A fast, 300 fs, component which corresponds to the dumping of S_2 describes the full loss of the ESA band (also shown for comparison), i.e. due to both the S_1 and the $S^{\ddagger}$ bands, whereas the slow, 10 ps, component, describes the preferential loss of the S_1 ESA. The fact that $S^{\ddagger}$ is depleted after dumping S_2 shows it corresponds to an excited state which is formed via S_2, and which, as both 800 nm and 530 nm repump experiments illustrate, is separate from S_1.

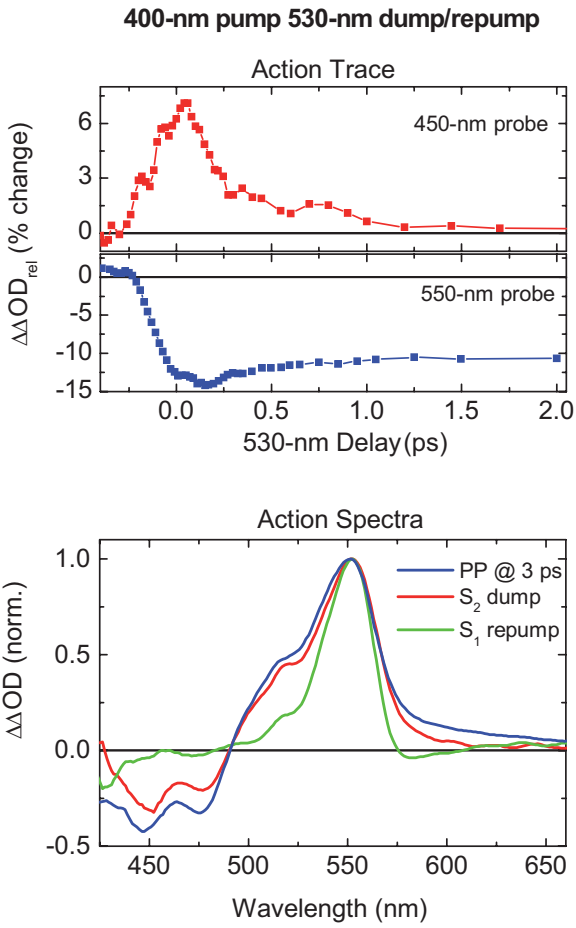

Fig. 9.18. Action traces (top) and spectra (bottom) measured for β-carotene with a 400 nm pump and 530 nm dump/repump pulse. The probe delay was 3 ps (see Figure 3C). In the top panel, the relative $\Delta\Delta OD$ signal is shown as a percentage of PP signal at two different probe wavelengths (indicated on the figure). The bottom panel contrasts the pump-probe spectrum measured at 3 ps probe delay (blue line), action spectrum of S_2 (solid line) and action spectrum of S_1 (green line).

The $S^{\ddagger}$ is not dissimilar from the S^* state, which was observed in several other carotenoids; however, unlike $S^{\ddagger}$, high-energy excitation is not required to create S^* and moreover its ESA is not as blue-shifted and broad as that of $S^{\ddagger}$ [73,76]. The nature and relationship of these states remains elusive. Calculations on polyenes [77] predict two electronic states, apart from S_1, under S_2, the $1B_u^-$ and the $3A_g^-$ states. However, in order to assign the observed $S^{\ddagger}$ (or the S^*) to either of them, determination of their 0-0 energy is required. It is

also unclear to what degree the spatial configuration of carotenoids influences their excited-state manifold; it has been proposed that the relaxation in the excited state manifold of β-carotene includes minor structural changes [72] and that in light-harvesting complexes, the protein-imposed configuration controls an additional deactivation channel [78]. Thus, it was concluded that these new states result from overcoming configurational barriers in the S_2 state when excited with additional excitation energy [49].

9.3.3.2 Excited state equilibrium between charge transfer state and S_1 in peridinin

Responding to the presence of only blue/green light underwater, photosynthetic marine organisms often rely on carotenoids rather than chlorophylls for light harvesting; the highest carotenoid/chlorophyll ratio (4:1) is found in the water-soluble peridinin chlorophyll protein (PCP) of the dinoflagellate *Amphidinium carterae* [79].

Peridinin is special among carotenoids because its carbonyl group induces a large dependence of its excited state manifold and dynamics on the solvent polarity and, in the case of protic solvents, also on the excitation wavelength [74, 79]. In polar solvents, a distinct SE band is observed in the near-IR, which is absent in nonpolar media [74]. This band has been attributed to an intramolecular charge transfer (ICT) state of peridinin. The exact relationship of the ICT state with the S_1 state, the only state observed in nonpolar solvents, has been debated, both in experimental [79,80] and theoretical [80,81] works, and is not elucidated yet: are they separate states or are they the same entity? This complex excited state structure makes peridinin a challenge that MPTAS techniques can help to address.

To investigate the complex excited state dynamics, a PDP experiment on peridinin in methanol was performed; the molecule was excited at 530 nm and an 800-nm pulse was then used to dump the near infrared SE of the ICT state [82]. Figure 9.19A shows the normalized PP spectra measured 1 ps and 10 ps after excitation. The region below 550 nm, which has been associated with the ESA of the S_1 state [79,80], is enhanced in the 10-ps spectrum. This implies that S_1 is populated on the timescale of a few picoseconds after the ICT state. Figure 9.19B contains the $\Delta\Delta OD$ traces measured in the PDP experiment with the dump pulse placed 3 ps after the pump pulse. Before the interaction of the dump pulse with the sample (probe delay less than 3 ps), the signal is zero - the dump pulse has not arrived yet and therefore the PP and PDP data are identical. The induced change appears upon the arrival of dump pulse and has a temporal profile that depends on the probe wavelength: the peak of the ICT ESA at 590 nm is lost instantaneously, whereas the loss at 535 nm (S_1 ESA) and 435 nm (GSB) shows slower, and more complex, dynamics. Figure 9.19C contrasts the $\Delta\Delta OD$ spectra to the PP spectra at two probe delays after the 3-ps dump. At a probe delay of 3.5 ps, the $\Delta\Delta OD$ spectrum does not have any amplitude in the S_1 region and indicates that the

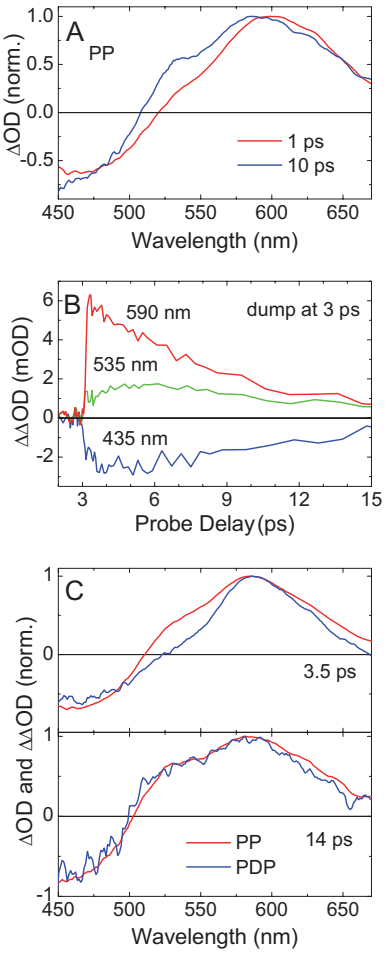

Fig. 9.19. Transient absorption measurements for peridinin in methanol after 530-nm excitation. *A*. pump-probe spectra measured at different probe delays; *B*. Pump-dump-probe $\Delta\Delta$OD kinetics with the 800-nm dump pulse placed at 3 ps; *C*. The $\Delta\Delta$OD spectra (blue lines) measured at probe delays of 3.5 ps and 14 ps contrasted to the respective pump-probe spectra (red lines).

dump pulse selectively depletes the ESA of the ICT-state; in contrast, the loss found at a probe delay of 14 ps is uniform across the complete ESA as the $\Delta\Delta OD$ spectrum overlaps with the PP spectrum. This leads to a conclusion that the S_1 state is separated from the ICT state: the dump does not affect it in the same instantaneous fashion. However, the fact, that after a certain time delay S_1 does exhibit a response, indicates that the S_1 and the ICT state are in equilibrium with each other.

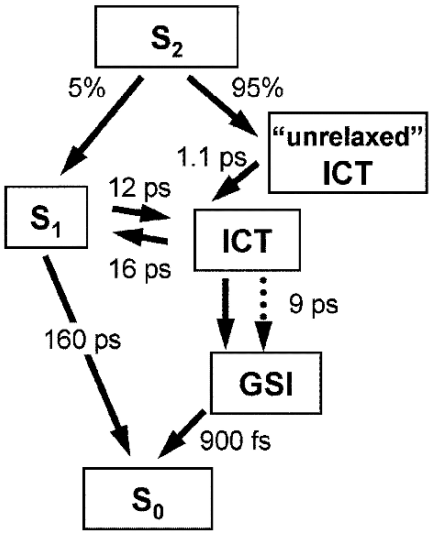

Fig. 9.20. Kinetic scheme used to model the excited states of peridinin [82]. GSI denotes the unequilibrated ground state that is produced by the relaxation (or dumping) of the ICT state.

The connectivity scheme shown in Fig. 9.20 was proposed, that allowed to explain the observed PP and PDP data on peridinin [82]. Upon excitation, population is transferred to the S_2 state, which then relaxes through two separate (branched) pathways, populating either the S_1 state or the ICT state. This relaxation involves an unrelaxed, 'hot' intermediate similar to other carotenoids [71, 72]. Both the natural and the dumped evolution of the ICT state populates an unequilibrated ground state, which in turn decays into the equilibrium ground state. The single trace that shows this most clearly is the 435 nm trace in Fig. 9.19B (blue): upon dumping, the bleach does not recover instantaneously, but ground state equilibration dynamics takes place. In addition to their own decay pathways, the populations of the S_1 and ICT states are in equilibrium with each other - another result that was deduced from MPTAS experiments.

9.3.4 Resolving the primary steps of photoactive yellow protein photocycle

The Photoactive Yellow Protein (PYP) is a small, 125 amino acid containing, water-soluble protein found in the bacterium *Halorhodospira halophila* and is responsible for triggering the negative phototaxis response of the organism to blue light [83–85]. PYP contains an intrinsic chromophore, paracoumaric acid, that is covalently bound to the protein backbone via a cysteine

residue [86–89]. Upon photoexcitation, this chromophore undergoes a trans-cis isomerization around its double bond [89–91] and initiates a complicated series of reversible reactions that extends over 15 decades in time extending from femtoseconds to seconds [92–95]. These isomerization-induced processes include chromophore protonation [92, 96], protein unfolding [93], hydrogen-bond disruption [97, 98], and their corresponding recovery reactions. Hence, PYP is an excellent system for studying the complex relationship between protein dynamics and chemical reaction dynamics and more specifically how Nature has tuned both to produce biological function. The properties and the photocycle of PYP have been extensively studied (see [99–101] for review), here we will mostly concentrate on the application of MPTAS to investigate the primary events occurring in PYP after the excitation.

Ultrafast PP transient spectra of wt-PYP, excited with ultrafast 395-nm excitation pulses, are shown in Fig. 9.21, spanning probing times from 180 fs to 4 ns [48]. The collected spectra and dynamics of the PYP system are similar to the data measured in other dispersed PP measurements on PYP [94,102–104]. All transient spectra show GSB, peaking at the maximum of the absorption spectrum (446 nm). The 180 fs and 2 ps spectrum also exhibit a broad negative band at 500 nm and a pronounced positive band at 370 nm, which are ascribed to the SE and the ESA band, respectively. In contrast, the 35 ps, 500 ps and 4 ns spectra no longer exhibit clear SE bands, but instead show positive product state absorption bands peaking at 500 nm and 480 nm, respectively, which are ascribed to the product state absorptions of the initial red-shifted intermediates in the PYP photocycle: I_0 and pR [99, 100]. The 35 ps, 500 ps and 4 ns PP spectra also exhibit a noticeable positive sharply peaked band at 360 nm that has not been previously ascribed to either the I_0 or the pR product state band. Since the ultrafast fluorescence signals on PYP show that no appreciable excited state population remains at this time [105–107], this sharply featured band is not ascribed to the similar UV ESA band observed in the 180 fs and 2 ps spectra. Furthermore, a weak broad absorption is observed in the 4 ns spectrum, which extends beyond 550 nm. Excitation power-dependence of these bands along with the MPTAS (PDP) measurements allowed to attribute these bands to a photoionization of the PYP chromophore, resulting in hydrated electron responsible for the broad induced absorption band at wavelengths longer than 550 nm, and the radical of the chromophore, featuring the sharp induced absorption band around 360 nm [48].

From the spectra shown in Fig. 9.21, it is obvious that the pump-probe spectrum is composed out of largely overlapping bands (both spectrally and temporally) due to different initial intermediates in the PYP photocycle. Getting a picture of how precisely the initial steps of PYP photocycle are organized is impossible using pump-probe and fluorescence upconversion data alone. For example, the near complete overlap of the SE band with the absorption of the first photoproduct, I_0, precludes directly correlating the quenching timescales of the excited state with the timescale of photocycle initiation [94, 104, 108]. Because of this ambiguity, different kinetic schemes

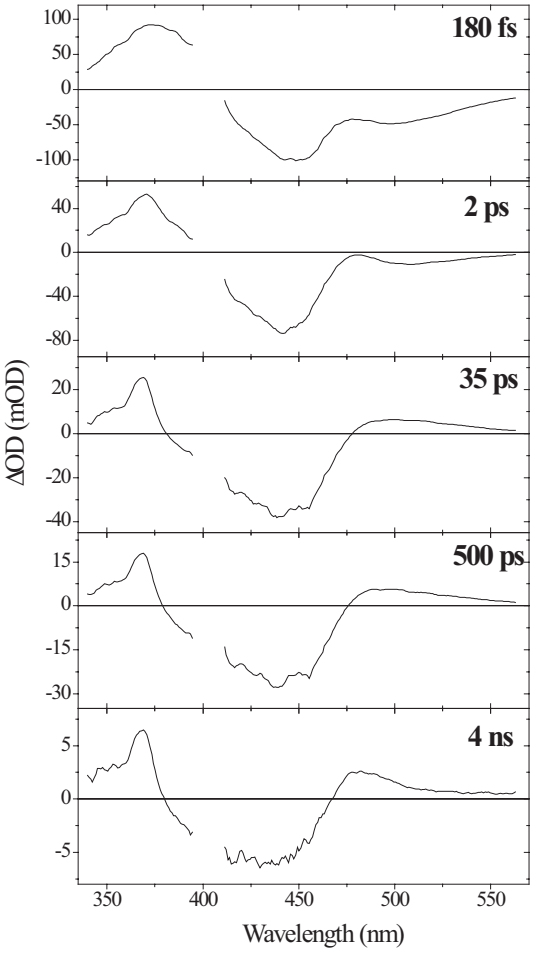

Fig. 9.21. Representative dispersion corrected transient PP spectra. The region around the pump excitation wavelength (395 nm) is corrupted due to scatter from the pump pulse.

have been proposed for modeling the initial dynamics of the PYP photocycle [102,104]. MPTAS was applied to get a better understanding of the initial dynamics of PYP [48].

Representative kinetic traces from two PDP data sets dumped at 500 fs (green circles) and 2 ps (solid blue circles) are shown in Fig. 9.22, overlapping the PP signals (red triangles). The dump pulse shifts part of the population from the excited state to the ground state, which is observed as a loss of SE (550 nm) and ESA (375 nm) with a concomitant recovery in the bleach region

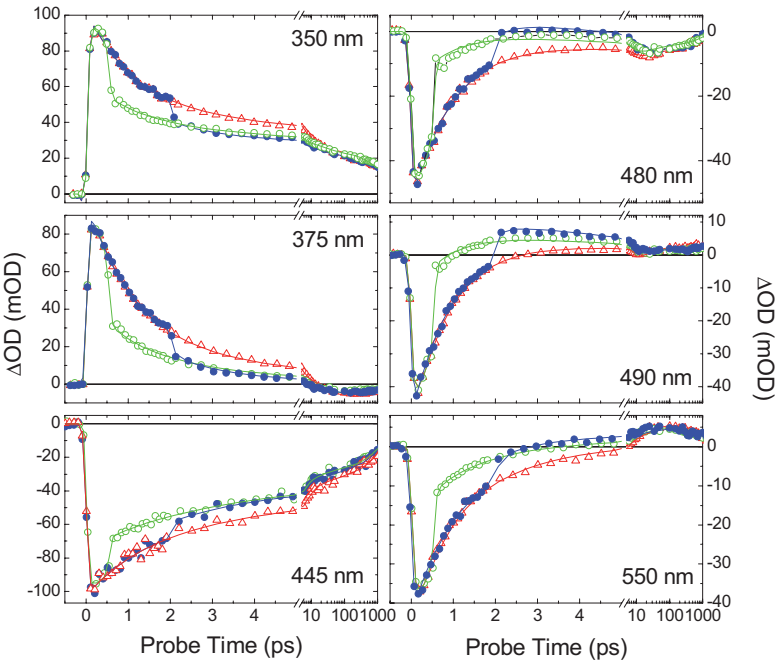

Fig. 9.22. Selected PP (red triangles) and PDP traces dumped at 500 fs (green circles) and 2 ps (blue circles). Symbols are the experimental data and the solid lines are the results of the global fits to these data. Note that the time axis is linear up to 5 ps, and then logarithmic to 1 ns.

(445 nm). However, the relative magnitude of the GSB recovery at 445 nm (∼25%) is not comparable with the depletion of the SE and ESA (∼50%), suggesting the involvement of a third intermediate state that temporarily stores ground-state population before refilling the bleach on a longer timescale. This ground state intermediate (GSI) is more clearly observed as an increase in the dump-induced absorption in the 480 nm and 490 nm traces, where a local maximum in both the PP and the PDP signals is observed. The structural basis of this intermediate state is not known; it may originate from a competing structural rearrangement motion (e.g. rotation about one of the sigma bonds, instead of the double bond of the chromophore) or from a local minimum in the ground state potential energy along the isomerization coordinate. The smaller dump effect in the 350-nm trace is indicative of the insensitivity of the overlapping radical contribution to the dump pulse; this observation is useful for characterizing photoionization properties. Such characterization was performed by measuring the action trace with the probe pulse placed at 500 ps after the excitation and scanning the dump pulse. This action trace is shown in Fig. 9.23, which shows the dump effect as a function of dump delay on the GSB (red triangles), I_0 induced absorption (green diamonds),

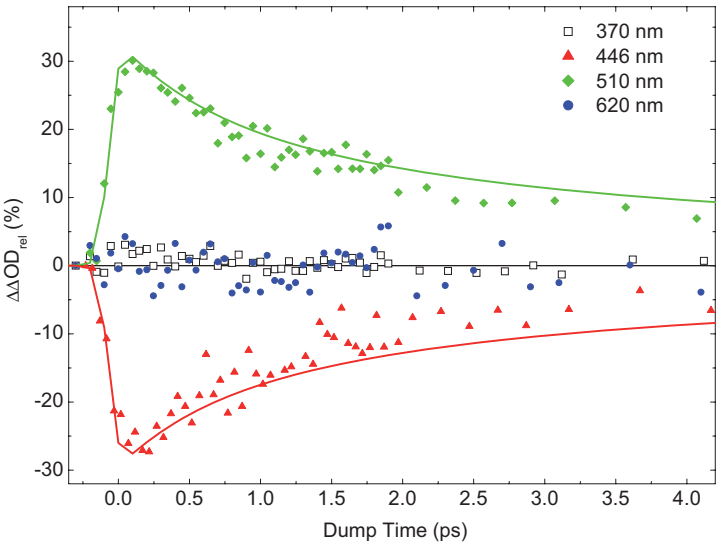

Fig. 9.23. Action trace of PYP, measured with probe time at 500 ps. Plotted is the $\Delta\Delta OD_{rel}$ signal (PDP-PP)/PP *vs.* the dump time. The red triangles are the dump-induced depletion of the bleach (446 nm) and the green diamonds are the induced-depletion of the I_0 photoproduct absorption (510 nm). The black squares and blue circles are the depletion of the radical (370 nm) and the ejected electron (620 nm) respectively. The amplitude of the PP signals were 13 mOD (radical), 30 mOD (bleach), 12 mOD (I_0) and 4 mOD (electron). Overlapping the bleach and I_0 signals is the fitted excited state population resulting from global analysis.

combined ESA and radical band (black squares) and hydrated electron band (blue circles). As expected for photoionization, which is a near-instantaneous process, the radical and electron bands in 500 ps pump-probe spectrum remain completely unaffected by the dump pulse, regardless of its timing. The action traces measured in the spectral regions of GSB and I_0 induced absorption allow to monitor the efficiency of entering PYP photocycle as a function of time [48]. By comparing them to excited state population (solid lines in Fig. 9.23), which can be estimated from the intensity of SE or ESA, one can see, that in the early times, the probability of producing an I_0 intermediate is surprisingly much higher.

On the basis of these PDP data and the PP data two self-consistent kinetic models were constructed to describe the observed dynamics (Fig. 9.24) [48]. Both the homogeneous (Fig. 9.24B) and the inhomogeneous (Fig. 9.24A) models describe the observed PDP and PP dynamics as an evolution between discrete interconnected transient states that are separated into four categories: i) excited-state dynamics, ii) ground-state dynamics, iii) photocycle dynamics and iv) an ionization channel. Whilst both models produce similar quality fits to the measured PDP data, their respective interpretations differ. The kinetic

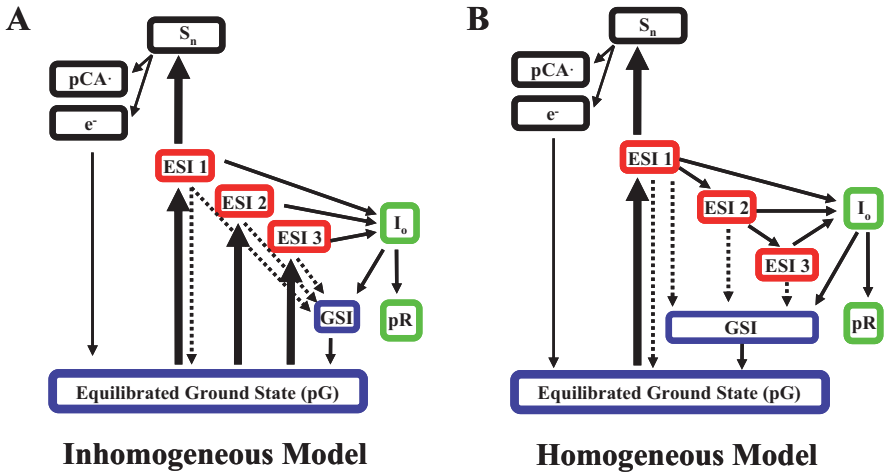

Fig. 9.24. Connectivity schemes compatible with the data and used in the global analysis for the PDP: A) inhomogeneous model and B) homogeneous model. Dynamical states are separated into four classes: excited state (red), ground state (blue), photocycle products (green) and two-photon ionization dynamics (black). ESI1, ESI2, and ESI3 refer to the excited state lifetimes τ_1, τ_2 and τ_3 respectively. pG is the equilibrated ground state species, and GSI is the ground state intermediate. Thick solid arrows represent the initial excitation process from the laser pulse and thin solid arrows dynamics represent the natural PP population dynamics. The dashed arrows represent the population transfer dynamics that may be enhanced with the dump pulse. S_n is a higher lying electronic state and $pCA^{\bullet}$ is *p*-coumaric acid PYP chromophore radical after ionization.

models differ primarily in the connectivity scheme for the excited-state evolution, and with respect to which state(s) is (are) initially excited by the applied laser pulse (thick black lines). Whilst the inhomogeneous model ascribes the multiexponential excited-state behavior to a superposition of multiple subpopulations with differing decay times, the homogeneous model ascribes the multiexponential decay to evolution along the excited-state potential energy surface.

The PDP technique probes the reaction yield of each ESI by dumping the ESI at different times and then probing the magnitude of the change of the I_0 photoproduct absorption. The PDP data favor the inhomogeneous over the homogeneous model since each ESI does not have the same yield in initiating the PYP photocycle. This observation, in combination with the global analysis of the kinetic trace PDP signals, supports the observation that ESI1 has the highest yield ($\sim$40%) followed by ESI2 (20%), whereas ESI3 has a near negligible yield ($\sim$1%) in initiating the photocycle. A homogenous model would require that the excited state population would have a time-dependent yield and evolve across a complex potential energy surface with quenching

pathway(s) that compete with photocycle generation. The inhomogeneous model, in contrast, is simpler to interpret.

In summary, photoinduced dynamics of biological systems presents a significant challenge to laser spectroscopists. Besides the problems related to the nature of the samples (biological material is 'soft', difficult to obtain in large quantities, and often unstable under laser light illumination), the dynamic properties of biological molecules are inherently complex. Photoactive proteins and pigments use the light in a variety of ways, their principle reaction pathways occur in parallel with the cul-de-sac events and the spectral features of different photoreaction intermediates co-exist in time and spectrally overlap with reaction 'byproducts'. These properties often prevent unambiguous interpretations of ultrafast spectroscopic data obtained in 'traditional' ways, such as pump-probe and fluorescence up-conversion. Multi-pulse transient absorption spectroscopies, together with the state-of-the-art achievements in laser technology, open up the possibilities of bringing the understanding the light-induced biological reactions to a qualitatively new level.

9.4 Laser pulse control of excitation energy dynamics in biological chromophore complexes

B. Brüggemann and V. May

The investigation of electronic excitations in chromophore complexes known as Frenkel excitons represents one major application of femtosecond spectroscopy (for recent introductions into this field see [109, 110]). Of particular interest have been studies of light harvesting antennae belonging to the photosynthetic apparatus of bacteria or higher plants (cf. the overview in [111,112]). Although femtosecond laser pulse control techniques are widely used meanwhile (see [113,114] and Chapter 2 for an up to date overview), there only exist a single example where these techniques have been applied to chromophore complexes. Reference [115] describes such an application to discriminate between internal conversion and excitation energy transfer taking place among a carotenoid and bacteriochlorophyll (BChl) molecule in the light harvesting antenna LH2 of purple bacteria.

This concept of guiding excitation energy into one of two particular transfer channels will be put here into a more general frame. In the following, a theoretical analysis is presented of laser pulse controlled excitation energy motion and localization in systems of strongly coupled chromophores like the FMO–complex or the PS1 (for both antenna systems see [111]). While general aspects have been already discussed in [116–118] emphasis is put here on polarization control [119] (see also [120]). This is of particular interest since recent pulse shaping technology allows for a simultaneous and inde-

pendent manipulation of the two different polarization directions of the laser beam [121].

When studying Frenkel excitons one is faced with spatially delocalized excited states with the basic electronic excitations, however, completely localized at the individual chromophores of the complex. The respective state vector for such a localized excitation will be denoted as $|\phi_m\rangle$ with the index m indicating the excited chromophore. The strong coupling among different chromophores results in the formation of delocalized (single)–exciton states $|\alpha_1\rangle = \sum_m C(\alpha_1; m)\, |\phi_m\rangle$ with energy $\hbar\Omega_{\alpha_1}$. This energy is much larger than the thermal energy (at room temperature conditions) and if the coupling to vibrational coordinates remains weak, as it is often the case, excitation energy transfer may proceed coherently up to some 100 fs.

The particular control task which will be discussed in the following aims at an excitation energy localization at a single chromophore at a definite time. The localization has to be achieved against the tendency to form delocalized states. It requires the photo–induced formation of an excitonic wave packet, i.e. the time–dependent superposition $\sum_{\alpha_1} A_{\alpha_1}(t)|\alpha_1\rangle$ of the various exciton states. This has to be done in such a way that at the final time t_f of the control task the superposition corresponds to excitation energy localization at a particular chromophore m, i.e. $\sum_{\alpha_1} A_{\alpha_1}(t = t_f)|\alpha_1\rangle = |\phi_m\rangle$. Of course, it would be of interest to study a situation where the time t_f to reach the target state is replaced by a time–interval around t_f as it would be necessarily the case in an experiment which proofs the suggested excitation energy localization [122–124]. If the detection interval, however, amounts to clearly less than 100 fs it would not change the outcome so much, since the exciton dynamics in the considered systems is slow on a sub–100 fs time–scale.

To form the superposition state $\sum_{\alpha_1} A_{\alpha_1}(t)|\alpha_1\rangle$ all exciton states in a control task have to be addressed, therefore the oscillator strength should be distributed over all exciton states $|\alpha_1\rangle$ which excludes the use of highly symmetric complexes for such studies. For an appropriate non–regular structure, however, different transition dipole moments $\mathbf{d}_{\alpha_1}$ may also posses different spatial orientations. This would favor the use of polarization shaped control fields. The spatial orientation of $\mathbf{E}(t)$ (perpendicular to the propagation direction) would increase the flexibility for putting the various coupling expressions $\mathbf{d}_{\alpha_1}\mathbf{E}(t)$ in the right order of magnitude at the right time interval to achieve the proper wave packet formation. (Of course, a random spatial orientation of the complexes has to be included into these considerations.)

The description of excitation energy localization discussed so far has to be generalized to the inclusion of exciton relaxation and dephasing originated by the presence of exciton–vibrational coupling. This requires an approach based on open system dynamics techniques, i.e. by introducing the (reduced) exciton density matrix. Moreover, one has to account for structural and energetic disorder. Such a combination of density matrix propagation, polarization shaping, and disorder to solve the control task using the Optimal Control Theory (OCT) is new and will be explained in detail in the following sections.

First, in the subsequent section, the exciton model and the density matrix description are introduced. Afterwards, a specific implementation of the OCT is shortly explained. Some selected results are presented in the last section.

9.4.1 Excitons in biological chromophore complexes

When studying chromophore complexes by ultrafast and intense laser pulses higher excited states of single molecules as well as of the whole complex have to be taken into account. It results the multiexciton scheme which found various applications in different non–biological complexes as well as photosynthetic antenna systems [111,112]. The respective basic model applied in the following is explained in Fig. 9.25.

Based on this model one may introduce singly excited states $|\phi_m\rangle$ of the complex as well as doubly excited states $|\phi_{mn}\rangle$, corresponding to a double excitation of a single molecule ($m = n$) or the simultaneous single excitation of two different chromophores ($m \neq n$). Their superposition may result in single–exciton states $|\alpha_1\rangle = \sum_m C(\alpha_1; m)|\phi_m\rangle$, with quantum numbers α_1

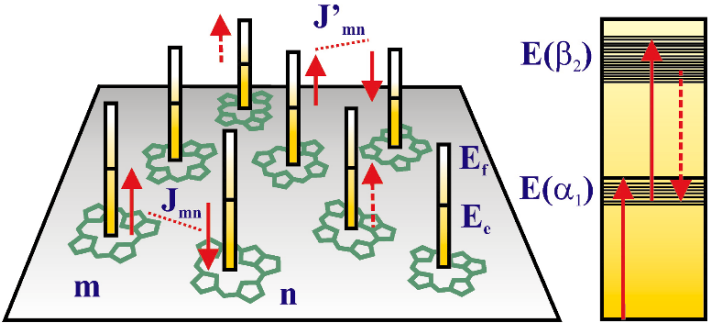

Fig. 9.25. Excitation energy transfer in a chromophore complex (left part) with the chromophores (tetrapyrrole type molecules) arranged to a planar complex and described by a three–level model. Beside the electronic ground–state energy E_g (not shown) every chromophore is characterized by a first excited state with energy E_e and a higher excited state with energy E_f. Excitation energy transfer is possible via de–excitation of chromophore n (from E_e to E_g, shown by vertical arrow) and excitation of chromophore m (from E_g to E_e). Both processes are caused by the Coulombic inter–chromophore coupling J_{mn} (broken line). Transfer of the double excitation of a single chromophore is realized by J'_{mn} (double excitation via a fusion of two single excitations is also possible). A single chromophore may be excited by photon absorption (vertical dotted arrows). The right part shows the manifold of single and two–exciton levels with energies $E(\alpha_1) \equiv \hbar\Omega_{\alpha_1}$ as well as $E(\alpha_2) \equiv \hbar\Omega_{\alpha_2}$ and resulting from a superposition of singly and doubly excited states of the complex, respectively (full arrows: optical excitation, broken arrow: radiationless decay of two–exciton state via exciton–exciton annihilation).

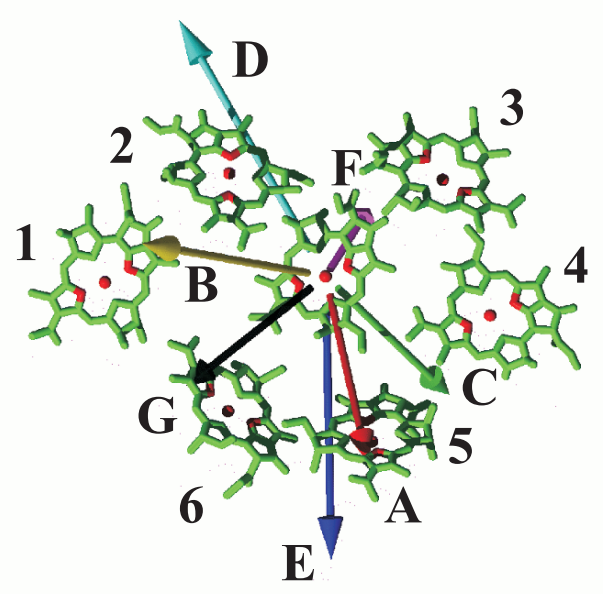

Fig. 9.26. Spatial arrangement of the seven BChls in the monomeric FMO complex of *Prosthecochloris aestuarii* (without protein matrix, the used counting scheme labels BChl 1 to 6, BChl 7 is positioned in the center) [125]. Atoms in line of the respective Q_y dipole moments are marked (all parameters used in the calculations can be found in [116, 126]). The different arrows display the magnitude and spatial orientation of the exciton transition dipole moments $\mathbf{d}_{\alpha_1}$ (to distinguish the labeling from those of the BChl, capital letters A to G have been used for $\alpha_1 = 1$ to 7). Note, that the exciton levels 3 and 5 mainly contribute when BChl 7 should be exclusively excited [116].

as well as in two–exciton states $|\alpha_2\rangle = \sum_{m,n} C(\alpha_2; m, n)|\phi_{mn}\rangle$, with quantum numbers α_2. Using these states and accounting for all inter–chromophore Coulombic interactions (often used in the form of a dipole–dipole coupling, cf., for example, [110]) the complete electronic part of the overall Hamiltonian can be diagonalized (with the vibrational coordinates fixed at their ground–state equilibrium configuration). Both types of states together with the ground–state $|\alpha_0\rangle \equiv |\phi_0\rangle$ define the multiexciton part $H_{\rm mx}$ of the overall Hamiltonian $H_{\rm mx} = \sum_N \sum_{\alpha_N} \hbar\Omega_{\alpha_N} \, |\alpha_N\rangle\langle\alpha_N|$. Here, $N = 0, 1, 2$ counts the so–called exciton manifolds and the $\hbar\Omega_{\alpha_N}$ define the respective spectrum.

Besides $H_{\rm mx}$ the chromophore complex Hamiltonian

$$H_{\rm CC}(t) = H_{\rm mx} + H_{\rm mx-vib} + H_{\rm vib} + H_{\rm field}(t)$$

includes the coupling to intra- and inter-molecular vibrations ($H_{\rm mx-vib}$) and the coupling to external laser fields ($H_{\rm field}(t)$). Neglecting inter–manifold coupling, the multiexciton–vibrational coupling is given by:

$$H_{\mathrm{mx-vib}} = \sum_{N} \sum_{\alpha_N, \beta_N} H^{(\mathrm{mx-vib})}_{\alpha_N \beta_N} |\alpha_N\rangle\langle\beta_N|$$

with the matrix elements expanded with respect to the vibrational coordinates q_ξ, i.e. $H^{(\mathrm{mx-vib})}_{\alpha_N \beta_N} = \sum_\xi \hbar\omega_\xi g_{\alpha_N \beta_N}(\xi) q_\xi$. This represents the most basic expression. Its introduction can be understood as the result of a normal–mode description of all vibrations (with parabolic PES). Accordingly, the Hamiltonian H_{vib} is that of decoupled harmonic oscillators. Often, a vibrational modulation of the inter–chromophore coupling is neglected. More involved formulas as well as the derivation of the matrix elements $g_{\alpha_N \beta_N}(\xi)$ can be found in, e.g., [110,112,127,128] ([127] puts also emphasis on internal conversion processes being responsible for exciton–exciton annihilation, see below). The Hamiltonian $H_{\mathrm{field}}(t)$ describing the coupling to the radiation field $\mathbf{E}(t)$ is written in the standard form $-\hat{\mu}\mathbf{E}(t)$ where the chromophore complex dipole operator $\hat{\mu}$ includes ground–state single–exciton transitions with dipole matrix elements $\mathbf{d}_{\alpha_1}$ and transitions from the single into the two–exciton states with dipole matrix elements $\mathbf{d}_{\alpha_2 \beta_1}$.

In order to specify the multiexciton approach to light harvesting antenna complexes a three–level model (see Fig. 9.25) is introduced for every Chlorophyll (Chl) or Bacteriochlorophyll (BChl) molecule. The so–called Q_y–state of tetrapyrroles is taken as the first excited state. The higher excited state has to be considered as a representative of the multitude of higher excited electron–vibrational states (it has to be introduced to allow for intra–chromophore excitations in the same energetic range where the energy of two singly excited states at different chromophores is positioned). Besides their energy level structure every chromophore has to be characterized by transition dipole moments. If data on the electronic inter–chromophore couplings are available they can be used to define the respective expressions in the Hamiltonian. Otherwise one applies the dipole–dipole approximation (necessary in any case if the higher excited states are concerned). Finally, the spectral densities resulting from the coupling to the multitude of vibrational coordinates (see below) are fixed by fitting optical absorption or luminescence. Independent calculations are not available so far (cf. also [111,112]).

To describe the light–driven exciton dynamics in the presence of relaxation and dephasing the multiexciton density matrix is introduced

$$\rho(\alpha_M, \beta_N; t) = \langle \alpha_M | \hat{\rho}(t) | \beta_N \rangle \ , \tag{9.3}$$

where $\hat{\rho}(t)$ denotes the related reduced density operator. The diagonal elements $\rho(\alpha_M, \alpha_M; t)$ define the exciton level populations and the off-diagonal ones the different coherences, which may refer to the same manifold or to different manifolds. There are different ways to compute $\rho(\alpha_M, \beta_N; t)$. Here, a description is chosen based on the following Markovian quantum master equation

$$\frac{\partial}{\partial t}\hat{\rho}(t) = -\frac{i}{\hbar}[H_{\mathrm{mx}} + H_{\mathrm{field}}(t), \hat{\rho}(t)] - \mathcal{R}_{\mathrm{mx-vib}}\hat{\rho}(t) \ . \tag{9.4}$$

The multiexciton Hamiltonian $H_{\rm mx}$ together with the coupling to the external laser pulses $H_{\rm field}(t)$ determine the reversible part of the quantum master equation, whereas energy relaxation and dephasing are accounted for by the superoperator $\mathcal{R}_{\rm mx-vib}$. The latter is assumed to take the following form

$$\mathcal{R}_{\rm mx-vib}\,\hat{\rho}(t) = \sum_{N=1,2}\sum_{\alpha_N,\beta_N} k^{\rm (mx-vib)}_{\alpha_N\to\beta_N} \left\{\frac{1}{2}\big[|\alpha_N\rangle\langle\alpha_N|,\hat{\rho}(t)\big]_+ - |\beta_N\rangle\langle\alpha_N|\hat{\rho}(t)|\alpha_N\rangle\langle\beta_N|\right\}. \tag{9.5}$$

The transition rates $k^{\rm (mx-vib)}_{\alpha_N\to\beta_N}$ are mainly determined by the spectral densities $\mathcal{J}_{\alpha_N\beta_N,\beta_N\alpha_N}$ taken at the transition frequencies $\Omega_{\beta_N} - \Omega_{\alpha_N}$. The single–exciton spectral density, for example, is given by the expression $\mathcal{J}_{\alpha_1\beta_1,\beta_1\alpha_1}(\omega) = \sum_m \mid C(\alpha_1;m)C(\beta_1;m)\mid^2 J_e(\omega)$, including chromophore local spectral functions $J_e(\omega)$ (a more involved description can be found in [112]). Notice that the spectral densities account for delocalized multiexciton states since they are defined in using the related expansion coefficients. Often it becomes also necessary to account for exciton–exciton annihilation as the dominant non–radiative two–exciton decay channel. For respective considerations see [111, 112, 127, 128].

The sequence of approximations necessary to arrive at (9.4) and (9.5) is well documented in the literature (for a recent overview see [129, 130]). One has to carry out a second order perturbation theory with respect to the exciton–vibrational coupling. The correlation time of the vibrational equilibrium correlation function should be short enough to allow for a neglect of non–Markovian contributions, the laser pulse field strength has to be small enough to exclude contributions in $\mathcal{R}_{\rm mx-vib}$ and, finally, the spectra of single and two–exciton states have to be anharmonic to neglect the coupling between diagonal and off–diagonal density matrix elements.

9.4.2 Theory of femtosecond laser pulse control

Theoretical simulations of laser pulse control experiments are mainly carried out in the framework of the Optimal Control Theory (OCT) [110,131,132] and Chapter 2. It allows one to compute the laser pulse (the control field) $\mathbf{E}$ which optimizes the observable $\mathcal{O}$ measured in the particular control experiment (taking place in the time interval from t_0 up to t_f and under the constraint of a finite laser pulse intensity). Therefore, one searches for an $\mathbf{E}(t)$ which leads to an extremum of the overall control functional:

$$J[\mathbf{E}] = \mathcal{O}[\mathbf{E}] - \lambda\big(\frac{1}{2}\int_{t_0}^{t_f} dt\ \mathbf{E}^2(t) - I_0\big). \tag{9.6}$$

The second term represents the constraint to ensure finite control field intensity fixed by the value I_0, and the quantity λ is a Lagrange multiplier. (Often

one avoids to adapt the field to the predetermined intensity but fixes λ by a reasonable value and determines the related I_0 after the control task has been solved.) The field $\mathbf{E}$ resulting in an extremum of $\mathcal{O}[\mathbf{E}]$ will be called the *optimal* field. This scheme has been widely applied to the description of pure state molecular dynamics. Generalizations to open molecular system have been also worked out, but found less applications (cf. [133–136]).

A rather general expression for $\mathcal{O}$ defined via a trace expression with respect to the multiexciton levels and the multiexciton density operator is given by

$$\mathcal{O}[\mathbf{E}] = \int_{t_0}^{\infty} dt_f \int dp \, \mathrm{tr}_{\mathrm{mx}}\{\hat{O}(t_f;p)\hat{\rho}(t_f;p)\} \, . \tag{9.7}$$

It accounts for a distribution of the final time t_f where the observable (represented by the operator $\hat{O}(t_f;p)$) has to be maximized (for example, optimization of the probe–pulse signal in a pump–probe scheme [122–124]). p is a parameter or set of parameters which should refer to a particular property changing among the individual molecules. Therefore, $\mathcal{O}[\mathbf{E}]$ not only accounts for a distribution of the operator $\hat{O}$ in time but also in the space of the parameters p. Then, $\mathcal{O}$ is ready to describe, for example, inhomogeneous broadening present in the considered molecular system. In this case p counts all molecules in the sample, where the properties of the single molecules, for example, their excitation spectrum change from molecule to molecule.

The determination of the optimal control field is achieved by searching for the extremum of J, i.e. the solution of $\delta J/\delta \mathbf{E} = 0$. The solution of the resulting it gives the temporal behavior of the optimal pulse (self–consistency condition for the optimal field)

$$\mathbf{E}(t) = \frac{i}{\hbar\lambda} \int dp \int_{t}^{\infty} dt_f \, \mathrm{tr}_{\mathrm{S}}\{\hat{O}(t_f;p)\mathcal{U}(t_f,t;p;\mathbf{E})[\hat{\mu},\hat{\rho}(t;p)]\} \, . \tag{9.8}$$

The field at time t is determined by the commutator of the dipole operator with the density operator taken also at time t, but further propagated up to t_f. The latter procedure is indicated by the action of the time–propagation superoperator $\mathcal{U}(t_f,t;\mathbf{E})$ (depending on the parameter set p and at the presence of the field $\mathbf{E}$). Notice also the integration with respect to t_f which originates from the time distribution of $\hat{O}$. To solve (9.8) one rearranges the trace expression in order to replace $\int_t^{\infty} dt_f \, \hat{O}(t_f;p)\mathcal{U}(t_f,t;p;\mathbf{E})$ by the auxiliary density operators $\hat{\theta}(t;p)$ propagated backwards in time (see also [134, 135]). The respective equation of motion is different from that with $\mathcal{R}_{\mathrm{mx-vib}}$. A changed expression appears (cf. [116]) which enables a stable propagation backward in time (in the presence of dissipation and of the field). The control task is solved by a combined iterative forward and backward propagation [133] (see also [134, 135]).

If energetic disorder is considered a discrete set of different $\hat{\rho}(t;p)$ and $\hat{\theta}(t;p)$ appears with p counting the different complexes in the ensemble. Accounting also for polarization shaping (**E** consists of an x– and y–component perpendicular to the propagation direction), (9.8) reads ($j = x, y$):

$$E_j(t) = \frac{1}{N_{\rm CC}} \sum_p \frac{i}{\hbar\lambda} {\rm tr}_{\rm mx}\{\hat{\theta}(t;p)[\hat{\mu}_{pj}, \hat{\rho}(t;p)]\} \; . \tag{9.9}$$

Here, $\hat{\mu}_{pj}$ denotes the x– or y–component of the dipole operator and $N_{\rm CC}$ is the number of different chromophore complexes considered in the disordered ensemble. Now, the optimal pulse $\mathbf{E}(t)$ represents a compromise with respect to the driven dynamics in the individual chromophore complexes of the disordered ensemble. In order to calculate $\mathbf{E}(t)$ one has to solve simultaneously the coupled equations of motion of the various $\hat{\rho}(t;p)$ and $\hat{\theta}(t;p)$.

9.4.3 Controlling excitonic wave packet motion in the FMO complex

The multiexciton density matrix theory in combination with OCT has been used to study fs laser pulse induced excitation energy localization in the PS1 [118] and the FMO complex [116, 119]. Here, emphasis is put on the latter example. Focusing on energy localization at a particular time t_f, the operator $\hat{O}$ introduced in (9.7) which characterizes the target of the control task is given by the projector $|\phi_{m_{\rm tar}}\rangle\langle\phi_{m_{\rm tar}}|$ times $\delta(t_f - \tau_f)$. Then, $\mathcal{O}[\mathbf{E}]$ of identified with the population of the target state $P_{\rm tar}$ at $t = \tau_f$ and can be calculated from the single–exciton density matrix according to

$$P_{\rm tar}(\tau_f) = \frac{1}{N_{\rm CC}} \sum_p \sum_{\alpha_1,\beta_1} C_p(\alpha_1; m_{\rm tar}) C_p^*(\beta_1; m_{\rm tar}) \rho_p(\alpha_1, \beta_1, \tau_f; p) \; . \tag{9.10}$$

Fig. 9.27 displays respective results for excitation energy localization at chromophore 7 of the monomeric FMO–complex (cf. Fig 9.26), but in the absence of two–exciton states and disorder. Most efficient localization is achieved for a control pulse length of around 600 fs. As has to be expected an increase in temperature acts counterproductive. The effect of transitions among the single and two–exciton manifold is demonstrated in Fig. 9.28. It results in a reduction of $P_{\rm tar}(\tau_f)$ from a value above 0.6 to a value somewhat below 0.4. To correctly rate this value one has to notice that the probability to stay in the chromophore complex ground–state is larger than 0.4. Therefore, it is advisable to consider the renormalized target state population $P_{\rm tar}(\tau_f)/P_0(\tau_f)$ which amounts to a value of about 0.6 ($P_0(\tau_f)$ is the ground–state population).

This justifies in part to neglect the two–exciton states when considering the influence of disorder (note also that an iteration of the OCT equations combined with an ensemble averaging now refers to less than 60 density matrix

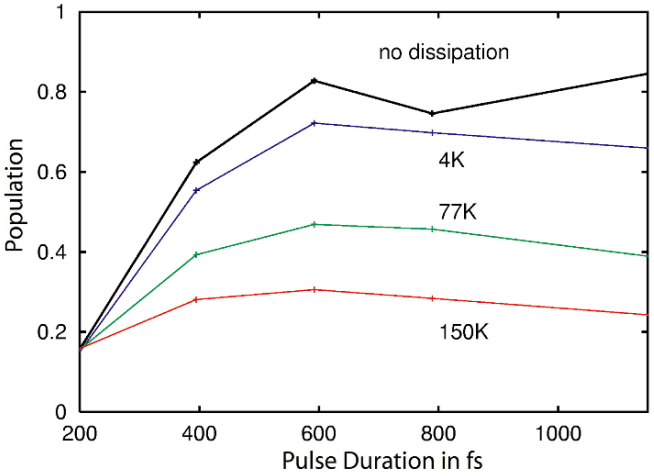

Fig. 9.27. Excitation energy localization in the FMO complex demonstrated by the population $P_{\rm tar}$, (9.10) of the single BChl Q_y–state $m_{\rm tar} = 7$ (cf. Fig. 9.25) at t_f. The population is drawn versus the pulse duration $t_f - t_0$ as well as in the absence of dissipation and for different temperatures. All data have been obtained in neglecting two–exciton states as well as disorder and after up to 50 iterations of the coupled density matrix equations for forward and backward propagation.

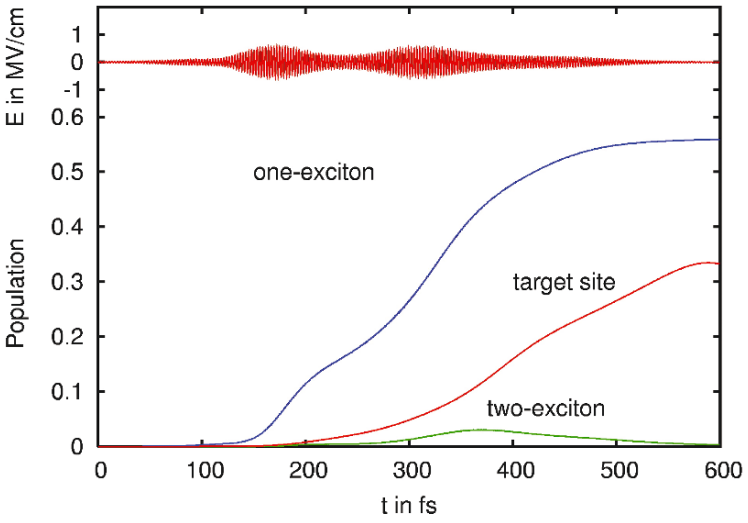

Fig. 9.28. Temporal evolution of excitation energy localization in the FMO complex, including transitions into the two–exciton manifold and a decay via exciton–exciton annihilation (target site $m_{\rm tar} = 7$, pulse duration $\tau_f - t_0 = 600$ fs, T = 4 K, neglect of disorder) Upper part: time–dependence of the control field, lower panel: overall single– and two–exciton state population as well as the target site population.

equations compared to about 1000 for the inclusion of two–exciton states). In any case the presence of disorder further decreases the control yield as shown in Fig. 9.29 (upper panel). Fortunately, this inefficiency can be compensated when changing to laser pulse control including polarization shaping. The possibility of an independent control of both polarizations of the field increases the control yield considerably (cf. the lower panel of Fig. 9.29). As demonstrated also in Fig. 9.29 the time interval where the two components (x– and y–component) of the field are non–zero becomes longer compared to the control with a linearly polarized field (the different sub pulses of the two components act out of phase indicating strong elliptic polarization of the control field).

9.5 Light induced singlet oxygen generation

I. Corral, L. González, A. Lauer, and K. Heyne

During the last decade drugs with endoperoxide groups have become more and more important. They are synthesized as antimalarial drugs [137, 138] or as photosensitizers for cancer treatment in photodynamic therapy (PDT) [139].

Malaria, along with tuberculosis and the human immunodeficiency virus (HIV), form a disease triad that accounts for almost half of all the infectious disease mortality. Malaria is transmitted by the bite of an infected female *Anopheles* mosquito that transfers to the human host up to four different species of *Plasmodium* parasites. Traditionally, malaria has been treated with quinolines. Unfortunately, most of the parasites responsible for the vast majority of fatal malaria infections, have become resistant to quinolines. Today, the most potent antimalarials available are artemisinins, extracted from sweet wormwood (*Artemisia annua*), rapidly killing all asexual stages of *Plasmodium falciparum* by specifically inhibiting its sarcoendoplasmic reticulum Ca^{2+} ATPase ortholog [140]. The special feature of Artemisinin is an endoperoxide group which can be cleaved or dissociated by interaction with iron ions or light [141]. Therefore, the synthesis of new drugs with endoperoxide groups plays an important role in the development of new prodrug prototypes to treat malaria [138].

Molecules with endoperoxide groups are also interesting for photodynamic therapy (PDT) [139]. In traditional PDT, a photosensitive drug is excited by light in the presence of ground state molecular oxygen, which is abundant in tissues/cells, to produce singlet molecular oxygen, $^1O_2$, as well as other cytotoxic agents. These, and $^1O_2$ cause severe physiological damage in selected cell subunits, such as cell membranes, and lead subsequently to cell death [142]. In the first step of PDT the dye is administered to the patient, where it accumulates in the tumor tissues [143]. Next, the target area is irradiated directly by a light source of a wavelength where the photosensitizer absorbs. Upon

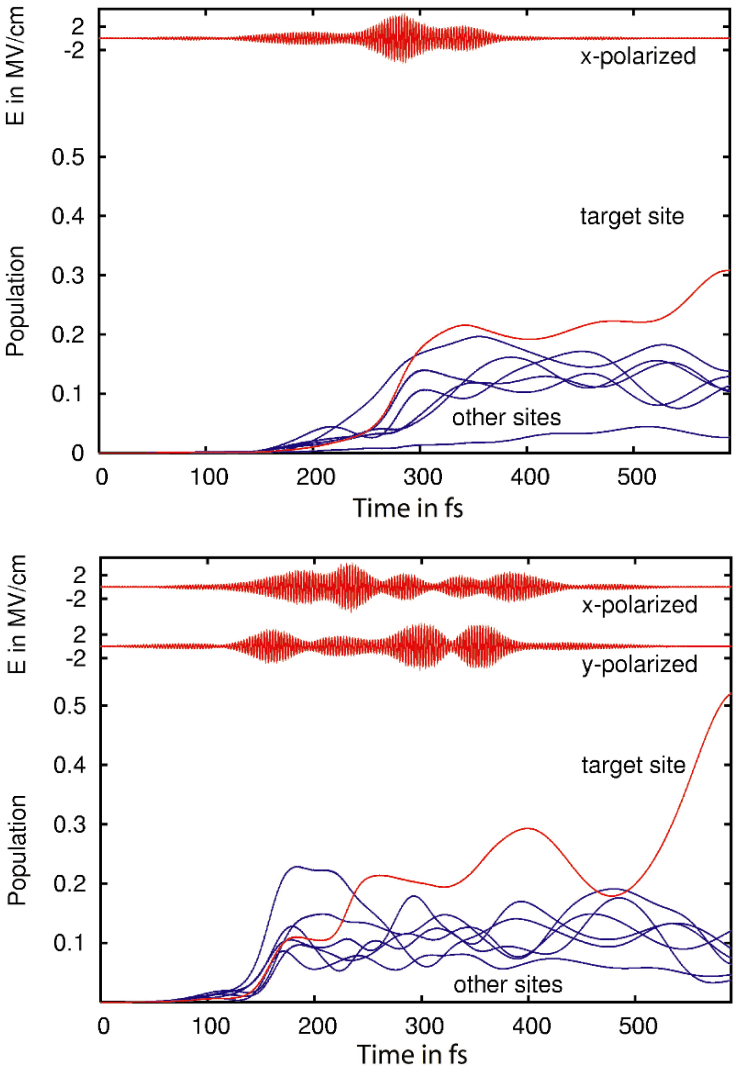

Fig. 9.29. Disorder averaged chromophore populations in the FMO complex at the target site $m_{\mathrm{tar}} = 7$ (and at all other sites). Upper panel: use of a linearly polarized control pulse, lower panel: the optimization covered the independent two polarization directions of the field. An ensemble of 10 complexes with randomly chosen spatial orientation and fluctuating on–site energies E_e ($\sigma = 100$ cm^{-1}) has been considered. The temporal evolution of the field components is shown in the upper part of both panels.

light absorption, (see Fig. 9.30), the photosensitizer is excited to the first excited singlet state S_1, from where it can again return to the ground state S_0 or alternatively reach the first excited triplet state T_1 through intersystem crossing (ISC). Once the first triplet excited state is formed, two different types of interaction mechanisms might occur between the photosensitizer and the target substrate [144]. Photodynamic reactions of type I are those where the photodynamic damage is mainly caused by radical photosensitizer intermediates. Reactions of type II, on the other hand, involve energy transfer (ET) from the triplet state of the photosensitizer to ground state triplet oxygen $^3O_2$, resulting in $^1O_2$ and other reactive oxygen species (ROS).

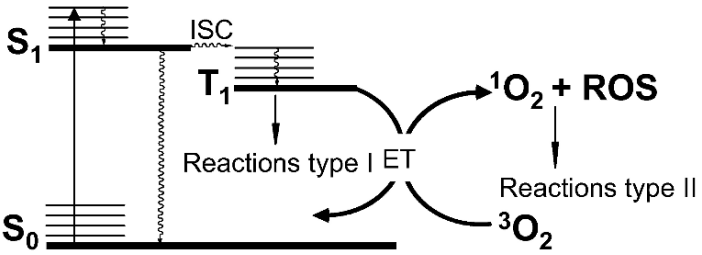

Fig. 9.30. Scheme for singlet oxygen generation [142]. The initial step is the excitation of the photosensitizer ($S_0 \rightarrow S_1$). By intersystem crossing (ISC) the triplet T_1 is populated ($S_1 \rightarrow T_1$). Deactivation of the triplet photosensitizer state is followed by conversion of the oxygen triplet ground state $^3O_2$ into the singlet oxygen state $^1O_2$ and the generation of other reactive oxygen species (ROS).

Necessary properties for drugs to be used as photosensitizers are high and selective accumulation in target tissues, absorption in the phototherapeutic window 600-1200 nm, high yields in generation of the excited triplet state T_1, and of course minimal adverse effects. The use of PDT in biological tissues is limited to a few millimeters depth, due to strong scattering and photon loss $I = I_0 \exp(-\sigma_t x)$. Here, I_0 and I are the light intensities in front of and inside the biological tissue, σ_t is the total damping cross section, which is a sum of the scattering cross section σ_s and the absorption cross section σ_a, and x is the depth in the sample. Typically, the scattering coefficient σ_s decreases from $120\,\mathrm{mm}^{-1}$ at 400 nm to $20\,\mathrm{mm}^{-1}$ at 1800 nm, whereas the absorption coefficient varies between $40\,\mathrm{mm}^{-1}$ and $0.01\,\mathrm{mm}^{-1}$ in the same spectral region. Thus, the transmitted light intensity in 1 mm depth of biological tissue is only 0.027 % at 600 nm and 4.07 % at 1600 nm. Since the intensity of the transmitted light increases for longer wavelengths, an ideal photosensitizer should preferably absorb at long wavelengths. However, the generation of singlet oxygen from abundant ground state oxygen requires an energy of more than 1270 nm, restricting the absorption of photosensitizers to wavelengths shorter than 1270 nm. As a consequence, for single photon excitation the

phototherapeutic window ranges from 600 nm to 1200 nm. An alternative approach in PDT is the use of two-photon excitation processes with shaped laser pulses of longer wavelengths, and concomitantly higher light transmission in biological tissues. This could accomplish better excitation and higher selectivity in the presence of molecules with similar one-photon absorption, e.g. the melanin pigment [145].

A special kind of photosensitizers are those which contain an endoperoxide group, so-called oxygen-carrier photosensitizers. These photosensitizers are able to generate $^1O_2$ directly upon irradiation, contrary to conventional ones. One such case is anthracene-9,10-endoperoxide, (APO), which has been chosen in the present study as a model to understand the photochemical behavior of aromatic oxygen-carrier photosensitizers.

Oxygen-carrier photosensitizers, such as APO, can show different photochemical behaviors and reaction mechanisms depending on the excitation wavelength. As shown in Fig. 9.31, two competing photodissociation mechanisms can take place in APO upon ultraviolet (UV) irradiation: a) O-O homolysis, resulting in oxygen biradical rearrangement products, and b) cycloreversion, either concerted or stepwise, producing singlet oxygen and the parent hydrocarbon.

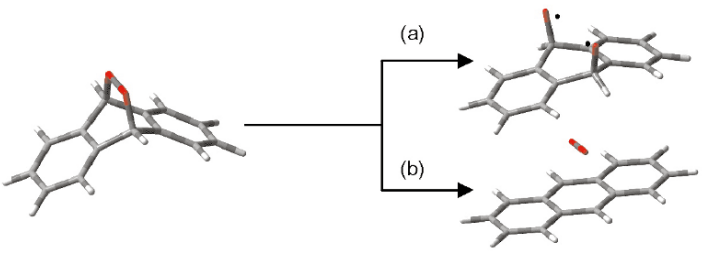

Fig. 9.31. Photodissociation products of APO by: (a) O-O homolysis (b) cycloreversion.

Much has been published on APO and related derivatives; however, the detailed photodissociation mechanism is still unclear. In the following we present new experimental and theoretical data on APO's photochemistry attempting to increase the understanding of the APO photochemical mechanisms.

The first studies dealing with the photochemistry of endoperoxides date from 1969. Through orbital and state correlation diagrams obtained from thermochemical/spectroscopical data and symmetry/spin selection rules, Kearns and Khan [146] postulated that the excitation of small size endoperoxides to their first excited singlet or triplet states leads to the cleavage of the O-O endoperoxide bond, and therefore to the formation of oxygen biradicals, (see Fig. 9.31a), while the excitation to higher-lying excited states, which imply

promotion of an electron from a π^*_{OO} orbital to a σ^*_{CO} orbital, induces the endoperoxide photodissociation into the parent hydrocarbon and singlet oxygen, (see Fig. 9.31b). This can be easily rationalized taking into account that the population of antibonding σ^*_{OO} and σ^*_{CO} orbitals leads to a weakening of the O-O and C-O bonds, respectively, and therefore favors the cleavage of these respective bonds.

Some time later, in 1984 Brauer and coworkers [147] recorded experimental absorption spectra of APO in CH_2Cl_2 and studied its UV photolysis. In agreement with Kearns and Khan's predictions [146], they assigned the first excited singlet state S_1 at 384-300 nm to the $\pi^*_{OO} \rightarrow \sigma^*_{OO}$ transition, which they found leads to rearrangement products with origin in the homolytic rupture of the endoperoxide bridge. They also found cycloreversion products, with origin in higher energy excited states, $S_n \geq 2$, at $\lambda \leq 278$ nm, characterized by $\pi_{CC} \rightarrow \pi^*{}_{CC}$ transitions.

Experimental wavelength-dependent photodissociation studies on phenylated and methylated derivatives of anthracene-9,10-endoperoxides, were performed by Eisenthal et al. [148] and Rigaudy et al. [149]. They found the same general photodissociation trends as reported by Brauer and coworkers [147]. The picosecond time-resolved measurements carried out by Eisenthal et al. [148] allowed, in addition, to postulate a nonconcerted mechanism for the loss of molecular oxygen, based on the unusual long rise times (50-75 ps) observed for the cycloreversion process.

More recent Ar-matrix experiments supported by semiempirical CNDO/S and INDO/S calculations carried out by Klein and coworkers [150] suggested, however, that the well-accepted assumption of cycloreversion occurring from the S_2 excited state was wrong. Excitation to the S_1 state at 275 nm led to cycloreversion products and their calculations predicted a $\pi_{CC} \rightarrow \pi^*_{CC}$ character for the S_1 state, concluding that O-O homolysis products may have their origin in the triplet manifold.

These controversial results clearly call for further experiments as well as for high level ab initio quantum chemical calculations, beyond semiempirical and state correlation diagrams. In the following, results obtained by using multiconfigurational ab initio theory and femtosecond polarization resolved UV pump IR probe spectroscopy are presented. This combined theoretical and experimental study contributes to clarifying the mechanisms behind both cycloreversion and O-O homolysis reactions, with the long term goal to understand and optimize drugs with endoperoxide groups.

Computational Details

All the calculations on APO were done at the ab initio (see Chapter 3, Sect. 3.2.1) multiconfigurational Complete Active Space Self Consistent Field [151] (CASSCF) level of theory in combination with the Small Atomic Natural Orbital Basis Set [152] (ANO-S) as implemented in the quantum chemistry package MOLCAS 6.0 [153]. The calculations were performed on the C_{2v}

equilibrium geometry optimized at MP2 level of theory with the 6-311G(d,p) Pople Split Valence Triple Zeta Basis Set, supplemented with d and p diffuse functions on heavy and hydrogen atoms, respectively. In order to include dynamic correlation effects, the CASSCF electronic energies were corrected using Multi-State Complete Active Space Perturbation Theory to the Second Order [154] (MS-CASPT2).

The full active space for the description of the system in its equilibrium geometry consists of 6 pairs of π_{CC} and π^*_{CC} orbitals belonging to the anthracene moiety, together with the π_{OO}, π^*_{OO}, σ_{OO} and σ^*_{OO} orbitals localized in the endoperoxide bridge. This amounts to a total of 18 electrons in 16 orbitals, resulting in 27810640 configurations, impracticable from the computational point of view. Our effective active space for describing the equilibrium structure of APO is therefore reduced to 14 electrons in 12 orbitals, CAS(14,12), disregarding the two lowest and highest energy π_{CC} and π^*_{CC} occupied and virtual orbitals, respectively. To describe the C-O dissociation problem, the σ_{CO} and σ^*_{CO} orbitals are additionally included in the active space.

In order to assess the performance of the chosen theoretical procedure and basis set, other basis sets and active spaces were as well employed. The comparison of MS-CASPT2(14,12)/ANO-S//CASSCF(14,12)/ANO-S vertical excitation energies for the first singlet excited states with those obtained with the Large Atomic Natural Orbital basis set [155] (ANO-L) and with a (16,14) active space, shows differences of 2-3 kcal/mol, that lie within the error inherent of the employed methods, justifying our choice.

Experimental Details

APO was dissolved in deuterated chloroform ($CDCl_3$) at a concentration of 70 mM (sample thickness 0.1 mm, temperature 293 K). The APO absorption spectrum exhibits clear absorption peaks at 271 nm and 279 nm in the UV spectrum as shown in Fig. 9.32 and gives rise to the infrared absorption bands shown in Fig. 9.33. Femtosecond pump and probe pulses at 273 nm and 1170 cm^{-1}, respectively, were generated with a cross correlation time between the pump and probe pulses of 300 fs (FWHM). Measurements were performed with parallel and perpendicular linear polarization of pump and probe pulses. The absorbance change was derived from measurements with parallel $\Delta A_{\parallel}(t_D) = -\log(T_{\parallel}(t_D)/T_{\parallel 0})$; ($T_{\parallel}(t_D)$, $T_{\parallel 0}$: sample transmission with and without excitation (respectively), t_D: delay time), and perpendicular ($\Delta A_{\perp}(t_D)$) polarization. The relative angle of the electronic transition dipole moment to the vibrational transition dipole moment was derived using the formulas: $D = \Delta A_{\parallel}(t_D)/\Delta A_{\perp}(t_D)$ and $\vartheta = \arccos\sqrt{\frac{2D-1}{D+2}}$. The orientations of the calculated electronic transition dipole moments within the APO molecule are shown in Fig. 9.32. The orientations of the vibrational dipole moments in the electronic ground state were calculated on the geometry given in

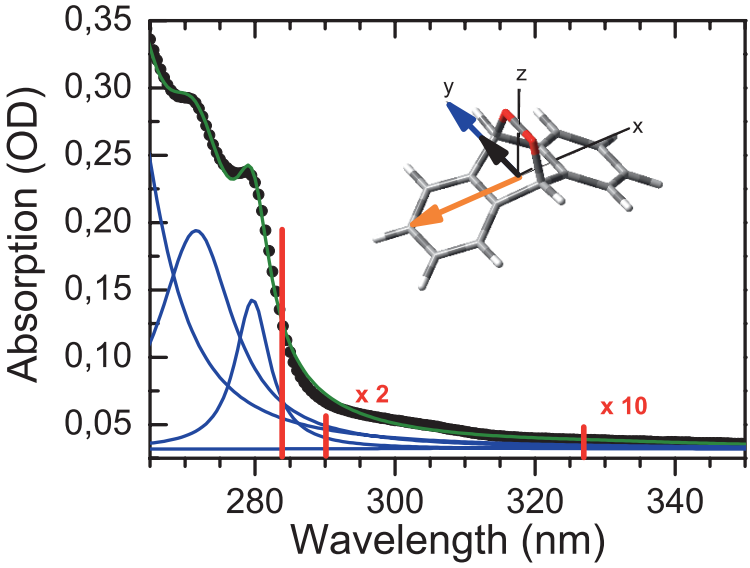

Fig. 9.32. Absorption spectrum of APO in chloroform ($CDCl_3$) (circles); Multiple Lorentzian Fit: green line; individual peaks: blue lines; calculated transitions: red bars. The inset shows the APO optimized geometry used in the calculations. The arrows indicate the orientations of transition dipole moments. $S_0 \rightarrow S_1$ and $S_0 \rightarrow S_2$ transition dipole moment (yellow arrow); vibrational transition dipole moment of the C-H bending vibrations of APO (black arrow); $S_0 \rightarrow S_4$ transition dipole moment (blue arrow).

Fig. 9.32 using Density Functional Theory (DFT) at B3LYP/6-31G* level of theory, as implemented in Gaussian03 [156].

9.5.1 Assignment of the absorption spectrum

In Fig. 9.32 the lowest energy part of the linear absorption spectrum of APO in deuterated chloroform (circles) is plotted together with the gas phase calculated spectrum (red bars). In the experimental absorption spectrum two distinct bands appear at 271 nm and 279 nm. The band at 271 nm has an oscillator strength 4.5 times higher than the band at 279 nm. A third very weak band around 300 nm can only be found at higher concentrations (data not shown). To gain deeper insight into the origin of these absorption bands quantum chemistry calculations were performed on the gas phase optimized geometry given in Fig. 9.32. Gas phase MS-CASPT2 vertical excitation energies are presented in Table 9.1. The first singlet excited state S_1 of APO is found to have B_1 symmetry and is assigned to a $\pi^*_{OO} \rightarrow \sigma^*_{OO}$ transition

Table 9.1. MS-CASPT2/CASSCF vertical singlet excitation energies (ΔE in nm), corresponding assignments, oscillator strengths f, and x,y,z transition dipole moment (TDM) components. Most intense bands are highlighted in color.

State	Symmetry	Assignment	ΔE	f	TDM (x/y/z)
S_0	1^1A1	—	0.00	—	—
S_1	1^1B1	$\pi^*_{OO} \rightarrow \sigma^*_{OO}$	327	0.0003	(0.06/0/0)
S_2	2^1B1	$\pi_{CC} \rightarrow \pi^*_{CC}$	290	0.0021	(-0.14/0/0)
S_3	1^1A2	$\pi^*_{OO} \rightarrow \pi^*_{CC}$	286	0.0000	—
S_4	1^1B2	$\pi^*_{OO} \rightarrow \pi^*_{CC}$	284	0.0220	(0/-0.45/0)
S_5	2^1A2	$\pi_{CC} \rightarrow \pi^*_{CC}$	267	0.0000	(0/0/0.10)
S_6	2^1A1	$\pi_{CC} \rightarrow \pi^*_{CC}$	266	0.0011	—

absorbing at 327 nm with a very weak oscillator strength. The second singlet state S_2 displays also B_1 symmetry and corresponds to a $\pi_{CC} \rightarrow \pi^*_{CC}$ transition. This band is centered at 290 nm and according to the computed oscillator strength it should be about 7 times more intense than the S_1 band. The transition from the ground to the fourth singlet state S_4 with B_2 symmetry is the next band with nonzero oscillator strength. The excitation is assigned to a $\pi^*_{OO} \rightarrow \pi^*_{CC}$ transition absorbing at 284 nm with a 10 times higher oscillator strength than the $S_0 \rightarrow S_2$ transition.

The comparison of theoretically and experimentally determined absorption bands (cf. Fig. 9.32) shows a good agreement of the experiment and the gas phase calculations, if taking into account a small shift due to the solvent. The experimental absorption bands of APO in chloroform are located at 271 nm, 279 nm, and about 305 nm with decreasing oscillator strengths. The calculated ab initio MS-CASPT2 excitation energies (red bars) are located red shifted at 284 nm, 290 nm, and 327 nm, also with decreasing oscillator strengths (see Table 9.1). Taking into account the blue shifting of the experimental bands due to solvent effects with respect to the gas phase theoretical calculations, the following tentative assignment of the experimental spectrum is made: the experimental band centered at 271 nm is assigned to the $\pi^*_{OO} \rightarrow \pi^*_{CC}$ transition, and the band at 279 nm is assigned to the $\pi_{CC} \rightarrow \pi^*_{CC}$ transitions. Both are red-shifted compared to the gas phase theoretical calculations. Finally, the spectral tail lying between 290-320 nm is attributed to the $\pi^*_{OO} \rightarrow \sigma^*_{OO}$ transition, which is theoretically predicted at 327 nm with a very low oscillator strength.

These results are also consistent with the early theoretical work of Kearns and Khan [146]. Furthermore, they are in reasonable agreement with the ex-

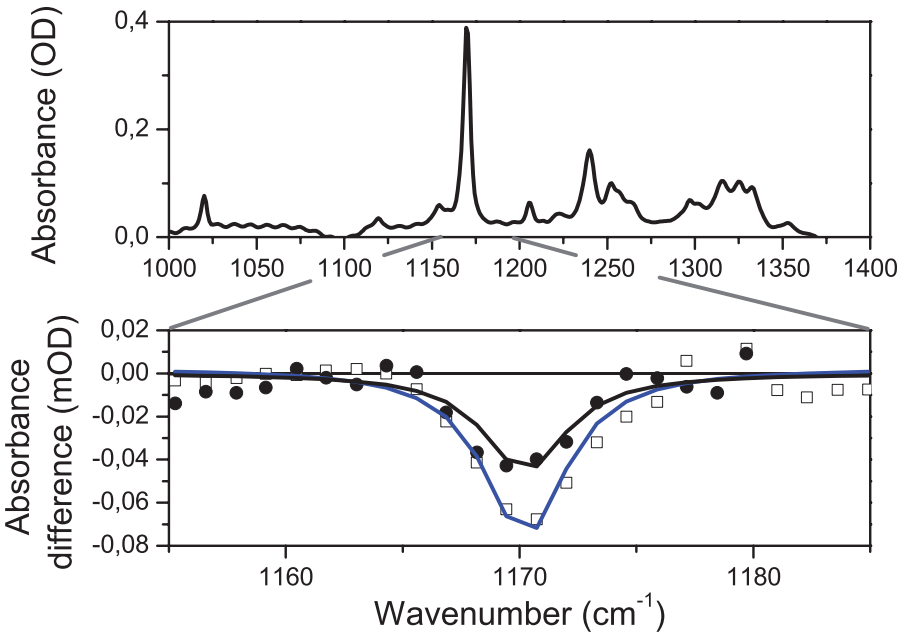

Fig. 9.33. Upper panel: Infrared absorption spectrum of APO in chloroform; Lower panel: Absorbance difference 25 ps after APO excitation with 273 nm. Black line: Lorentzian fit of the bleaching signal (solid circles) with perpendicular polarized light pulses. Blue line: Lorentzian fit of the bleaching signal (open squares) with parallel polarized light pulses. The ratio of the bleach amplitudes correspond to a relative angle of $28 \pm 20^{\circ}$ between electronic and vibrational TDM.

perimental APO absorption spectrum recorded in solutions of CH_2Cl_2 and CH_3CN, reported by the groups of Brauer [147], Rygaudy [149], and Eisenthal [148], respectively.

On the other hand, our results differ significantly from the semiempirical calculations and experimental work of Gudipati and coworkers [150] who did not find any low-lying transitions involving a significant contribution of endoperoxide orbitals, and reported, instead, anthracene and $^1O_2$ cycloreversion products as the only reaction products observed upon UV irradiation.

In order to confirm the theoretical assignments, the character of the excited states are probed experimentally by determining the orientation of the electronic transition dipole moment (TDM) within the molecule. This is done by measuring the relative angle between the orientations of the electronic TDM and a specific vibrational transition dipole moment, whose orientations are related to the geometry of the molecule.

Comparison of the calculated and measured relative angles between the electronic and vibrational transition dipole moments can help elucidating the character of the excited state transition. In APO, the orientations of the elec-

tronic TDMs are the same for $S_0 \rightarrow S_1$ and $S_0 \rightarrow S_2$ transitions: parallel to the x-axis (orange arrow in Fig. 9.32). However, the $S_0 \rightarrow S_4$ transition is perpendicular to these, and parallel to the y-axis (blue arrow in Fig. 9.32). The investigated C-H bending vibration $\delta(CH)$ of APO (black arrow in Fig. 9.32) around 1170 cm^{-1} has a vibrational dipole moment oriented parallel to the y-axis. Excitation at 273 nm results in a bleaching of the $\delta(CH)$ absorption band. The bleaching signal of the vibrational $\delta(CH)$ transition at 1170 cm^{-1} is plotted in Fig. 9.33 for different relative polarization directions of the pump and the probe beam. The bleaching for probing with perpendicular polarized light is weaker than for probing with parallel polarized light indicating a relative angle of less than 54.7. Analysis of the bleaching signal gives an angle of 28 ± 20, indicating an orientation of the electronic TDM excited at 273 nm more parallel to the y-axis than to the x-axis. Thus, the absorption band at 273 nm can be assigned to the $S_0 \rightarrow S_4$ transition, and not to the $S_0 \rightarrow S_1$ or $S_0 \rightarrow S_2$ transitions. These findings support the above assignment of the absorption bands and the calculated character of the transitions. To summarize: on the basis of the new data we assign the absorption band at 271 nm to the $S_0 \rightarrow S_4$ transition, the band at 279 nm to the $S_0 \rightarrow S_2$ transition and the band around 300 nm, which exhibits a very low oscillator strength, both in the experiment as well as in the calculations, to the $S_0 \rightarrow S_1$ transition.

9.5.2 Analysis of Photodissociation Mechanisms

In order to get more insight into the dual photodissociation mechanism of APO, the dissociation curves for its ground and lowest energy excited states along the two relevant coordinates leading to oxygen biradical rearrangement, R_{OO}, and cycloreversion products, R_{CO}, were calculated at the MS-CASPT2/ANO-S//CASSCF/ANO-S level of theory. The potential energy curves for homolytic O-O endoperoxide bond breaking are plotted in Fig. 9.34, while the potentials for the concerted and step-wise photodissociation mechanism associated to the C-O cleavage are shown in Figs. 9.35a and 9.35b, respectively.

From the S_1 energy profile plotted in Fig. 9.34, which shows a $\pi^*_{OO} \rightarrow \sigma^*_{OO}$ character, it can be observed that the electronic energy decreases as the R_{OO} distance is increased, reaching its minimum around 2.1 Å. From there, it starts to increase again, showing thereby a binding character. As already stated before, electron excitation into σ^*_{OO} orbitals would significantly weaken the O-O endoperoxide bridge favoring its homolytic rupture. This way, APO molecules excited into the S_1 state would be "trapped" in this potential. Preliminary wave packet simulations in this one-dimensional model indicate vibrational oscillations of ca. 80 fs (full period); at longer time scales, the vibrational energy is expected to be dissipated into other normal modes, leading to relaxed oxygen diradical molecules that would finally evolve to lower energy rearrangement products. This is consistent with the photolysis results published in the works of Brauer [147] and Eisenthal, [148] who obtain rearrangement

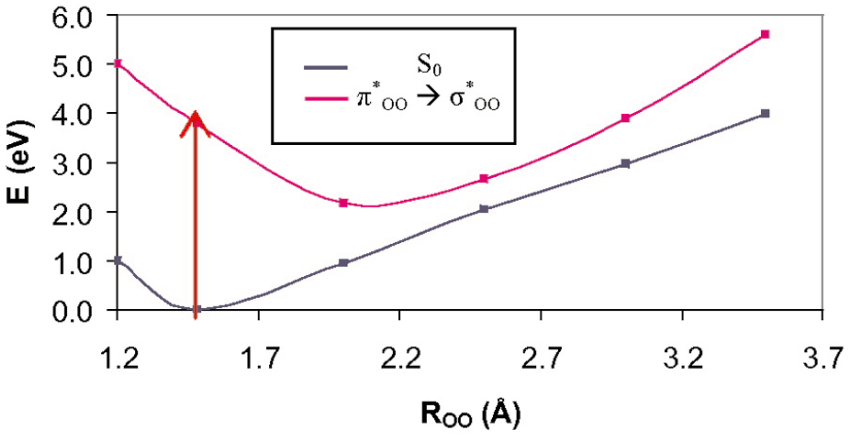

Fig. 9.34. Potential energy curves for the ground and the lowest energy B_1 singlet excited states of APO along the R_{OO} dissociation coordinate. The red arrow indicates the experimental irradiation frequency, which results in the observation of oxygen diradical rearrangement products [147].

products and the parent aromatic hydrocarbon, upon irradiation of APO or 1,4-dimethyl-9,10-diphenyl-9,10-anthracene-endoperoxide at $\lambda \geq 270$nm.

In order to study the mechanism behind cycloreversion processes, the lowest B_1 states along the C-O dissociation coordinate for the concerted and step-wise singlet oxygen loss were also computed. The concerted dissociation of the two C-O bonds in APO is described by considering the stretching of both C-O distances, while keeping the rest of the degrees of freedom frozen. The potential's profile of Fig. 9.35a points to the existence of a conical intersection between the $\pi_{CC} \rightarrow \pi^*_{CC}$ (S_2) excited state, populated upon irradiation, and the $\pi^*_{OO} \rightarrow \sigma^*_{CO}$ dissociative state. The population of σ^*_{CO} orbitals through the conical intersection is consistent with the weakening of the CO bond and the subsequent oxygen loss. However, this process is highly unlikely to occur as the curve crossing is located significantly above the experimental irradiation energy [147]. These findings, therefore, indicate that the possibility that the cycloreversion process takes place through a concerted mechanism should be ruled out a step-wise cycloreversion is more favourable.

In order to model the step-wise mechanism for the molecular singlet oxygen loss, we considered the cleavage of a single C-O bond, keeping the second C-O distance as well as the other reaction coordinates frozen. Figure 9.35b displays schematically the diabatic potential energy curves for the ground electronic state and the lowest energy states of B_1 symmetry of APO. Similar to the concerted cycloreversion mechanism, several singlet/singlet crossings also can be observed for the nonconcerted mechanism. Starting from the $\pi_{CC} \rightarrow \pi^*_{CC}$

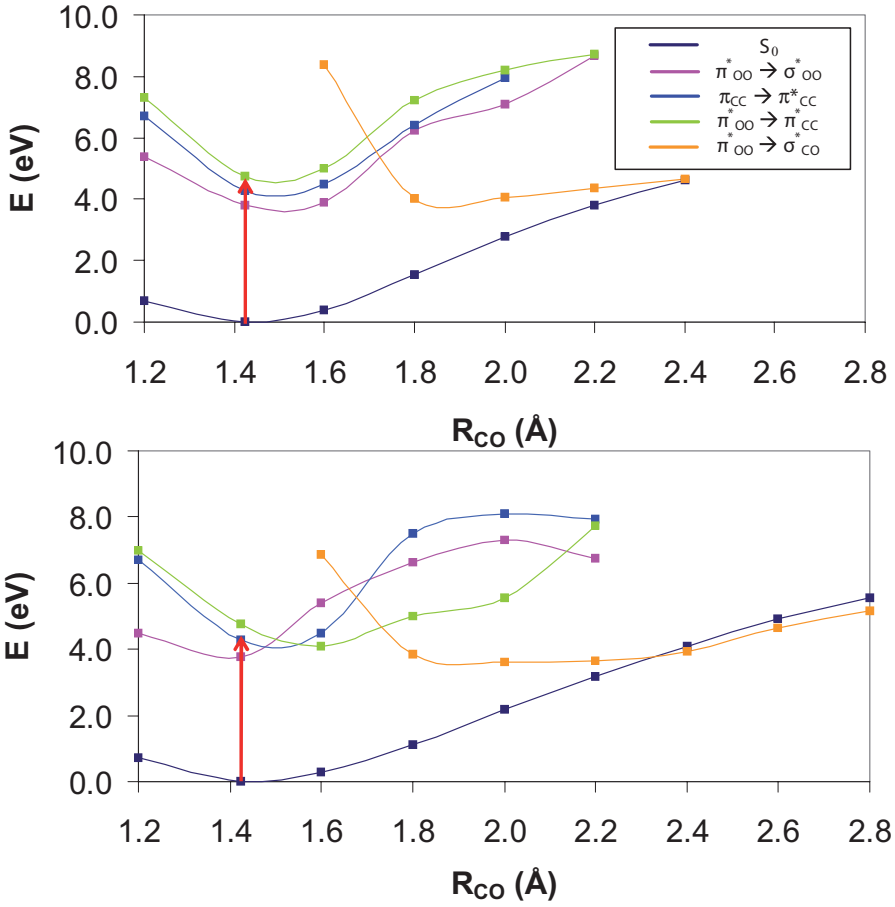

Fig. 9.35. Diabatic potential energy curves for the ground and the lowest energy B_1 singlet excited states of APO along the R_{CO} dissociation coordinate, assuming a concerted (a) and a step-wise mechanism (b) for $^1O_2$. The red arrow represents the experimental irradiation energy that results in the observation of cycloreversion products [147].

S_2 excited state, which is the only accessible state for irradiation at $\lambda \geq$ 279nm, the system would be able to overcome the S_2/S_1 and S_2/S_3 crossings through vibronic couplings, finally reaching the $\pi^*_{OO} \rightarrow \pi^*_{CC}$ S_3 excited state, which in turn presents a crossing around a R_{CO} distance of 1.70 Å with the $\pi^*_{OO} \rightarrow \sigma^*_{CO}$ dissociative state, directly associated with singlet oxygen loss. The main difference to the concerted mechanism is that in this case all the calculated singlet/singlet crossings, including the $\pi^*_{OO} \rightarrow \pi^*_{CC}$/ $\pi^*_{OO} \rightarrow \sigma^*_{CO}$ curve crossing lie below the energy stored by the system upon irradiation; therefore, through nonadiabatic dynamics fragmentation can occur. Once

more, these results are consistent with the experimental cycloreversion quantum yields ranging from 0.25-0.35, reported in Brauer's [147] and Eisenthal's [148] work when they irradiated at the wavelength region assigned to the S_2 band.

As seen in Fig. 9.35, a second crossing for a R_{CO} distance of 2.35 Å, is also found between the dissociative $\pi^*_{OO} \rightarrow \sigma^*_{CO}$ and APO's ground. This would account for the portion of the quantum yield returning back to the ground state.

Finally, it is worth mentioning that our high-level quantum mechanical description of the photodissociation mechanisms of APO agrees well with the theoretical calculations made by Kearns and Khan, [146] who predicted cycloreversion and O-O homolysis products from $\pi^*_{OO} \rightarrow \sigma^*_{CO}$ and $\pi^*_{OO} \rightarrow \sigma^*_{OO}$ transitions, respectively.

9.5.3 The role of triplet excited states

Until here, only the role of singlet excited states in O-O homolysis and cycloreversion reactions has been discussed. However, some authors [146, 148, 150] have pointed to the possible role of excited triplet states in the homolytic O-O bond rupture. Our MS-CASPT2/CASSCF vertical triplet state energies show that the first triplet excited state, similar to the first singlet excited state, has a $\pi^*_{OO} \rightarrow \sigma^*_{OO}$ character. The next higher energy triplet states exhibit $\pi_{CC} \rightarrow \pi^*_{CC}$ and $\pi^*_{OO} \rightarrow \pi^*_{CC}$ character and show different symmetry. There are three triplet states lying in between the S_0 and S_1 state and four triplet states in between the S_1 and S_2 state. From these facts, one could expect the occurrence of a nonnegligible probability for intersystem crossing. Nevertheless, no definitive conclusions can be drawn without computing potential energy surfaces along the R_{OO} and R_{CO} dissociation coordinates and corresponding spin-orbit couplings.

In summary, anthracene-9,10-endoperoxide has been chosen as a model to understand the photochemical behavior of aromatic oxygen carrier photosensitizers with endoperoxide groups. These are able to directly release singlet oxygen upon light irradiation, which is the main cytotoxic agent used in photodynamic therapy for the treatment of cancers and against viral/bacterial diseases.

Upon UV irradiation, endoperoxides exhibit at least two different photodissociation processes: i) cycloreversion reactions that lead to molecular singlet oxygen and the parent aromatic hydrocarbon, and ii) O-O homolysis reactions that lead to oxygen diradical rearrangement products. Using nonlinear femtosecond polarization resolved spectroscopy and ab initio multiconfigurational MS-CASPT2/CASSCF calculations the linear absorption spectrum and the character of the low energy excited states of APO has been assigned.

9.6 Metastable conformational structure and dynamics: Peptide between gas phase via clusters and aqueous solution

E. Meerbach, C. Schütte, I. Horenko, and B. Schmidt

The dynamics of biomolecular systems is characterized by the existence of biomolecular conformations which can be understood as metastable geometrical large scale structures [157]. On the longest time scales, biomolecular dynamics is dominated by flipping processes between these conformations, while on shorter time scales, the dynamical behavior is governed by flexibility within these conformations, resulting in a rich temporal multiscale structure of time-dependent observables. An approach to characterize biomolecular dynamics is to construct reduced models reflecting the "effective dynamics" of the system.

It is a promising idea to describe the effective dynamics of a biomolecular systems by means of a Markov chain with discrete states $D_1, \ldots, D_m$, representing the metastable conformations, and a transition matrix $P = (p_{kj})$, describing the "flipping dynamics" between these states. Efficient algorithmic identification of the metastable conformations is a challenging problem, which has recently been tackled by set-oriented approaches [158–160]. In the context of the present work Hidden Markov Models (HMM) are used to extract the effective dynamics between hidden metastable molecule conformations from observable time series. e.g. the torsional angles of the backbone of biopolymers obtained by MD simulations [161]. In addition, the flexibility within conformations can be modeled by stochastic differential equations (SDE), thus comprising the HmmSde model [162–164]. As the description of internal flexibility by SDEs also accounts for relaxation from one metastable conformation to another, this approach narrows the gap between "flipping dynamics" and transition path computation, as described in, e.g., [165].

9.6.1 Metastability and the transfer operator approach

In the following we shortly summarize the algorithmic idea of the transfer operator approach, omitting most of the theoretical background. Instead we concentrate on the question how to set up an effective dynamics from a given time series, e.g., trajectory data. The reader interested in a mathematically more rigorous description is referred to [159, 166–169], readers not familiar with the basic notations of Markov chain theory are referred to [170]. First we explicate the concept of metastability of a Markov chain and the key idea for the identification of metastable states. Note that the transfer operator is an object in continuous state space, while we present the concept on discrete state space. Therefore only the discretized equivalent of the transfer operator, the transition matrix, appears in the following.

Consider a Markov chain $\{X_k\}_{k\in\mathbb{N}}$ on a discrete state space $\mathbf{X} = \{1, 2, \ldots, n\}$ specified by a stochastic transition matrix $P = (p_{kj})$, with

$$p_{kj} = \mathbb{P}\left[X_{l+1} = j | X_l = k\right],$$

denoting the conditional probability to jump from k to j within one time step. Furthermore, assume that the Markov chain is irreducible, aperiodic and reversible, i.e. a unique and strictly positive stationary distribution $\pi = (\pi_k)$ exists with $\pi_k p_{kj} = \pi_j p_{jk}$ for all $k, j \in \mathbf{X}$. A subset $B \subset \mathbf{X}$ is called metastable if

$$\mathbb{P}\left[X_{l+1} \in B | X_l \in B\right] \approx 1,$$

i.e., if the process is in subset B it is very likely to stay there within the next time step.

A decomposition $\mathrm{d} = \{D_1, \ldots, D_m\}$ of the state space $\mathbf{X}$ is defined as a collection of disjoint subsets $D_k \subset \mathbf{X}$ covering $\mathbf{X}$, i.e. $\cup_{k=1}^{m} D_k = \mathbf{X}$. The metastability of a decomposition d is defined as the sum of the metastabilities of its subsets, i.e. for each arbitrary decomposition d_m of the state space $\mathbf{X}$ into m sets its metastability measure is defined as

$$M(\mathrm{d}_m) = \sum_{j=1}^{m} \mathbb{P}\left[X_{l+1} \in D_j | X_l \in D_j\right].$$

For given m, the optimal metastable decomposition into m sets maximizes the functional M. In particular the appropriate number m of metastable subsets must be identified. Both the determination of m and the identification of the metastable subsets can be achieved via spectral analysis of the transition matrix P, as the following holds:

> Due to reversibility, all eigenvalues of the transition matrix P are real. Metastable subsets can be detected via eigenvalues close to the maximal dominant eigenvalue $\lambda = 1$, i.e., the number of metastable subsets in the metastable decomposition is equal to the number of eigenvalues close to 1, including $\lambda = 1$ and accounting for multiplicity, while the rest of the spectrum is separated through a spectral gap from 1. Among other possibilities, the sign structure of the eigenfunctions allows the identification of the metastable subsets [159, 168, 171].

Therefore the road map to determine metastable states on basis of a time series reads as follows:

1. Discretize the state space of the time series and extract a transition matrix by counting transitions between the discrete states.
2. Use the spectral properties of the transition matrix to obtain metastable sets, yielding a coarse-grained description.

There are two remarks to be made on this road map.
First: Discretizing the state space is a nontrivial task, as typical biomolecular systems contain hundreds or thousands of degrees of freedom. Fortunately,

chemical observations reveal that—even for larger biomolecules—the curse of dimensionality can be circumvented by exploiting the hierarchical structure of the dynamical and statistical properties of biomolecular systems: only relatively few essential degrees of freedom may be needed to describe the conformational transitions.
Second: After discretizing the state space there is a choice in the lag time τ used to obtain the transition matrix. If τ^* is the time step between subsequent data points then the lag time τ can be set to $r\tau^*$ by evaluating transitions from every kth sampled step to every $(k+r)$th, $r \geq 1$, sampled step. Taking $r > 1$ corresponds to a coarser discretization of the time domain of the originally continuous dynamics. Different values of r give rise to different transition matrices. Therefore, subsets of the state space are metastable with respect to a certain timescale. By choosing r sufficiently large one can decrease correlations between subsequent time steps and therefore ensure that the Markov description is a proper description.

9.6.2 Illustrative example

We give a short and simplistic example to highlight the procedure outlined above. Consider the one dimensional time series $(Y_t)_{t=t_1,\ldots,t_N}$, with constant sampling time $\tau^* = t_{j+1} - t_j$, shown in Fig. 9.36, which clearly exhibits metastable behavior. We discretize the state space $[-180\ 180]$ into 9 equidistant boxes, the numbering of the boxes randomly chosen. If $N_r(j,k)$ denotes the number of transitions from box j to box k in r steps and $N_r(k)$ the number of data points in box k, we obtain a reversible transition matrix $P = (p_{kj})$, with respect to the time lag $\tau = r * \tau^*$, by setting

$$p_{kj} = \frac{N_r(j,k) + N_r(k,j)}{N_r(j) + N_r(k)}. \tag{9.11}$$

The obtained matrix seems to exhibit no special structure, but computing the spectrum, for $r = 1$, yields

$$\sigma(P) = \{1, 0.98, 0.55, 0.34, \ldots\},$$

indicating two metastable states. The information contained in the eigenvector belonging to the second eigenvalue is used to identify the metastable subsets, i.e. boxes with the same eigenvector sign are assigned to the same metastable state. Permuting the matrix such that boxes belonging to the same metastable set are neighbors, results in a dominantly blockdiagonal structure. Aggregating the states in each metastable set results in a two state "effective dynamics" with transition matrix

$$\begin{pmatrix} 0.989 & 0.011 \\ 0.013 & 0.987 \end{pmatrix},$$

and a stationary distribution $\pi = (0.56\ 0.44)^T$.

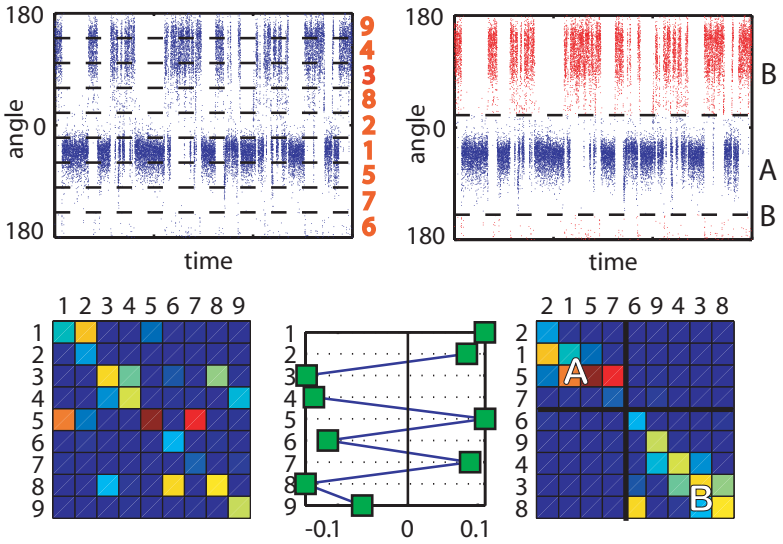

Fig. 9.36. Top left: A time series of circular data. The equidistant space discretization in 9 randomly numbered boxes is indicated with dashed lines. Bottom left: The obtained stochastic transition matrix, blue (dark) color represents entries near zero, while red (light) entries are corresponding to entries close to one. Bottom middle: The sign structure of the second eigenvector allows assignment to metastable states. Bottom right: The matrix permuted according to the eigenvector structure exhibits a block structure. Top right: Aggregating the discretization boxes belonging to the same metastable state yields a two state model.

9.6.3 The hidden Markov model approach

Assume that we extracted a time series Y_t from, e.g., MD-simulation, which do not necessarily completely specify the state of the molecule at time t, but rather some low-dimensional observable, for example, some or all torsion angles or a set of essential degrees of freedom. As the Markov property does not hold for projections of Markov processes in general, we have to be aware that the process on the (torsion angles) subspace might no longer be Markovian. Nevertheless, we assume that there is an unknown metastable decomposition into m sets $D_1, \ldots, D_m$, in the full dimensional system. We then can premise that, at any time t, the system is in one of the metastable states D_{j_t} to which we simply refer by j_t in the following. However, the time series (j_t) is hidden, i.e., neither known in advance nor observed, while the series (Y_t) is called the output series or the observed sequence.

This scenario can be represented by a Hidden Markov Model (HMM). A HMM abstractly consists of two related stochastic processes: a hidden process j_t, that fulfills the Markov property, and an observed process Y_t, that depends

on the state of the hidden process j_t at time t. A HMM is fully specified by the initial distribution π, the transition matrix P of the hidden Markov process j_t, a rate matrix in continuous time, and the probability distributions that govern the observable Y_t depending on the respective hidden state j_t.

In the standard versions of HMMs the observables are assumed to be identically and independent distributed (i.i.d.) random variables with stationary distributions that depend on the respective hidden states [161]. Within the scope of molecular dynamics this setting corresponds to the simple case where the (sampling) time lag τ is comparable with the relaxation times within the metastable states, while being are sufficiently smaller than the mean exit times of the metastable states. In other words one expects the process to sample the restricted invariant density before exiting from a metastable state, and the sampling time of the time series is long enough to assume statistical independence between steps. Nevertheless, if this is not the case, only a slight modification of the model structure is required to include the relaxation behavior: Instead of i.i.d. random variables, an Ornstein-Uhlenbeck (OU) process serves as a model for the output behavior in each hidden state. The HMM then takes the form [162]:

$$\dot{Y}_t = -\nabla V^{(j_t)}(Y_t) + \sigma^{(j_t)}\dot{W}_t, \tag{9.12}$$

$$j_t \,:\, \mathbf{R}^1 \to \{1, 2, \ldots, m\}, \tag{9.13}$$

where j_t are the realizations of the hidden Markov process with discrete state space, W_t is standard "white noise", and $\sigma^{(j)}$ the state dependent diffusion matrix. $V^{(j)}$ is assumed of the form

$$V^{(j)}(Y) = \frac{1}{2}(Y - \mu^{(j)})^T D^{(j)}(Y - \mu^{(j)}) + V_0^{(j)}, \tag{9.14}$$

i.e., to be harmonic potentials with $\mu^{(j)}$ and $D^{(j)}$ denoting equilibrium position and Hesse-matrix of the OU process within conformation j. This process is therefore specified by the parameters $\Theta^{(j)} = (\mu^{(j)}, D^{(j)}, \sigma^{(j)})$. Since the output process is given by a stochastic differential equation we will refer to this model modification as HmmSde. Its entire parameter set is $\Theta = (\Theta^{(1)}, \ldots, \Theta^{(m)}, P)$, where P denotes the transition matrix of the Markov chain in (9.13).

The parameter set of this model can be estimated from a time series via a modified EM (expectation-maximation) algorithm [172], as described in [162, 163, 173]. Once the model parameters are estimated one can use the Viterbi algorithm [174] to compute the most probable path of hidden states, the Viterbi path, given an observation sequence. So both can be obtained, a dynamical model and the assignment of data points to the hidden, not observed, states. In contrast to the transfer operator approach, where the number of metastable states is extracted from the spectral properties of the transition matrix, we have to specify the number of metastable states as an input parameter for the EM algorithm. Since this number is in general unknown, a combination of both algorithms is used: First, guess a sufficiently

large number of metastable sets, compute a Viterbi path and, second, reduce the number of states by set up a transition matrix from the (discrete) Viterbi path and cluster with the transfer operator approach.

9.6.4 Conformation analysis of a glycine dipeptide analogue (GLDA)

As an example we investigate the dynamics of glycine dipeptide analogue (CH_3–CO–NH–CH_2–CO–NH–CH_3), which is one of the smallest (artificial) peptides containing two peptide bonds (CO–NH). Thus the essential degrees of freedom are the torsional rotations of the individual peptide units (–CO–NH–) about the backbone of the chain, where Φ and Ψ describe the torsion of the N-terminus (CH_3–CO–NH–) and the C-terminus (–CO–NH–CH_3), respectively, with regard to the central CH_2 group, see Fig. 9.37. The plane spanned by the two angles Φ, Ψ is referred to as Ramachandran plane [175], with values of $(\pm 180°, \pm 180°)$ corresponding to a fully extended conformation of the chain. For longer polypeptide chains these angles serve to characterize typical secondary structural motifs such as helices and sheets.

9.6.4.1 GLDA in the gas phase

We used an empirical force field (Gromos 53a6 [176,177]) to obtain a potential energy surface in the two essential degrees, i.e., varying the Ramachandran angles and minimizing the potential energy wrt. the other degrees of freedom.

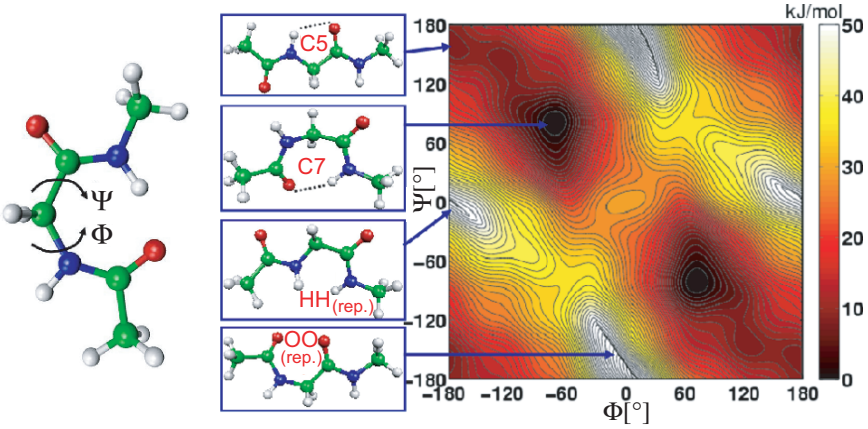

Fig. 9.37. Left: Glycine dipeptide analogue. The two marked torsion angles are the essential degrees of freedom as the peptide units are essentially planar. Right: Potential energy surface with respect to the two torsion angles. The local minima are due to the formation of hydrogen bonds between the peptide groups, the local maxima are due to repulsion.

The potential energy surface shown in Fig. 9.37, reflects the symmetry of the peptide. Local minima correspond to energetically favorable formations of ringlike structures, including seven or five atoms (C5 and C7), closed by (strongly) frustrated intramolecular hydrogen bonds. The maximal regions are corresponding to intramolecular repulsion of $-O\ O-$ and $-H\ H-$. The accuracy of the potential energy surface is of course limited by the quality of the empirical force field used, but comparison with the potential energy surface computed by quantum chemical calculations yields a qualitatively similar picture [178–182].

Performing a finite temperature MD-simulation at 300K using a Berendsen thermostat of the dipeptide in vacuum, samples the low energy regions of C5 and C7 in the Ramachandran plane, see Fig 9.38E. As these regions are separated by a barrier of approx. 9 kJ/mol one would expect a metastable behavior at a reasonable timescale. To confirm this assumption, we use HMMSDE to extract a Viterbi path, assuming 4 (hidden) states, for each of the Ramachan-

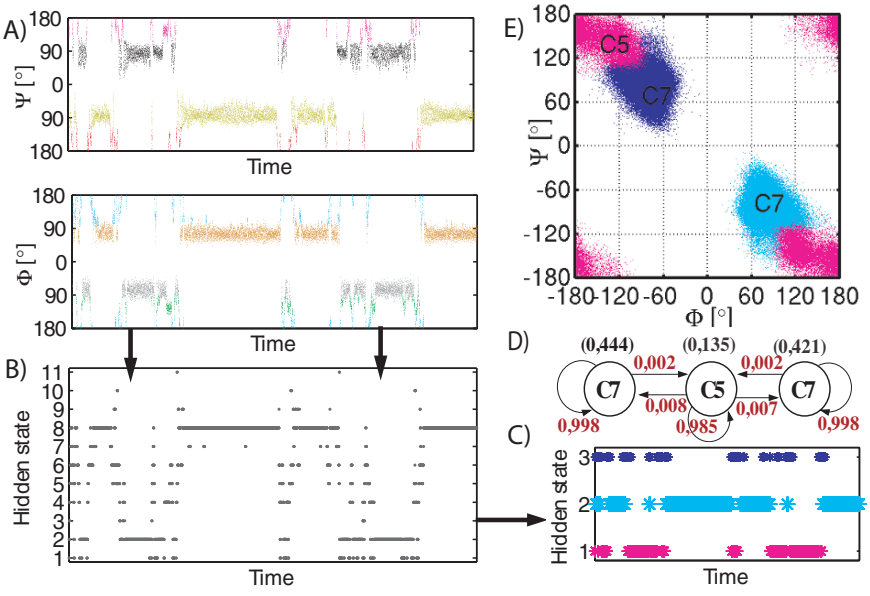

Fig. 9.38. A) A sample of the two dimensional torsion angle time series extracted from a 300K MD-simulation. The data points are colored according to the allocation to hidden states by HMM-SDE. B) Superposition of the two Viterbi paths yields into a joint Viterbi path with 11 hidden states. C) Using the transfer operator approach lumps the 11 hidden states to 3 metastable hidden states. D) A transition network for the 3 hidden states with a time lag of $\tau = 0.1ps$, red numbers denote the conditional transition probabilities, numbers in brackets the weight of each state. E) The data points of the torsion angle time series in the Ramachandran plane colored according to their allocation to metastable states.

dran angles Φ, Ψ. Superposition of these two Viterbi paths yields a Viterbi path with 11 states. As the number of hidden states is only determined by our initial guess, we use the transfer operator approach to further reduce the number of states. Setting up the stochastic transition matrix P with time lag $\tau = 0.1ps$, and computing the first five eigenvalues:

$$\sigma(P) = \{1, 0.9948, 0.9296, 0.8152, 0.6540 \ldots\},$$

indicates 3 metastable sets. Using the information coded in the three dominant eigenvectors we aggregate the 11 states to 3 states. In Fig. 9.38E the assignment of the data points to these metastable (hidden) states is shown, the plot reveals, that we identified the (symmetric) C7 conformations and the C5 conformation. Transition probabilities between these hidden states can be obtained by using (9.11), Fig. 9.38D. Thus we have obtained a detailed dynamical picture of the effective finite temperature dynamics of GLDA in vacuum.

9.6.4.2 GLDA in aqueous solution

To compare these results with the dynamics in solution phase we consider GLDA in a $(3.5\text{nm})^3$ box filled with 1405 rigid water molecules. Using a cutoff for electrostatic interactions of 1.1 nm and a Berendsen-temperature coupling to the solvent of 300K, we performed an MD-simulation over 2.5 ns with an integration timestep of 2 fs using again the Gromos 53a6 force field and recording the atom positions every 20 fs. After discretizing the Ramachandran plane in $5^\circ \times 5^\circ$ boxes, the free energy for each box B_i can be calculated by [183, 184]

$$\Delta G(B_i) = -k_B T(\log(\mathbb{P}[B_i]) - \log(\max_i \mathbb{P}[B_i])).$$

This free energy surface, see Fig. 9.39, has, due to intermolecular interactions (water-GLDA), a considerably richer structure than the potential energy surface in gas phase, Fig. 9.37. Analyzing the torsion angle time series with the HmmSde approach, assuming 24 metastable sets, perfectly distinguishes regions belonging to different local minima in the free energy surface, Fig. 9.39. As these local minima are separated by low energy barriers, compared with thermally available energies, it is not a priori clear that they correspond to metastable states on timescales of e.g. 1 ps. An instructive picture is obtained by setting up the transition matrix, based on the 24 states of the obtained Viterbi path, and plotting the eigenvalues against the time lag used, Fig. 9.40. It can be clearly seen that 4 metastable states are persistent even for larger time lags, as there is an obvious gap after the first 4 eigenvalues.

The cause of the metastable states can be revealed by taking the intermolecular interactions into account. These interactions are mainly due to H-bond bridges between the peptide groups (–CO–NH–) and neighboring water molecules. Each peptide group provides a donor pair (NH) and an acceptor (O) for

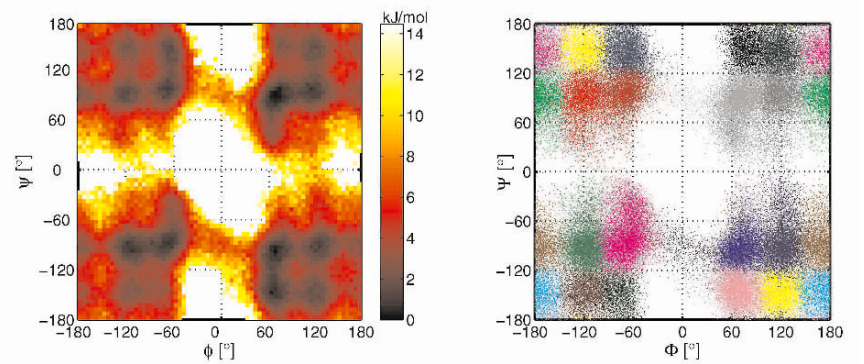

Fig. 9.39. Left: The free energy surface obtained from MD-Simulation with water has a considerably richer structure than the potential energy surface in vacuum. Right: Coloring the data points according to state allocation obtained by HmmSde perfectly distinguishes the local minima in the free energy surface (for 24 metastable sets assumed).

H-bond bridges attracting solvent molecules. If we restrict to microsolvation structures, i.e. GLDA with 1 or 2 waters, it is clear that ring like structures, as shown in Fig. 9.41, are energetically favorable, as each water molecule can participate in two H-bond bridges [185]. Besides the possible extension of the C7 and C5 structure to C7+2 (atoms), C7+2+2, C5+2 and C5+2+2 structures, H-bond bridges can stabilize structures that do not occur in vacuum, namely the C6 structures shown, where the –O O– and –H H– repulsion is overcome by inserting water molecules to form a ring structure. In the following we denote by C7+X the C7+2+2 and C7+2 structures collectively (with analogous meaning of C6+X and C5+X).

These microsolvation ring structures can also be identified in the fully solvated system. Comparison of the plots in Fig. 9.40 reveals the nature of the four metastable states. They correspond to regions where C7+X/C5+X or C6+X ring structures occur.

The assumption that microsolvation structures cause metastability can be further supported by redoing the analysis based on six metastable states, see Fig. 9.42. Even though there are regions in the Ramachandran plane allowing different microsolvation structures, e.g. regions allowing C7+X or C5+X structures have an overlap, the plots of the data points belonging to a metastable state and the plots of data points with certain microsolvation structures show an obvious similarity. Again, this indicates that the origin of the metastable conformational structures is related to the formation of different microsolvation environments of the solute molecule.

In conclusion, we demonstrated the ability of the HmmSde approach to reflect structural properties of the complete simulated system by analysis of only two essential degrees of freedom. The effective reduction of dimension-

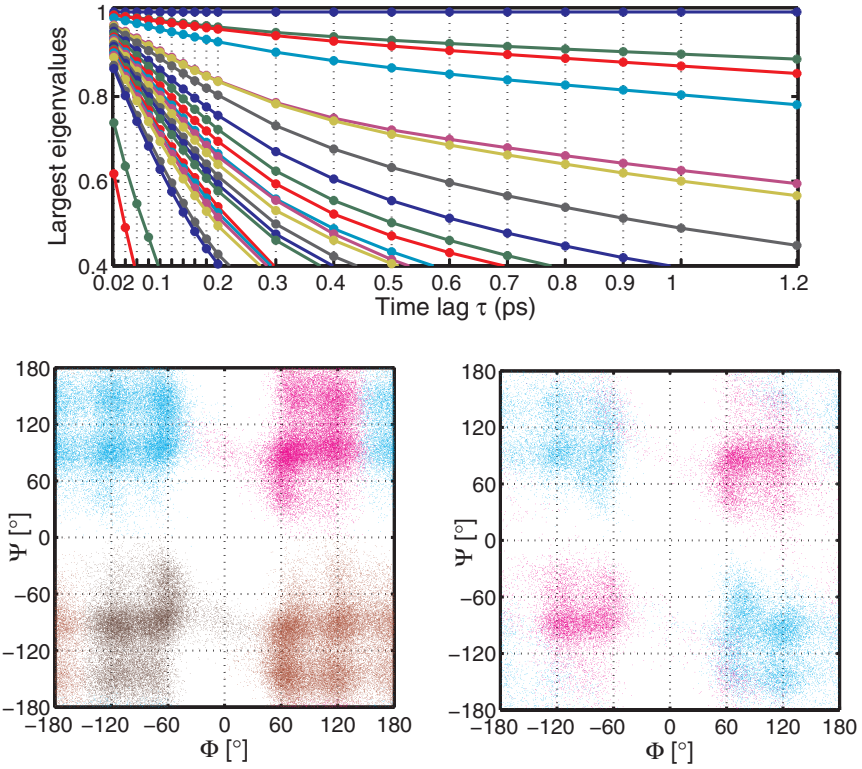

Fig. 9.40. Left: Dependence of the eigenvalues of the transition matrix obtained from the Viterbi path on different time lags. Middle: Data points are colored according to a clustering of the Viterbi path in 4 metastable sets. Right: Data points exhibiting a C6 microsolvation structure (magenta) and data points exhibiting a C7 or C5 microsolvation structure (cyan).

ality achieved for the GLDA example is due to the capability of HmmSde to distinguish different dynamical behavior in time series. Although the system investigated here is of moderate size, HmmSde appears to be a promising approach to beat the curse of dimensionality in more complex systems. Currently conformational analysis of DNA fragments containing 15 base pairs has been pursued in our laboratory [173]. Hence, it is believed that this approach is much more general and can be used beyond the context of MD-simulations. Possible applications range, e.g., from transient spectroscopy to the analysis of climate or financial data.

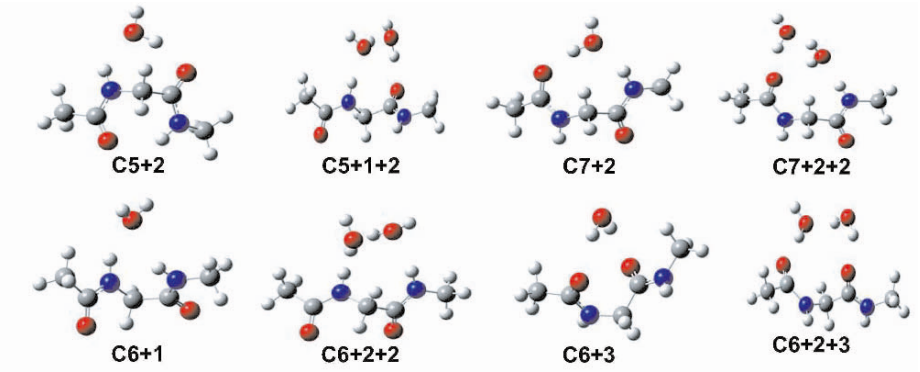

Fig. 9.41. Energetically favorable microsolvation structures with one or two water molecules.

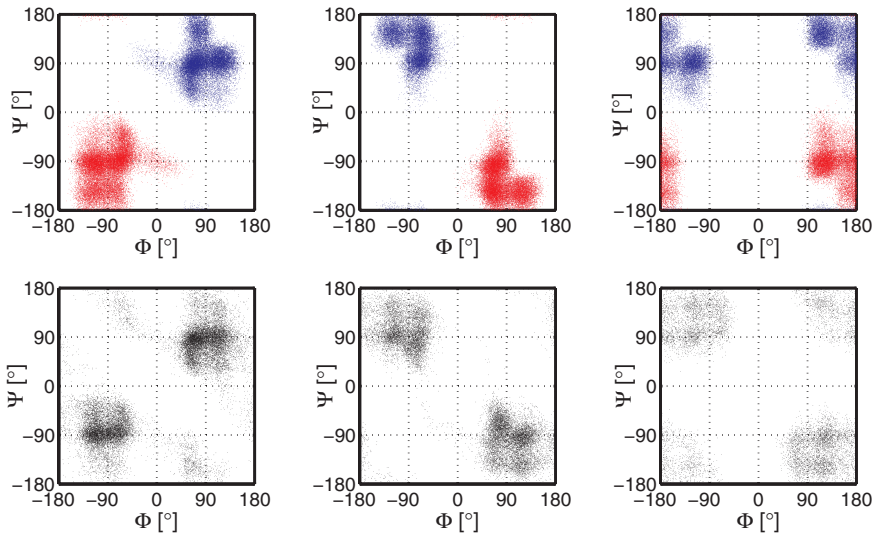

Fig. 9.42. *Top:* Data points belonging to different metastable states after clustering in 6 states, two symmetric equivalent states are shown in one plot. *Bottom:* Data points exhibiting C6+X (left), C7+X (middle) or C5+X (right) ring structures.

9.7 Detection and identification of bacteria in air using femtosecond spectroscopy

J.-P. Wolf

Rapid detection and identification of pathogenic aerosols such as *Bacillus anthracis* (anthrax) and *variola major* (smallpox) from potential bioterrorism release, as well as infectious diseases such as severe acute respiratory syndrome (SARS) or legionellosis, are urgent safety issues. However, in order to efficiently protect populations from bioterrorism in public locations or to prevent nosocomial infections in hospitals (e.g. Methicillin resistant *Staphylococcus aureus*) or epidemic spread, bioaerosol detectors need to be very fast (typ. minutes) and very selective (to discriminate pathogen from nonpathogen particles and minimize false alarm rates). Unfortunately such detectors are today sorely lacking.

One can roughly distinguish two research tracks that were followed these latter years in order to reach this important but difficult objective: [186] biochemical identification procedures, which are selective but slow, and [187] optical devices, which are fast but not specific enough.

The currently available biochemical techniques, such as polymerase chain reaction (PCR) [186–189], fluorescence in situ hybridization (FISH) [186,187, 190], antibiotic resistance determination [191,192], or chip matrix of biochemical microsensors [193,194], can identify the genus and species of the bacteria or virus. However, after the alarm has sounded, these biochemical assay procedures require time (many hours or even days). Even the recently developed ultrafast B cell adaptive immune-based sensor [195] and real-time PCR [188] will require more than an hour [195] for the total assay.

Several groups have developed sophisticated optical systems to distinguish bioaerosols from nonbioaerosols based on fluorescence [196–199] and/or elastic scattering [200,201]. The most advanced experiments address each individual aerosol particle, which is spectrally analyzed [196,202,203]. These instruments can run continuously, in-situ, and in real-time to provide rapid warning/alarm for the existence of a few potentially life threatening bio-aerosols in the midst of a vast number of nonbio-aerosols. The major flaw inherent in these instruments is frequent false alarms because the UV-Visible fluorescence systems are incapable of distinguishing different molecules with similar fluorescence peaks (such as tryptophan and diesel particles or cigarette smoke) [202, 204]. Fig 9.43 shows, as an example, the similitude in the fluorescence spectra of diesel fuel, tryptophan and *Bacillus subtilis*, which is a biosimulant for *Bacillus anthracis*. It is even more elusive using LIF to expect identifying different kinds of harmless from pathogen microorganisms. In this latter case, extensive studies based on principle components analysis of the excitation vs fluorescence spectral matrix have been performed to distinguish the spectrum from one type of bacteria from another, without success [205].

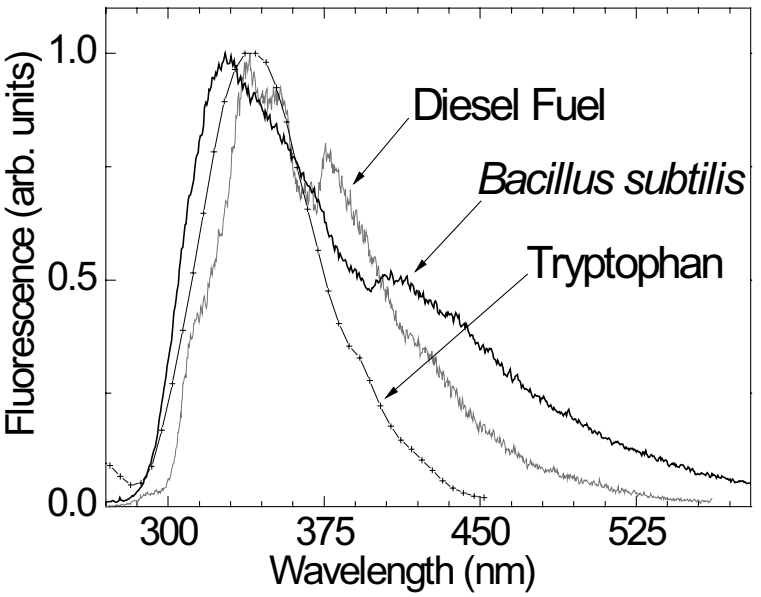

Fig. 9.43. Comparison of the fluorescence spectra of Tryptophan, *B. Subtilis* and Diesel fuel.

However, an attractive capability of optical techniques is remote sensing, and especially Lidar (Light Detection and Ranging). The Lidar technique [206] allows mapping aerosols in 3D over several kilometers, similar to an optical Radar. It might be able to detect the release and spread of potentially harmful plumes (such as bioterrorism release or legionella from industrial cooling towers) at large distance and then provide time to take the necessary measures to protect populations or identify sources. So far, Lidar detection of bioaerosols has been demonstrated either using elastic scattering [206] or LIF [206, 207]. However, the distinction between bioaerosols and nonbio-aerosols was either impossible (elastic scattering only) or very unsatisfactory for LIF-Lidars (for the same reason as point monitors, e.g. interference with pollens and organic particles like traffic related soot or polycyclic aromatic hydrocarbons (PAHs)).

To overcome these difficulties, there is an interest in exciting the fluorescence with ultrafast laser pulses in order to access specific molecular dynamical features. Recent experiments using coherent control and multiphoton ultrafast spectroscopy have shown the ability of discriminating between molecular species that have similar one-photon absorption and emission spectra [208, 209]. Two-photon excited fluorescence (2PEF) and pulse shaping

techniques should allow for selective enhancement of the fluorescence of one molecule versus another that has similar spectra. Optimal dynamic discrimination (ODD) [210] of similar molecular agent provides the basis for generating optimal signals for detection.

9.7.1 Multiphoton excited fluorescence (MPEF) and multiphoton ionization (MPI) in aerosol microparticles

Femtosecond laser pulses provide very high pulse intensity at low energy, which allows inducing nonlinear processes in particles without deformation due to electrostrictive and thermal expansion effects.

The most prominent feature of nonlinear processes in aerosol particles is strong localization of the emitting molecules within the particle, and subsequent backward enhancement of the emitted light [211, 212]. This unexpected behavior is extremely attractive for remote detection schemes, such as Lidar applications. Localization is achieved by the nonlinear processes, which typically involve the n-th power of the internal intensity $\mathrm{I}^n(\mathrm{r})$ (r for position inside the particle). The backward enhancement can be explained by the reciprocity (or time reversal) principle: Re-emission from regions with high $\mathrm{I}^n(\mathrm{r})$ tends to return toward the illuminating source by essentially retracing the direction of the incident beam that gave rise to the focal points. This backward enhancement has been observed for both spherical and non spherical [213] microparticles. More precisely, we investigated, both theoretically and experimentally, incoherent multiphoton processes involving $n = 1$ to 5 photons [212]. For $n = 1$, 2, 3, MPEF occurs in bioaerosols because of natural fluorophors such as amino acids (tryptophan, tyrosin), NADH (nicotinamide adenine dinucleotide), and flavins. Figure 9.44 shows the LIF spectra of various bacteria, and the contribution of each fluorophor in the fluorescence spectrum under 266 nm excitation. The strongly anisotropic MPEF emission was demonstrated on individual microdroplets containing tryptophan, riboflavin, or other synthetic fluorophors [211–213]. The experiment was performed such that each individual microparticle was hit by a single laser shot. The aerosol source was based on a piezo driven nozzle, which precisely controlled the time of ejection of the microparticles. Figure 9.45 shows the MPEF angular distribution and the comparison between experimental and theoretical (Lorentz-Mie calculations) results for the one- (400 nm) (Fig. 9.45a), two- (800 nm) (Fig. 9.45b) and three-photon ($1, 2\mu m$) (Fig. 9.45c) excitation process. They show that the fluorescence emission is maximum in the direction toward the exciting source. The directionality of the emission is dependent on the increase of n, because the excitation process involves the nth power of the intensity $\mathrm{I}^n(\mathrm{r})$. The ratio $\mathrm{Rf} = \mathrm{P}(180°)/\mathrm{P}(90°)$ increases from 1.8 to 9 when n changes from 1 to 3 (P is the emitted light power). For 3PEF, fluorescence from aerosol microparticles is therefore mainly backwards emitted, which is ideal for Lidar experiments. For $n = 5$ photons we investigated laser induced breakdown (LIBS) in water microdroplets, initiated by multiphoton ionization. The ionization potential

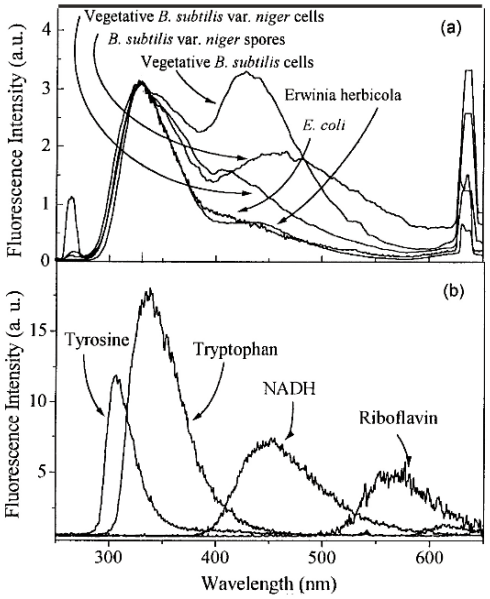

Fig. 9.44. Fluorescence spectra of bacteria and respective contributions of amino acids, NADH and flavins [202].

of water molecules is E_{ion}=6.5 eV, so that 5 photons are required at a laser wavelength of 800 nm to initiate the process of plasma formation. The growth of the plasma is also a nonlinear function of $I^n(r)$. We showed that both localization and backward enhancement strongly increases with the order n of the multiphoton process, exceeding $Rf = U(180°)/U(90°) = 35$ for $n = 5$ [214]. As for MPEF, LIBS has the potential of providing information about the aerosols composition.

9.7.2 MPEF-Lidar detection of biological aerosols

The first multiphoton excited fluorescence Lidar detection of biological aerosols was performed using the Teramobile system. The Teramobile (www.teramobile.org) is the first femtosecond-terawatt laser based Lidar [215], and was developed by a French-German consortium, formed by the Universities of Jena, Berlin, Lyon, and the Ecole Polytechnique (Palaiseau).

The bioaerosol particles, consisting of 1 μm size water droplets containing 0.03 g/l Riboflavin (typical for bacteria), were generated at a distance of 50 m from the Teramobile system. Riboflavin was excited by two photons at 800 nm and emitted a broad fluorescence around 540 nm. This experiment [215, 216] is the first demonstration of the remote detection of bioaerosols using a 2PEF-femtosecond Lidar. The broad fluorescence signature is clearly

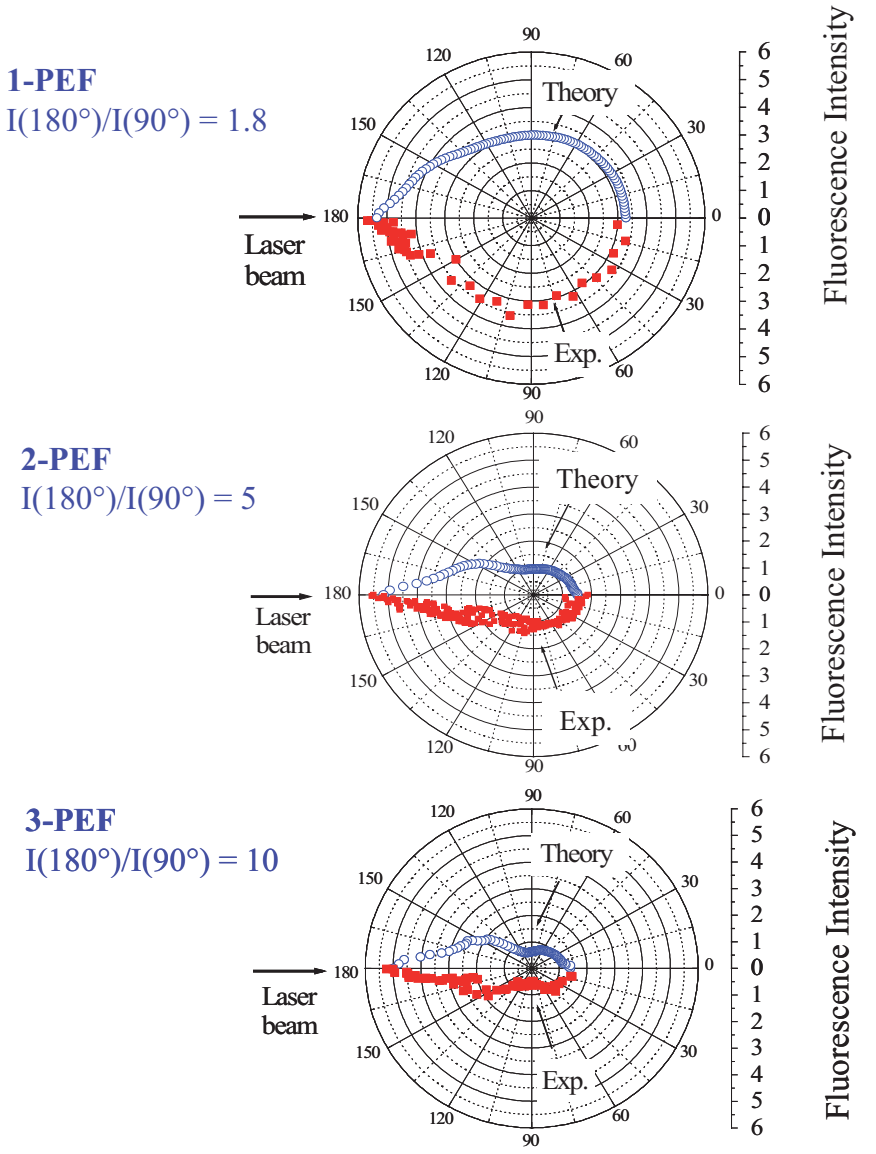

Fig. 9.45. Backward enhancement of the fluorescence from aerosol microparticles in the case of nonlinear excitation (MPEF) [211].

observed from the particle cloud (typ. $10^4 p/cm^3$), with a range resolution of a few meters (Fig. 9.46). As a comparison, droplets of pure water do not exhibit any parasitic fluorescence in this spectral range. However, a background is observed for both types of particles, arising from the scattering of white light generated by filaments in air.

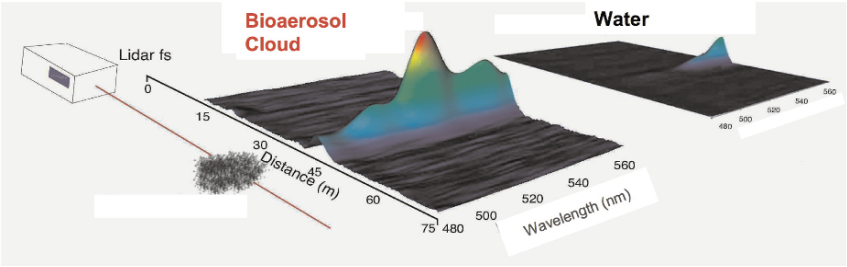

Fig. 9.46. Two-photon excited fluorescence (2PEF)-Lidar detection of bioaerosols [215, 216].

Primarily, MPEF might be advantageous as compared to linear LIF for the following reasons: (1) MPEF is enhanced in the backward direction and (2) the transmission of the atmosphere is much higher for longer wavelengths. For example, if we consider the detection of tryptophan (another typical biotracer that can be excited with 3 photons of 810 nm), the transmission of the atmosphere is typically 0.6 km^{-1} at 270 nm, whereas it is $3 \cdot 10^{-3}$ km^{-1} at 810 nm (for a clear atmosphere, depending on the background ozone concentration). This compensates the lower 3-PEF cross-section compared to the 1-PEF cross-section at distances larger than a couple of kilometers. The most attractive feature of MPEF is, however, the possibility of using pump-probe techniques, as described hereafter in order to discriminate bioaerosols from background interferents such as traffic related soot or PAHs.

9.7.3 Pump-probe spectroscopy to distinguish bioaerosols from background organic particles in air

As mentioned before, a major drawback inherent in LIF instruments is the frequency of false identification because UV-Vis fluorescence is incapable of discriminating different molecules with similar absorption and fluorescence signatures. While mineral and carbon black particles do not have strong fluorescence signals, aromatics and polycyclic aromatic hydrocarbons (PAH) from organic particles and Diesel soot strongly interfere with biological fluorophors such as amino acids [202, 204]. The similarity between the spectral signatures of organic and biological molecules under UV-Vis excitation lies in the fact that similar π-electrons from carbonic rings are involved. Therefore, aromatics or PAHs (such as naphthalene) exhibit absorption and emission bands similar to those of amino acids like Tyrosine or Trp. Some shifts are present because of differences in specific bonds and the number of aromatic rings, but the broad featureless nature of the bands renders them almost indistinguishable. Moreover, the different environments of Trp in bacteria (e.g., they are contained

in many proteins) and the mixtures of PAHs in transportation generated particles, blur their signatures. As shown before in Fig. 9.43, the fluorescence spectra (resulting from excitation at 270 nm) of Trp, *Bacillus Subtilis* and Diesel fuel are almost identical.

A novel femtosecond pump-probe depletion (PPD) concept was recently developed [217], based on the time-resolved observation of the competition between excited state absorption (ESA) into a higher lying excited state and fluorescence into the ground state. This approach makes use of two physical processes beyond that available in the usual fluorescence spectrum: (1) the dynamics in the intermediate pumped state and (2) the coupling efficiency to a higher lying excited state. More precisely, as shown in Fig. 9.47, a femtosecond pump pulse (τ=120fs) at 270 nm transfers a portion of the ground state S_0 population of Trp to its $S_1(\{v'\})$ excited state (corresponding to a set of vibronic levels, *i.e.*, $\{v'\}$). The vibronic excitation relaxes by internal energy redistribution to lower $\{v'\}$ modes, associated with charge transfer processes (CT), conformational relaxation, and intersystem crossing with repulsive $\pi\sigma*$ states [218]. After vibronic energy redistribution, fluorescence is emitted from $S_1(\{v'\})$ within a lifetime of 2.6 ns. By illuminating the amino acid with a

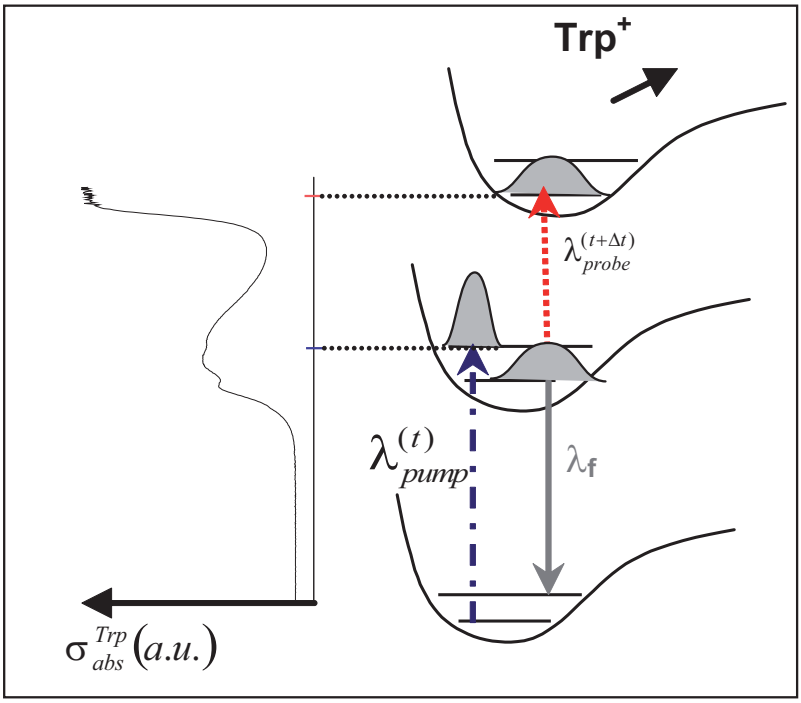

Fig. 9.47. Femtosecond pump-probe depletion (PPD) technique to distinguish biomolecules from organic interferents.

second pulse (probe) at 800 nm after a certain time delay from the pump pulse, the S_1 population is decreased and the fluorescence depleted. The 800 nm femtosecond laser pulse induces a transition from S_1 to an ensemble of higher lying S_n states, which are likely to be autoionizing [219], but also undergo radiationless relaxation into S_0 [220]. By varying the temporal delay between the pump and probe, the dynamics of the internal energy redistribution within the intermediate excited potential surface S_1 is explored. In principle, as different species have distinct S_1 surfaces, discriminating signals can be enhanced in this fashion.

Figure 9.48 shows the pump-probe depletion dynamics of the S_1 state in Trp as compared to a circulation of Diesel fuel and Naphthalene in cyclohexane, one of the most abundant fluorescing PAHs in Diesel. While depletion reaches as much as 50% in Trp for an optimum delay of $\Delta t = 2$ ps, Diesel fuel and Naphthalene appear almost unaffected (within a few percent), at least on these timescales. This remarkable difference allows for efficient discrimination between Trp and organic species, although they exhibit very similar linear

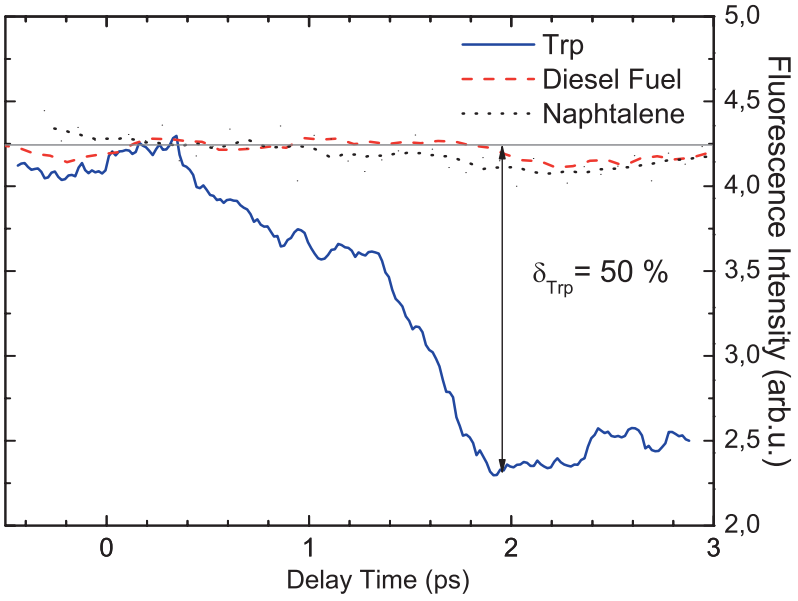

Fig. 9.48. Femtosecond pump-probe depletion PPD applied to the distinction of Trp from traffic related PAH's [217].

excitation/fluorescence spectra (Fig. 9.43). Two reasons might be invoked to understand this difference: (1) the intermediate state dynamics is predominantly influenced by the NH- and CO- groups of the amino acid backbone and (2) the ionization potential and other excited states are higher for the PAHs contained in Diesel than for Trp by about 1 eV so that excitation induced by the probe laser is much less likely in the organic compounds. The particular dynamics of the internal energy redistribution in the S_1 state of Trp (Fig. 9.48), and in particular the time needed to start efficient depletion, is not fully interpreted as yet. Further electronic structure calculations are required to better understand the process, especially on the higher lying S_n potential surfaces.

In order to more closely approach the application of detecting and discriminating bioagents from organic particles in air, we repeated the experiment with bacteria, including *Escherichia coli*, *Enterococcus* and *Bacillus subtilis* (BG). Artefacts due to preparation methods have been avoided by using a variety of samples, i.e. lyophilized cells and spores, suspended either in pure or in biologically buffered water (i.e. typically $10^7 - 10^9$ bacteria per cc). The observed pump-probe depletion results are remarkably robust (Fig. 9.49), with similar depletion values for all the considered bacteria (results for Enterococcus, not shown in the figure, are identical), although the Trp microenvironment within the bacteria proteins is very different from water. These unique features can be used for a novel selective bioaerosol detection technique that avoids interference from background traffic related organic particles in the air: The excitation shall consist of a pump-probe sequence with the optimum delay $\Delta t = 2$ps, and the fluorescence emitted by the mixture will be measured as the probe laser is alternately switched on and off. This pump-probe two-photon differential fluorescence method will be especially attractive for an active remote detection technique such as MPEF-Lidar, where the lack of discrimination between bioaerosols and transportation related organics is currently most acute.

These results, based on very simple pump-probe schemes, are very encouraging and open new perspectives in the discrimination capability of bioaerosols in air. We intend to extend the technique by applying more sophisticated excitation schemes (e.g., optimally shaped pulses), related to coherent control, in order to better distinguish bioaerosols from non-bioaerosols, but also to gain selectivity among the bacteria themselves. Theoretical calculations were recently performed, which show that under some conditions, optimal dynamic discrimination (ODD) can lead to efficient distinction between 3 species that exhibit almost the same spectral characteristics [210].

9.7.4 Toward LIBS identification of bacteria in air

As mentioned above, laser induced plasma line emission is also enhanced in the backward direction when microparticles are excited by a femtosecond laser. Although nanosecond-laser LIBS (nano-LIBS) has already been applied to the

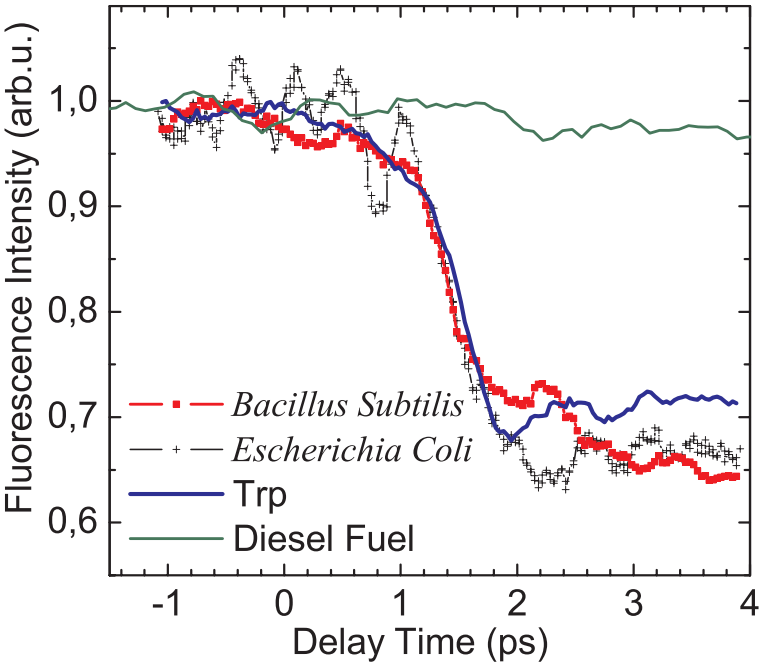

Fig. 9.49. Femtosecond pump-probe depletion of in vivo bacteria [217].

study of bacteria [221, 222], femtosecond lasers open new perspectives in this respect. The plasma temperature is, indeed, much lower in the case of femtosecond excitation, which strongly reduces the blackbody background and interfering lines from excited N_2 and O_2 from the air. This allows performing time gated detection with very short delays, and thus observing much richer and cleaner spectra from the biological sample. This crucial advantage is shown in Fig. 9.50, where the K line emitted by a sample of *Escherichia coli* is clearly detected in femto-LIBS and almost unobservable under ns-laser excitation [223]. Thanks to the low thermal background in fs-LIBS, 20-50 lines are recorded for each bacterial sample considered in the study (*Acinetobacter*, *Escherichia coli*, *Erwinia, Shewanella* and *Bacillus subtilis*) . A systematic sorting with sophisticated algorithms is in progress in order to evaluate whether the spectra are sufficiently different to unambiguously identify each species [224]. The results are already promising and we show (Fig. 9.51), as an example, the difference between *Escherichia coli* and *Bacillus subtilis* for the Li line intensity (also observed for the Ca line). This observation can be un-

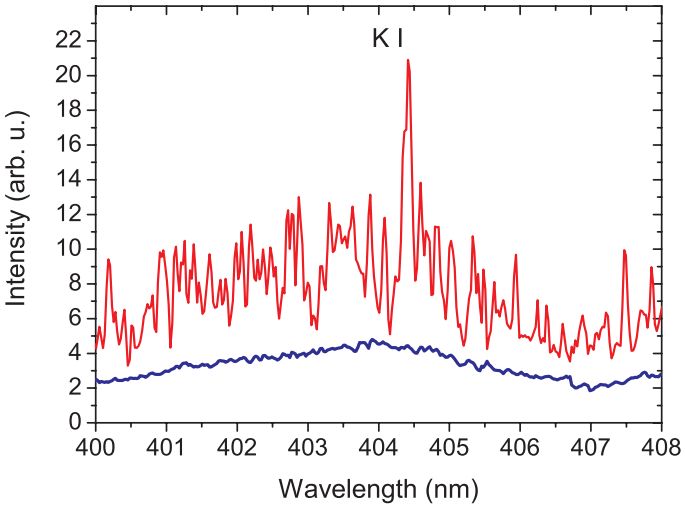

Fig. 9.50. Comparison of ns-LIBS (blue) and fs-LIBS (red) results on the K line (Kl) of *Escherichia coli* [224].

derstood by the typical difference of the cell wall structure between a Gram+ and a Gram- bacterium. The ratio of these lines as compared to Na for example constitutes an "all optical Gram test". Low temperature plasma is not the only advantage of fs-LIBS: the ablation process itself seems different. fs-LIBS acts more as a direct bond-breaking and evaporation process instead of thermal vaporization. This particular ablation process could be put into evidence as not only atoms and ions lines were observed but also molecular signatures such as CN or C_2 [225]. It was shown in particular that these molecular species are directly ablated from the sample, and not created by recombination of C atoms or ions with Nitrogen from the air (which occurs for ns excitation). Obtaining molecular signatures in addition to trace elements is a significant improvement of the method. The presence of CN molecules is, for instance, a good indicator for a biological material.

In conclusion, femtosecond spectroscopy opens new ways for the optical detection and identification of bioaerosols in air. Its unique capability of distinguishing molecules that exhibit almost identical absorption and fluorescence signatures is a key feature for identifying bacteria in a background of urban aerosols. The technique can also be applied for the remote detection of the microorganisms, if a nonlinear Lidar based configuration is chosen, as for the Teramobile. A more difficult task will be the distinction of one bacteria species from another, and in particular the identification of pathogen from

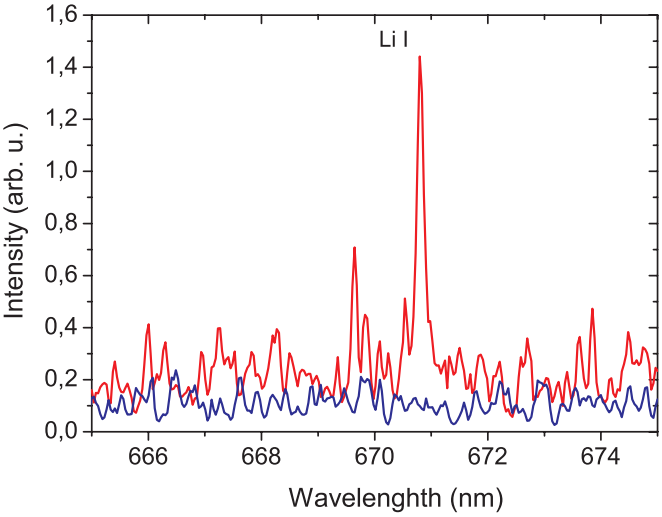

Fig. 9.51. Distinction of *Escherichia coli* (blue) from *Bacillus subtilis* (red) through their different Li-line emission (Li l) [224].

nonpathogen bioaerosols. A possible way to reach this difficult goal might be ODD. Another option could be provided by LIBS, as the wealth of emission lines under femtosecond excitation might allow to target some biological process that is characteristic from one type of bacteria. Moreover, it was recently demonstrated that LIBS could also be performed with a femtosecond-Lidar [226] and thus allow remote identification of particles in air.

9.8 Outlook

The investigation of biological systems with laser spectroscopic techniques remains a vibrant field. In particular, the strength of femtosecond spectroscopy for characterization of key reactive events and relaxation pathways, and identification of important inter- and intramolecular interactions has been illustrated in this chapter. Another avenue of growing importance is the use of femtosecond laser spectroscopies to obtain structure information in real-time on changes induced by optical excitation. For example, the monitoring of time-dependent absorption band shifts of tryptophan residues, induced by excitation of nearby bacteriorhodopsin was shown as a tool to this end. These experiments established the connection between translocation of charge [27] and the skeletal changes of the conjugate chain [23]. In addition, it also stressed the role of the dynamic electric force fields, which drive structural dynamics and govern enzymatic reactions. The capacity of infrared probing for determine the orientations of molecular electronic transition dipole moments within

the molecular frame was moreover demonstrated on anthracene-endoperoxide, and in combination with quantum mechanical calculations a definitive assignment of reactive electronic states could be made. For more complex biological systems and for tackling both the fast and the slower dynamics, Molecular Dynamics simulations, such as presented in Sect. 9.6, will prove to be a powerful tool for singling out crucial 3-dimensional conformations that can be connected to key events. Methods such as these, are expected to greatly contribute in the near future to enhancing our knowledge of 3-dimensional structural details in complex biological systems and their connection to the mechanisms that govern essential biological processes.

Insightful demonstrations were also presented of the use of creative multiple pulse manipulation schemes for separating overlapping spectral bands, manipulating excited and ground state populations, and knocking the investigated system out of equilibrium in biological systems of varying complexity, Sect. 9.3. These inherently multiphoton techniques can also be used to investigate excitation interactions in multichromophore systems [59, 60]. These new abilities allow significant new insights into fundamental biological events governing photosynthetic light harvesting [49,59,60,82], biological proton transfer reactions [69] and primary photoreception events [48, 48]. The fact that the control is achieved by manipulating electronic state populations allows the clear and concise interpretations of the experimental data.

On the theoretical front calculations of time-dependent wave packet propagations can provide information on time scales and branching ratios for competing reaction channels. These calculations also provide essential input for simulations based on a quantum dynamical Optimal Control Theory formulation, that can be used to predict the possibilities of experimentally manipulating the quantum yields of different reaction channels, or steering or even suppressing energy transfer and delocalization, by the use of shaped pulses. Input parameters for control possibilities are the amplitude (intensity), the phase, and the polarization of the different applied electromagnetic frequencies. We are only standing at the beginning of the tremendously exciting road of experimentally testing the possibilities optically altering the natural outcome biological processes.

Last but not least, femtosecond spectroscopy has led to new ways for outdoor detection and identification of airborne bioaerosols. The unique capability of distinguishing molecules with almost identical absorption and fluorescence signatures is a key feature for identifying bacteria in a background of urban aerosols, which will lead to clearly outlined applications.

The state-of-the-art achievements in laser technology, together with the continuously increasing computing power, due to the persisting validity of Moore's law, has clearly led to new spectroscopic and theoretical tools that continue to open up the possibilities of bringing the understanding of light-induced biological reactions to a higher levels.

Acknowledgments

I. Corral gratefully acknowledges La Fundación Ramón Areces for Financial Support and L. González the Berliner Förderprogram. The Teramobile project (www.teramobile.org) is funded by the Center National de la Recherche Scientifique (CNRS) and the Deutsche Forschungsgemeinschaft (DFG). J. P. Wolf gratefully acknowledges the members of the groups of R. Sauerbrey at the University Jena, A. Mysyrowicz at the ENSTA (Palaiseau). In particular, we wish to thank J. Kasparian, V. Boutou, F. Courvoisier, J. Yu, M. Baudelet, E. Salmon, D. Mondelain, G. Méjean, M. Rodriguez, H. Wille, S. Frey, R. Bourayou, and Y. B. Andre. The laboratory measurements on aerosols were performed in collaboration with the groups of R.K. Chang (Yale University), S.C. Hill (US Army Research Laboratories) and H. Rabitz (Princeton University). For these studies, RKC and JPW acknowledge NATO support SST-CLG977928.

The authors of Section 9.3 would like to thank colleagues that helped with this work including Luuk van Wilderen, Dr. Dorte Madsen, Dr. Ivo H.M. van Stokkum, Dr. Michael van der Horst. Results presented here were supported by the Netherlands Organization for Scientific Research (NWO) via the Dutch Foundation for Earth and Life Sciences (ALW) and the Stichting voor Fundamenteel Onderzoek der Materie, Netherlands (FOM). D.S.L. is grateful to the Human Frontier Science Program Organization for providing financial support with a long-term fellowship.

References

1. W. Behrens, U. Alexiev, R. Mollaaghababa, H.G. Khorana, M.P. Heyn, Biochem. **37**, 10411 (1998)
2. W. Behrens, (2004). Private communication
3. N. Grigorieff, T.A. Ceska, K.H. Downing, J.M. Baldwin, R. Henderson, J. Mol. Biol. **259**, 393 (1996)
4. P. Hamm, M. Zurek, T. Röschinger, H. Patzelt, D. Oesterhelt, Chem. Phys. Lett. **263**, 613 (1996)
5. L. Song, M.A. El-Sayed, J.K. Lanyi, Science **261**, 891 (1993)
6. K. Heyne, J. Herbst, B. Dominguez-Herradon, U. Alexiev, R. Diller, J. Phys. Chem. B **104**, 6053 (2000)
7. J. Herbst, K. Heyne, R. Diller, Science **297**, 822 (2002)
8. M.K. Johansson, H. Fidder, D. Dick, R.M. Cook, J. Am. Chem. Soc. **124**, 6950 (2002)
9. A. Warshel, Acc. Chem. Res. **14**, 284 (1981)
10. M.F. Perutz, Science **201**, 1187 (1978)
11. I. Gitlin, J.D. Carbeck, G.M. Whitesides, Angew. Chem. Int. Ed. **45**, 3022 (2006)
12. B.E. Cohen, T.B. McAnaney, E.S. Park, Y.N. Jan, S.G. Boxer, L.Y. Jan, Science **296**, 1700 (2002)

13. G.N. Phillips, M.L. Teodoro, T.S. Li, B. Smith, J.S. Olson, J. Phys. Chem. B **103**, 8817 (1999)
14. J.B. Jackson, A.R. Crofts, FEBS Letters **4**, 185 (1969)
15. J.L. Herek, T. Polivka, T. Pullerits, G.J. Fowler, C.N. Hunter, V. Sundström, Biochem. **37**, 7057 (1998)
16. R.A. Mathies, L. Stryer, Proc. Natl. Acad. Sci. **73**, 2169 (1976)
17. J. Huang, Z. Chen, A. Lewis, Phys. Chem. **93**, 3314 (1989)
18. D. Xu, C. Martin, K. Schulten, Biophys. J. **40**, 453 (1996)
19. J.T.M. Kennis, D.S. Larsen, K. Ohta, F.M. T, R.M. Glaeser, G.R. Fleming, J. Phys. Chem. B **106**, 6067 (2002)
20. A. Lewis, Proc. Natl. Acad. Sci. **75**, 549 (1978)
21. G. Wald, Science **162**, 230 (1968)
22. Q. Zhong, S. Ruhman, M. Ottolenghi, M. Sheves, N. Friedman, G.H. Atkinson, J. Delaney, J. Am. Chem. Soc. **118**, 12828 (1996)
23. T. Kobayashi, T. Saito, H. Ohtani, Nature **414**, 531 (2001)
24. D.W. McCamant, P. Kukura, R.A. Mathies, J. Phys. Chem. B **109**, 10449 (2005)
25. J. Dobler, W. Zinth, W. Kaiser, D. Oesterhelt, Chem. Phys. Lett **144**, 215 (1988)
26. S.J. Doig, P.J. Reid, R.A. Mathies, Phys. Chem **95**, 6372 (1991)
27. R. González-Luque, M. Garavelli, F. Bernardi, M. Merchán, M.A. Robb, M. Olivucci, Proc. Natl. Acad. Sci. **97**, 9379 (2000)
28. L. Salem, P. Bruckmann, Nature **258**, 526 (1975)
29. G.I. Groma, J. Hebling, C. Ludwig, J. Kuhl, Biophys. J. **69**, 2060 (1995)
30. J. Xu, A.B. Stickrath, P. Bhattacharya, J. Nees, G. Váró, J.R. Hillebrecht, L. Ren, R.R. Birge, Biophys. J. **85**, 1128 (2003)
31. G.I. Groma, A. Colonna, J.C. Lambry, J.W. Petrich, G. Váró, M. Joffre, M.H. Vos, J.L. Martin, Proc. Natl. Acad. Sci. **101**, 7971 (2004)
32. U. Zadok, A. Khatchatouriants, A. Lewis, M. Ottolenghi, M. Sheves, J. Am. Chem. Soc. **124**, 11844 (2002)
33. Y.R. Shen, *The principles of nonlinear optics* (Wiley-Interscience, Hoboken, N. J., 2003)
34. E. Pebay-Peyroula, G. Rummel, J.P. Rosenbusch, E.M. Landau, Science **277**, 1676 (1997)
35. H. Luecke, B. Schobert, H.T. Richter, J.P. Cartailler, J.K. Lanyi, J. Mol. Biol. **291**, 899 (1999)
36. P.R. Callis, Meth. Enzym. **278**, 113 (1997)
37. S. Schenkl, F. van Mourik, G. van der Zwan, S. Haacke, M. Chergui, Science **309**, 917 (2005)
38. S. Schenkl, F. van Mourik, N. Friedman, M. Sheves, R. Schlesinger, S. Haacke, M. Chergui, Proc. Nat. Acad. Sci. **103**, 4101 (2006)
39. M.R. Eftink, L.A. Selvige, P.R. Callis, A.A. Rehms, J. Phys. Chem. **94**, 3469 (1990)
40. M.L. Horng, J.A. Gardecki, A. Papazyan, M. Maroncelli, J. Phys. Chem. **99**, 17311 (1995)
41. B. Becher, F. Tokunaga, T.G. Ebrey, Biochem. **17**, 2293 (1978)
42. S. Georgakopoulou, R.N. Frese, E. Johnson, C. Koolhaas, R.J. Cogdell, R. van Grondelle, G. van der Zwan, Biophys. J. **82**, 2184 (2002)
43. Z.R. Grabowski, K. Rotkiewicz, W. Rettig, Chem. Rev. **103**, 3899 (2003)

44. W.M. Kwok, C. Ma, P. Matousek, A.W. Parker, D. Phillips, W.T. Toner, M. Towrie, S. Umapathy, J. Phys. Chem. A **105**, 984 (2001)
45. K. Nakanishi, V. Baloghnair, M. Arnaboldi, K. Tsujimoto, B. Honig, J. Am. Chem. Soc. **102**, 7945 (1980)
46. L.H. Andersen, I.B. Nielsen, M.B. Kristensen, M.O.A.E. Ghazaly, S. Haacke, M.B. Nielsen, M.A. Petersen, J. Am. Chem. Soc. **127**, 12347 (2005)
47. R. Jimenez, G.R. Fleming, *Ultrafast spectroscopy of photosynthetic systems, in Biophysical techniques in photosynthesis* (Kluwer Academic Publishers, Dordrecht, 1996)
48. D.S. Larsen, I.H.M. van Stokkum, M. Vengris, M.A. van der Horst, F.L. de Weerd, K.J. Hellingwerf, R. van Grondelle, Biophys. J. **87**, 1858 (2004)
49. D.S. Larsen, E. Papagiannakis, I.H.M. van Stokkum, M. Vengris, J.T.M. Kennis, R. van Grondelle, Chem. Phys. Lett. **381**, 733 (2003)
50. F. Gai, J.C. McDonald, P. Anfinrud, J. Am. Chem. Soc. **119**, 6201 (1997)
51. S. Ruhman, B. Hou, N. Freidman, M. Ottolenghi, M. Sheves, J. Am. Chem. Soc. **124**, 8854 (2002)
52. P. Changenet-Barret, C. Choma, E. Gooding, W. DeGrado, R.M. Hochstrasser, J. Phys. Chem. **104**, 9322 (2000)
53. S.A. Kovalenko, J. Ruthmann, N.P. Ernsting, J. Chem. Phys. **109**, 1894 (1998)
54. S.L. Logunov, V.V. Volkov, M. Braun, M.A. El-Sayed, Proc. Natl. Acad. Sci. **98**, 8475 (2001)
55. A.R. Holzwarth, *Data analysis in time-resolved measurements*, in *Biophysical techniques in photosynthesis* (Kluwer, Dordrecht, The Netherlands, 1996)
56. I.H.M. van Stokkum, D.S. Larsen, R. van Grondelle, Biochim. Biophys. Acta Bioenergetics **1657**, 82 (2004)
57. I.H.M. van Stokkum, D.S. Larsen, R. van Grondelle, Biochim. Biophys. Acta Bioenergetics **1658**, 262 (2004)
58. S.A. Rice, M. Zhao, *Optical control of molecular dynamics* (New York: Wiley Interscience, 2000)
59. E. Papagiannakis, I.H.M. van Stokkum, M. Vengris, R.J. Cogdell, R. van Grondelle, D.S. Larsen, J. Phys. Chem. B **110**, 5727 (2006)
60. E. Papagiannakis, M. Vengris, L. Valkunas, R.J. Cogdell, R. van Grondelle, D.S. Larsen, J. Phys. Chem. B **110**, 5737 (2006)
61. R.Y. Tsien, Ann. Rev. Biochem. **67**, 509 (1998)
62. M. Chattoraj, B.A. King, G.U. Bublitz, S.G. Boxer, Proc. Natl. Acad. Sci. **93**, 8362 (1996)
63. F. Yang, L. G, Moss, G.N. Phillips, Nat. Biotech. **14**, 1246 (1996)
64. T.M.H. Creemers, A.J. Lock, V. Subramaniam, T.M. Jovin, S. Volker, Nat. Struct. Biol. **6**, 557 (1999)
65. K. Brejc, T. Sixma, P. Kitts, S. Kain, R. Tsien, M. Ormo, S. Remington, Proc. Natl. Acad. Sci. **94**, 2306 (1997)
66. G.J. Palm, A. Zdanov, G.A. Gaitanaris, R. Stauber, G.N. Pavlakis, A. Wlodawer, Nat. Struct. Biol. **4**, 361 (1997)
67. H. Lossau, A. Kummer, R. Heinecke, F. Pollinger-Dammer, C. Kompa, G. Bieser, T. Jonsson, C.M. Silva, M.M. Yang, D.C. Youvan, M.E. Michel-Beyerle, Chem. Phys. **213**, 1 (1996)
68. K. Winkler, J.R. Lindner, V. Subramaniam, T.M. Jovin, P. Vöhringer, Phys. Chem. Chem. Phys. **4**, 1072 (2002)
69. J.T.M. Kennis, D.S. Larsen, I.H.M. van Stokkum, M. Vengris, J.J. van Thor, R. van Grondelle, Proc. Natl. Acad. Sci. **101**, 17988 (2004)

70. G. Striker, V. Subramaniam, C.A.M. Seidel, A. Volkmer, J. Phys. Chem. B **103**, 8612 (1999)
71. T. Polivka, V. Sundström, Chem. Rev. **104**, 2021 (2004)
72. F.L. de Weerd, I.H.M. van Stokkum, R. van Grondelle, Chem. Phys. Lett. **354**, 38 (2002)
73. C.C. Grandinaru, J.T.M. Kennis, E. Papagiannakis, I.H.M. van Stokkum, R.J. Cogdell, G.R. Fleming, R.A. Niederman, R. van Grondelle, Proc. Natl. Acad. Sci. **98**, 2364 (2001)
74. D. Zigmantas, T. Polivka, R.G. Hiller, A. Yartsev, V. Sundström, J. Phys. Chem. A **105**, 10296 (2001)
75. J.P. Zhang, T. Inaba, Y. Watanabe, Y. Koyama, Chem. Phys. Lett. **332**, 351 (2000)
76. E. Papagiannakis, J.T.M. Kennis, I.H.M. van Stokkum, R.J. Cogdell, R. van Grondelle, Proc. Natl. Acad. Sci. **99**, 6017 (2002)
77. P. Tavan, K. Schulten, J. Chem. Phys. **85**, 6602 (1986)
78. E. Papagiannakis, S.K. Das, A. Gall, I.H.M. van Stokkum, B. Robert, R. van Grondelle, H.A. Frank, J.T.M. Kennis, J. Phys. Chem. B **107**, 5642 (2003)
79. J.A. Bautista, R.E. Connors, B.B. Raju, R.G. Hiller, F.P. Sharples, D. Gosztola, M.R. Wasielewski, H.A. Frank, J. Phys. Chem. B **103**, 8751 (1999)
80. D. Zigmantas, R.G. Hiller, A. Yartsev, V. Sundström, T. Polivka, J. Phys. Chem. B **107**, 5339 (2003)
81. S. Shima, R.P. Ilagan, N. Gillespie, B.J. Sommer, R.G. Hiller, F.P. Sharpless, H.A. Frank, R.R. Birge, J. Phys. Chem. A **107**, 8052 (2003)
82. E. Papagiannakis, D.S. Larsen, I.H.M. van Stokkum, M. Vengris, R.G. Hiller, R. van Grondelle, Biochem. **43**, 15303 (2004)
83. T.E. Meyer, Biochim. Biophys. Acta **806**, 175 (1985)
84. T.E. Meyer, E. Yakali, M.A. Cusanovich, G. Tollin, Biochem. **26**, 418 (1987)
85. W.W. Sprenger, W.D. Hoff, J.P. Armitage, K.J. Hellingwerf, J. Bacteriol. **175**, 3096 (1993)
86. M. Baca, G.E. Borgstahl, M. Boissinot, P.M. Burke, D.R. Williams, K.A. Slater, E.D. Getzoff, Biochem. **33**, 14369 (1994)
87. W.D. Hoff, P. Dux, K.H.B. Devreese, I.M. Nugteren-Roodzant, W. Crielaard, R. Boelens, R. Kaptein, J. van Beeumen, K.J. Hellingwerf, Biochem. **33**, 13959 (1994)
88. Y. Imamoto, T. Ito, M. Kataoka, F. Tokunaga, FEBS Lett. **374**, 157 (1995)
89. U.K. Genick, G.E. Borgstahl, K. Ng, Z. Ren, C. Pradervand, P.M. Burke, V. Srajer, T.Y. Teng, W. Schildkamp, D.E. McRee, K. Moffat, E.D. Getzoff, Science **275**, 1471 (1997)
90. U.K. Genick, S.M. Soltis, P. Kuhn, I.L. Canestrelli, E.D. Getzoff, Nature **392**, 206 (1998)
91. B. Perman, V. Srajer, Z. Ren, T. Teng, C. Pradervand, T. Ursby, D. Bourgeois, F. Schotte, M. Wulff, R. Kort, K. Hellingwerf, K. Moffat, Science **279**, 1946 (1998)
92. A. Xie, L. Kelemen, J. Hendriks, B.J. White, K.J. Hellingwerf, W.D. Hoff, Biochem. **40**, 1510 (2001)
93. R. Brudler, R. Rammelsberg, T.T. Woo, E.D. Getzoff, K. Gerwert, Nat. Struct. Biol. **8**, 265 (2001)
94. A. Baltuška, I.H.M. van Stokkum, A. Kroon, R. Monshouwer, K.J. Hellingwerf, R. van Grondelle, Chem. Phys. Lett. **270**, 263 (1997)

95. T. Gensch, C.C. Gradinaru, I.H.M. van Stokkum, J. Hendriks, K. Hellingwerf, R. van Grondelle, Chem. Phys. Lett. **356**, 347 (2002)
96. A. Xie, W.D. Hoff, A.R. Kroon, K.J. Hellingwerf, Biochem. **35**, 14671 (1996)
97. Y. Zhou, L. Ujj, T.E. Meyer, M.A. Cusanovich, G.H. Atkinson, J. Phys. Chem. A **105**, 5719 (2001)
98. H. Chosrowjan, N. Mataga, Y. Shibata, Y. Imamoto, F. Tokunaga, J. Phys. Chem. B **102**, 7695 (1998)
99. M.A. Cusanovich, T.E. Meyer, Biochem. **42**, 4759 (2003)
100. K.J. Hellingwerf, J. Hendriks, T. Gensch, J. Phys. Chem. A **107**, 1082 (2003)
101. D.S. Larsen, R. van Grondelle, ChemPhysChem **6**, 828 (2005)
102. L. Ujj, S. Devanathan, T.E. Meyer, M.A. Cusanovich, G. Tollin, G.H. Atkinson, Biophys. J. **75**, 406 (1998)
103. S. Devanathan, A. Pacheco, L. Ujj, M. Cusanovich, G. Tollin, S. Lin, N. Woodbury, Biophys. J. **77**, 1017 (1999)
104. Y. Imamoto, M. Kataoka, F. Tokunaga, T. Asahi, H. Masuhara, Biochem. **40**, 6047 (2001)
105. H. Chosrowjan, N. Mataga, N. Nakashima, I. Yasushi, F. Tokunaga, Chem. Phys. Lett. **270**, 267 (1997)
106. P. Changenet, H. Zhang, M.J. van der Meer, K.J. Hellingwerf, M. Glasbeek, Chem. Phys. Lett. **282**, 276 (1998)
107. M. Vengris, M.A. van der Horst, G. Zgrablic, I.H.M. van Stokkum, S. Haacke, M. Chergui, K.J. Hellingwerf, R. van Grondelle, D.S. Larsen, Biophys. J. **87**, 1848 (2004)
108. S. Devanathan, S. Lin, M.A. Cusanovich, N. Woodbury, G. Tollin, Biophys. J. **79**, 2132 (2000)
109. S. Mukamel, *Principles of nonlinear optical spectroscopy* (Oxford University Press, 1995)
110. V. May, O. Kühn, *Charge and energy transfer dynamics in molecular systems* (Wiley-VCH, Berlin, 2004)
111. H. van Amerongen, L. Valkunas, R. van Grondelle, *Photosynthetic excitons* (World Scientific, Singapore, 2000)
112. T. Renger, V. May, O. Kühn, Phys. Rep. **343**, 137 (2001)
113. J. L. Herek (ed.), *Coherent Control of Photochemical and Photobiological Processes*, special issue, J. Photochem. Photobiol. A Chemistry, **180**, 225 (2006).
114. T. Halfmann, Opt. Comm. **264**, 247 (2006)
115. J.L. Herek, W. Wohlleben, R.J. Cogdell, D. Zeidler, M. Motzkus, Nature **417**, 533 (2002)
116. B. Brüggemann, V. May, J. Phys. Chem. B **108**, 10529 (2004)
117. B. Brüggemann, K. Sznee, V. Novoderezhkin, R. van Grondelle, V. May, J. Phys. Chem. B **108**, 13563 (2004)
118. B. Brüggemann, V. May, Chem. Phys. Lett. **400**, 573 (2004)
119. B. Brüggemann, T. Pullerits, V. May, in [113], p. 322.
120. D. Voronine, D. Abramavicius, S. Mukamel, J. Chem. Phys. **124**, 034104 (2006)
121. T. Brixner, G. Krampert, T. Pfeifer, R. Selle, G. Gerber, M. Wollenhaupt, O. Graefe, C. Horn, D. Liese, T. Baumert, Phys. Rev. Lett. **92**, 208301 (2004)
122. A. Kaiser, V. May, J. Chem. Phys. **121**, 2528 (2004)
123. A. Kaiser, V. May, Chem. Phys. Lett. **405**, 339 (2005)
124. A. Kaiser, V. May, Chem. Phys. **320**, 95 (2006)

125. D.E. Tronrad, B.W. Matthews, in *Photosynthetic reaction centers*, ed. by J. Deisenhofer, J.R. Norris (Academic Press, 1993)
126. M. Wendling, M.A. Przyjalgowski, D. Gülen, S.I.E. Vulto, T.J. Aartsma, R. van Grondelle, H. van Amerongen, Phot. Res. **71**, 99 (2002)
127. B. Brüggemann, V. May, J. Chem. Phys. **118**, 746 (2003)
128. B. Brüggemann, V. May, J. Chem. Phys. **120**, 2325 (2004)
129. B. Brüggemann, D.V. Tsivlin, V. May, *Quantum dynamics in complex molecular systems* (Springer Series in Chemical Physics 83, 2006)
130. V. May, Int. J. Quant. Chem. **106**, 3056 (2006)
131. S.A. Rice, M. Zhao, *Optical control of molecular dynamics* (Wiley, New York, 2000)
132. M. Shapiro, P. Brumer, *Principles of the quantum control of molecular processes* (Wiley, New York, 2003)
133. Y. Ohtsuki, W. Zhu, H. Rabitz, J. Chem. Phys. **110**, 9825 (1999)
134. T. Mančal, V. May, Euro. Phys. J. D **14**, 173 (2001)
135. T. Mančal, U. Kleinekathöfer, V. May, J. Chem. Phys. **117**, 636 (2002)
136. R. Xu, Y.J. Yan, Y. Ohtsuki, Y. Fujimura, H. Rabitz, J. Chem. Phys. **120**, 6600 (2004)
137. S. Pagola, P.W. Stephens, D.S. Bohle, A.D. Kosar, S.K. Madsen, Nature **404**, 307 (2000)
138. P.M. ONeill, P.A. Stocks, M.D. Pugh, N.C. Araujo, K.E.E. Orshin, J.F. Bickley, S.A. Ward, P.G. Bray, E. Paini, J. Davies, V.E. Erissimo, M.D. Bachi, Angew. Chem. Int. Ed. **43**, 4193 (2004)
139. W. Freyer, H. Stiel, M. Hild, K. Teuchner, D. Leupold, Photochem. Photobiol. **66**, 596 (1997)
140. A.C. Uhlemann, A. Cameron, U. Eckstein-Ludwig, J. Fischbarg, P. Iserovich, F.A. Zuniga, M. East, A. Lee, L. Brady, R.K. Haynes, S. Krishna, Nat. Struc. Biol. **12**, 628 (2005)
141. S. Kapetanaki, C. Varotsis, J. Med. Chem. **44**, 3150 (2001)
142. R. Bonnet, Chem. Soc. Rev. **24**, 19 (1995)
143. M.R. Hamblin, E.L. Newman, J. Photochem. Photobiol., B **23**, 3 (1994)
144. I.J. Macdonald, T.J. Dougherty, J. Porphyrins Phthalocyanines **5**, 105 (2001)
145. J.M.D. Cruz, I. Pastirk, M. Comstock, V.V. Lozovoy, M. Dantus, Proc. Natl. Acad. Sci. **101**, 16996 (2004)
146. D. Kearns, A. Khan, Photochem. Photobiol. **10**, 193 (1969)
147. R. Schmidt, K. Schaffner, W. Trost, H.D. Brauer, J. Phys. Chem. **88**, 956 (1984)
148. K.B. Eisenthal, N.J. Turro, C.G. Dupuy, D.A. Hrovat, J. Langan, T.A. Jenny, E.V. Sitzmann, J. Phys. Chem. **90**, 5168 (1986)
149. J. Rigaudy, C. Breliere, P. Scribe, Tetrahedron Lett. **7**, 687 (1978)
150. A. Klein, M. Kalb, M.S. Gudipati, J. Phys. Chem. A **103**, 3843 (1999)
151. B.O. Roos, *Advances in Chemical Physics: The complete active space self-consistent field method and its application in electronic structure calculations*, vol. 69 (John Wiley & Sons Ltd., 1987)
152. K. Pierloot, B. Dumez, P.O. Widmark, B.O. Roos, Theor. Chim. Acta **90**, 87 (1995)
153. G. Karlström, R. Lindh, P.A. Malmqvist, B.O. Roos, U. Ryde, V. Veryazov, P.O. Widmark, M. Cossi, B. Schimmelpfennig, P. Neogrady, L. Seijo, Comput. Mat. Sci. **28**, 222 (2003)

154. K. Anderson, P.A. Malmqvist, B.O. Roos, A.J. Sadlej, K. Wolinski, J. Chem. Phys. **96**, 1218 (1990)
155. P.O. Widmark, P.A. Malmqvist, B.O. Roos, Theor. Chim. Acta **77**, 291 (1990)
156. M.J. Frisch, G.W. Trucks, H.B. Schlegel, G.E. Scuseria, M.A. Robb, J.R. Cheeseman, V.G. Zakrzewski, J.A. Montgomery, R.E. Stratmann, J.C. Burant, S. Dapprich, J.M. Millam, A.D. Daniels, K.N. Kudin, M.C. Strain, O. Farkas, J. Tomasi, V. Barone, M. Cossi, R. Cammi, B. Mennucci, C. Pomelli, C. Adamo, S. Clifford, J. Ochterski, G.A. Petersson, P.Y. Ayala, Q. Cui, K. Morokuma, D.K. Malick, A.D. Rabuck, K. Raghavachari, J.B. Foresman, J. Cioslowski, J.V. Ortiz, B.B. Stefanov, G. Liu, A. Liashenko, P. Piskorz, I. Komaromi, R. Gomperts, R.L. Martin, D.J. Fox, T. Keith, M.A. Al-Laham, C.Y. Peng, A. Nanayakkara, C. Gonzalez, M. Challacombe, P.M.W. Gill, B.G. Johnson, W. Chen, M.W. Wong, J.L. Andres, M. Head-Gordon, E.S. Replogle, J.A. Pople, *Gaussian 98 (Revision A.2)* (Gaussian, Inc., Pittsburgh PA, 1998)
157. P. Deuflhard, C. Schütte, in *Applied Mathematics entering the 21st century. Proc. ICIAM 2003*, ed. by J.M. Hill, R. Moore (2004), pp. 91–119
158. C. Schütte, A. Fischer, W. Huisinga, P. Deuflhard, J. Comput. Phys., Special Issue on Computational Biophysics **151**, 146 (1999)
159. P. Deuflhard, W. Huisinga, A. Fischer, C. Schütte, Lin. Alg. Appl. **315**, 39 (2000)
160. M. Dellnitz, O. Junge, SIAM J. Num. Anal. **36**, 491 (1999)
161. A. Fischer, S. Waldhausen, I. Horenko, E. Meerbach, C. Schütte, J. Chem. Phys., submitted (2004)
162. I. Horenko, E. Dittmer, C. Schütte, Comp. Vis. Sci. **9**, 89 (2005)
163. I. Horenko, E. Dittmer, A. Fischer, C. Schütte, Multiscale modeling and simulation, accepted (2005)
164. E. Meerbach, E. Dittmer, I. Horenko, C. Schütte, in *Computer simulations in condensed matter systems*, *Lecture Notes in Physics*, vol. 703 (2006), *Lecture notes in Physics*, vol. 703, pp. 475–497
165. P. Metzner, C. Schütte, E. Vanden-Eijnden, J. Chem. Phys. **125**, 084110 (2006)
166. F. Cordes, M. Weber, J. Schmidt-Ehrenberg, Metastable conformations via successive Perron cluster analysis of dihedrals (2002). ZIB-Report 02-40, Zuse-Institute-Zentrum, Berlin
167. P. Deuflhard, M. Weber, Lin. Alg. Appl. **398**, 164 (2005)
168. W. Huisinga, B. Schmidt, in *New algorithms for macromolecular simulation*, *Lecture notes in Computational Science and Engineering*, vol. 49, ed. by C. Chipot, R. Elber, A. Laaksonen, B. Leimkuhler, A. Mark, T. Schlick, C. Schütte, R. Skeel (Springer, 2005), *Lecture notes in Computational Science and Engineering*, vol. 49, pp. 167–182
169. C. Schütte, W. Huisinga, in *Handbook of Numerical Analysis*, vol. X, ed. by P.G. Ciaret, J.L. Lions (North-Holland, 2003), pp. 699–744
170. P. Bremaud, *Gibbs fields, Monte Carlo simulation, and queues*, *Texts in applied mathematics*, vol. 31 (Springer, New York, 1999)
171. M. Weber, Improved Perron cluster analysis (2004). ZIB-Report 03-04, Zuse-Institute-Zentrum, Berlin
172. A.P. Dempster, N.M. Laird, D.B. Rubin, J. Roy. Stat. Soc. B **39**, 1 (1977.)
173. I. Horenko, E. Dittmer, F. Lankas, J. Maddocks, P. Metzner, C. Schütte, J. Appl. Dyn. Syst., submitted (2005)
174. A.J. Viterbi, IEEE Trans. Informat. Theory **IT-13**, 260 (1967)

175. G.N. Ramachandran, V. Sasiskharan, Advan. Prot. Chem. **23**, 283 (1968)
176. D. van der Spoel, E. Lindahl, B. Hess, G. Groenhof, A. Mark, H.J. Berendsen, J. Chem. Phys. **26**, 1701 (2005)
177. C. Oostenbrink, A. Villa, A.E. Mark, W.F.V. Gunsteren, J. Comp. Chem. **25**, 1656 (2004)
178. J. Antony, B. Schmidt, C. Schütte, J. Chem. Phys. **122**, 014309 (2005)
179. T. Head-Gordon, M. Head-Gordon, M.J. Frisch, C.L. Brooks III, J.A. Pople, J. Am. Chem. Soc. **113**, 5989 (1991)
180. A. Perczel, Ö. Farkas, I. Jakli, I.A. Topol, I.G. Csizmadia, J. Comp. Chem. **24**, 1026 (2003)
181. L. Schäfer, C.V. Alsenoy, J.N. Scarsdale, J. Chem. Phys. **76**, 1439 (1982)
182. H. Hu, M. Elstner, J. Hermans, Proteins **50**, 451 (2003)
183. Y. Mu, G. Stock, J. Phys. Chem. B **106**, 5294 (2002)
184. Y. Mu, P.H. Nguyen, G. Stock, Proteins **58**, 45 (2004)
185. W.G. Han, K.J. Jalkanen, M. Elstner, S. Suhai, J. Phys. Chem. B **102**, 2587 (1998)
186. F.C. Tenover, J.K.R. eds P R Murray, E.J. Baron, M.A. Pfaller, *Manual of clinical Microbiology* (Amer. Society for Microbiology, 1999)
187. J. Ho, Analy. Chim. Acta **457**, 125 (2002)
188. P. Belgrader, W. Benett, D. Hadley, J. Richards, P. Stratton, R. Mariella, F. Milanovich, Science **284**, 449 (1999)
189. S.I. Makino, H.I. Cheun, M. Wateral, I. Uchida, K. Takeshi, Appl. Microbio. **33**, 237 (2001)
190. B. Beatty, S. Mai, J. Squire (eds.), *FISH: a practical approach* (Oxford University Press, 2002)
191. F. Pourahmadi, M. Taylor, G. Kovacs, K. Lloyd, S. Sakai, T.S.B. Helton, L. Western, S. Zaner, J. Ching, B. McMillan, P. Belgrader, M.A. Northrup, Clin. Chem. **46**, 1151 (2000)
192. B.K. De, S.L. Bragg, G.N. Sanden, K.E. Wilson, L.A. Diem, C.K. Marston, A.R. Hoffmaster, G.A. Barnett, R.S. Weyant, T.G. Abshire, J.W. Ezzell, T. Popovic, Emerging Infection Diseases **8**, 1060 (2002)
193. C. Hagleitner, A. Hierlemann, D. Lange, A. Kummer, N. Kerness, O. Brand, H. Baltes, Nature **414**, 293 (2001)
194. P. Francois, M. Bento, P. Vaudaux, J. Schrenzel, J. Micros. Meth. **55**, 755 (2003)
195. T.H. Rider, M.S. Petrovick, F.E. Nargi, J.D. Harper, E.D. Schwoebel, R.H. Mathews, D.J. Blanchard, L.T. Bortolin, A.M. Young, J.Z. Chen, M.A. Hollis, Science **301**, 213 (2003)
196. Y.L. Pan, J. Hartings, R.G. Pinnick, J.H. S C Hill, R.K. Chang, Aerosol Sci. Tech **37**, 627 (2003)
197. F.L. Reyes, T.H. Jeys, N.R. Newbury, C.A. Primmerman, G.S. Rowe, A. Sanchez, Field Anal Chem. Tech. **3**, 240 (1999)
198. J.D. Eversole, W.K. Cary, C.S. Scotto, R. Pierson, M. Spence, A.J. Campillo, Field Anal. Chem. Tech. **5**, 205 (2001)
199. G.A. Luoma, P.P. Cherrier, L.A. Retfalvi, Field Anal. Chem. Tech. **3**, 260 (1999)
200. Y.L. Pan, K.B. Aptowicz, R.K. Chang, M. Hart, J.D. Eversole, Opt. Lett. **28**, 589 (2003)
201. P. Kaye, E. Hirst, T.J. Wang, Appl.Opt **36**, 6149 (1997)

202. S.C. Hill, R.P. Pinnick, S. Niles, Y.L. Pan, S. Holler, R.K. Chang, J. Bottiger, B.T. Chen, C.S. Orr, G. Feather, Field Anal Chem. Tech. **5**, 221 (1999)
203. Y.L. Pan, P. Cobler, S. Rhodes, A. Potter, T. Chou, S. Holler, R.K. Chang, R.G. Pinnick, J.P. Wolf, Rev.Sci.Inst. **72**, 1831 (2001)
204. R.G. Pinnick, S.C. Hill, Y.L. Pan, R.K. Chang, Atmosph.Environ. **38**, 1657 (2004)
205. Y.S. Cheng, E.B. Barr, B.J. Fan, P.J. Hargis, D.J. Rader, T.J. OHern, T.R. Torczynski, G.C. Tisone, B.L. Preppernau, S.A. Young, R.J. Radloff, Aero.Sci.Tech. **31**, 409 (1999)
206. C. Weitkamp (ed.), *Lidar*, vol. 102 (Springer-Verlag, New York, 2005)
207. F. Immler, D. Engelbart, O. Schrems, Atmos.Chem.Phys **4**, 5831 (2004)
208. T. Brixner, N.H. D, P. Niklaus, G. Gerber, Nature **414**, 57 (2001)
209. T. Brixner, N.H. D, B. Kiefer, G. Gerber, J.Chem. Phys. **118** (2003)
210. B. Li, H. Rabitz, J.P. Wolf, J. Chem. Phys. **122**, 154103 (2005)
211. S.C. Hill, V. Boutou, J. Yu, S. Ramstein, J.P. Wolf, Y. Pan, S. Holler, R.K. Chang, Phys.Rev.Lett. **85**, 54 (2000)
212. V. Boutou, C. Favre, S.C. Hill, Y. Pan, R.K. Chang, J.P. Wolf, App.Phys.B **75**, 145 (2002)
213. Y. Pan, S.C. Hill, J.P. Wolf, S. Holler, R.K. Chang, J.R. Bottiger, Appl. Opt. **41**, 2994 (2002)
214. C. Favre, V. Boutou, S.C. Hill, W. Zimmer, M. Krenz, H. Lambrecht, J. Yu, R.K. Chang, L. Woeste, J.P. Wolf, Phys.Rev.Lett. **89**, 035002 (2002)
215. J. Kasparian, M. Rodriguez, G. Méjean, J. Yu, E. Salmon, H. Wille, R. Bourayou, S. Frey, Y.B. Andre, A. Mysyrowicz, R. Sauerbrey, J.P. Wolf, L. Woeste, Science **301**, 61 (2003)
216. G. Méjean, J. Kasparian, J. Yu, S. Frey, E. Salmon, J.P. Wolf, Appl. Phys. **78**, 535 (2004)
217. F. Courvoisier, V. Boutou, V. Wood, J.P. Wolf, A. Bartelt, M. Roth, H. Rabitz, App. Phys. Lett. **87**, 063901 (2005)
218. A.L. Sobolewski, W. Domcke, C. Dedonder-Lardeux, C. Jouvet, Phys. Chem. Chem. Phys. **4**, 1093 (2002)
219. J. Teraoka, P.A. Harmon, S.A. Asher, J. Am. Chem. Soc. **112**, 2892 (1989)
220. H.B. Steen, J. Chem. Phys. **61**, 3997 (1974)
221. S. Morel, N. Leon, P. Adam, J. Amouroux, Appl. Opt. **42**, 6184 (2005)
222. P.B. Dixon, D.W. Hahn, Anal. Chem. **77**, 631 (2005)
223. M. Baudelet, L. Guyon, J. Yu, J.P. Wolf, T. Amodeo, E. Fréjafon, P. Laloi, to be published in J. App. Physics (2006)
224. M. Baudelet, M. Bossu, J. Jovelet, J. Yu, J.P. Wolf, T. Amodeo, E. Fréjafon, P. Laloi, submitted (2006)
225. M. Baudelet, L. Guyon, J. Yu, J.P. Wolf, T. Amodeo, E. Fréjafon, P. Laloi, App. Phys. Lett. **88**, 053901 (2006)
226. K. Stelmanszczyk, P. Rohwetter, G. Méjean, J. Yu, E. Salmon, J. Kasparian, R. Ackermann, J.P. Wolf, L. Woeste, App. Phys. Lett. **85**, 3977 (2004)